

Shapes from Pixels

THÈSE N° 6986 (2016)

PRÉSENTÉE LE 18 MARS 2016

À LA FACULTÉ INFORMATIQUE ET COMMUNICATIONS
LABORATOIRE DE COMMUNICATIONS AUDIOVISUELLES
PROGRAMME DOCTORAL EN GÉNIE ÉLECTRIQUE

ÉCOLE POLYTECHNIQUE FÉDÉRALE DE LAUSANNE

POUR L'OBTENTION DU GRADE DE DOCTEUR ÈS SCIENCES

PAR

Mitra FATEMI

acceptée sur proposition du jury:

Prof. S. Süssstrunk, présidente du jury
Prof. M. Vetterli, directeur de thèse
Dr G. Peyré, rapporteur
Dr A. Hansen, rapporteur
Prof. M. Unser, rapporteur



ÉCOLE POLYTECHNIQUE
FÉDÉRALE DE LAUSANNE

Suisse
2016

Acknowledgments

I sincerely thank my thesis advisor, Prof. Martin Vetterli, who gave me the chance to do a PhD at his lab and bared with me through my pregnancy time and the months after, when I was struggling to find a balance between my work and my new role as a mom. He is a man with endless enthusiasm for research and a great inspiration to his students. Thank you Martin for giving me just enough amount of guidance and freedom to develop my own research, in spite of all the difficulties I went through.

I would like to extend my appreciation to my committee members, Prof. Sabine Süsstrunk, Dr. Gabriel Peyré, Dr. Anders Hansen and Prof. Michael Unser, who took the time to read my thesis and valued my research.

I am very thankful to the members of LCAV for being part of this journey. First, I would like to thank my wonderful office mate, Marta Martinez Camara, with whom I shared an office and lots of feelings for nearly 4 years. She was a source of courage and confidence to me and other few female members of the lab. I would like to thank Loïc Baboulaz for his support during my PhD career and in particular, for facilitating my return from the maternity leave. Also, I am thankful to Amina, Reza, Ivan, Niranjana, Xue, Hanjie and Robin for their support in different aspects of this journey.

Doing a PhD with a young child was not easy at all and it became possible only through the help of my wonderful and generous Iranian friends. A special feeling of gratitude to Haleh and Mohsen, Negar and Amir Hessam, Nastaran and Omid, whom I do not hesitate to call my family. Thanks to Nasibeh and Sina, and Maryam and Masih for their endless help and to all of my friends who made my stay in Lausanne smooth and pleasant.

No word can justly express my appreciation to my family. I am very thankful to my parents, Ardeshir and Batool, for the unconditional support and love I received in my life. They raised me up with their sacrifice and helped me to achieve my dreams. I still remember how my mom stayed up every night so that I do not feel alone when I was studying for the university entrance exam and how my dad prepared my daily list of books and supplements with no pause, when I was at high school. And my lovely brother, Mohammad-Ali, who stood by me and encouraged me all my life and put my goals and dreams prior to his.

I am also honored to have an amazing family-in-law, who supported *us* in different ways specially during the last couple of years. I am very grateful to my grandparents-in-law, Zinat and Asadollah, for their true support and encouragement and my sister-in-law and her husband, Atoosa and Behzad, for making this journey more fun.

And my special thanks goes to my mother-in-law, Mehran, and my mom from whom I received unimaginable support that far exceeds expectations. Each of these two angels spent near a full year with me and my child here in Lausanne to fill in the absence of my husband. They spoiled me and my child with their infinite support, love and care. Without them, I could not stand the workload and difficulties of doing a PhD and raising a child while being away from my husband.

My sweetheart, Delaram, was a big part of this journey. My husband, Arash, and I got to know that we are going to have a child in the middle of my PhD, when he was about to return to Iran to start his new job. Since then, we had to constantly look for solutions to take the best care of our child. At some point, I had to decide about putting Delaram in a daycare and this, by far, was the hardest decision of my life. I will never forget the pain of leaving her at the daycare the first days when she was crying to come back to my arms. But, this little angel adapted herself very well to the new routine and gave me strength and ambition to never surrender. Delaram, you attended me every morning by saying “go to work” and welcomed me every evening with your sweet smile. Is there any greater motivation in life?

And my foremost recognition goes to my husband, Arash Amini, who spurred me on with his patience, enthusiasm and diligence and lit my path with his kind guidance. Above all, he made a big sacrifice by accepting to be far from our child for long and repeated periods while craving for her so that I continue and finish my PhD. Arash, I got to know you as a hero and you are still my hero in many aspects of life. This thesis exists only because you encouraged me to pursue my PhD and you stood by me past all obstacles.

I dedicate this thesis with all my love to Arash and Delaram.

Lausanne, March 2016

Abstract

In today's digital world, sampling is at the heart of any signal acquisition device: the device senses and stores analog signals at certain points in time or space and uses the samples later for the representation of the signal, possibly after some post processing. Imaging devices are ubiquitous examples that capture two-dimensional visual signals and store them as the pixels of discrete images. The main concern is whether and how the pixels provide an exact or at least a fair representation of the original visual signal in the continuous domain. This motivates the design of exact reconstruction or approximation techniques for a target class of images. Such techniques benefit different imaging tasks such as super-resolution, deblurring and compression.

This thesis focuses on the reconstruction of visual signals representing a shape over a background, from their samples. Shape images have only two different intensity values (0 and 1). However, the filtering effect caused by the sampling kernel of imaging devices smooths out the sharp transitions in the image and results in samples with varied intensity levels. To trace back the shape boundaries, we need strategies to reconstruct the original bilevel image. But, abrupt intensity changes along the shape boundaries as well as diverse shape geometries make reconstruction of this class of signals very challenging.

Curvelets and their discrete domain counterparts – contourlets – have been proved as efficient multiresolution representations for the class of shape images. This motivates the approximation of shape images in the aforementioned domains. In the first part of this thesis, we study generalized sampling and infinite-dimensional compressed sensing techniques to approximate a signal in a domain that is known to provide a sparse or efficient representation for the signal, given its samples in a different domain. We show that the generalized sampling scheme, due to its linearity, is incapable of generating good approximation of shape images, especially from a limited number of samples. The infinite-dimensional compressed sensing is a more promising approach for recovering efficient signal representations in a domain. However, the concept of random sampling in this scheme does not apply to the shape reconstruction problem.

Next, we propose a scheme for sampling and reconstruction of shape images with finite rate of innovation (FRI). More specifically, we model the shape boundaries as a subset of an algebraic curve with an implicit bivariate polynomial. We show that the image parameters – i.e., the polynomial coefficients – are the solutions of a set of linear annihilation equations with the coefficients being the image moments. We then replace conventional 2D moments with more stable *generalized moments* that are adjusted to the given sampling kernel. This leads to successful reconstruction of shape images with moderate complexities from samples generated with realistic sampling kernels and in the presence of low to moderate noise levels.

The proposed FRI scheme falls short of reconstructing shape images with intricate geometries from realistic samples. Our next contribution is a scheme for recovering shape images with smooth boundaries from a set of samples. The reconstructed image is constrained to regenerate the same samples (measurement consistency) as well as forming a bilevel image. We initially for-

mulate the reconstruction technique by minimizing the shape perimeter over the set of consistent binary shapes. Next, we relax the non-convex shape constraint to transform the problem into minimizing the total variation over consistent non-negative-valued images. We also introduce a requirement – called *reducibility* – that guarantees equivalence between the two problems. We illustrate that the reducibility property effectively sets a requirement on the minimum sampling density. In this scheme, unlike FRI schemes, we do not constrain the boundary curves by any specific model. Instead, we let the sampling kernel and the sample values decide for them. As a result, there is less restriction on the achievable shape geometries.

In the last part of this thesis, we study a relevant problem in the Boolean domain: the Boolean compressed sensing, also known as group testing problem. The problem is about recovering a sparse Boolean vector from a few collective binary tests. We first study a formulation of this problem as a binary linear program, which is NP hard in general. To overcome the computational burden, we can relax the binary constraint on the variables and apply a rounding to the solution of the relaxed linear program. We introduce a randomized algorithm to replace the rounding procedure. We show that the proposed algorithm considerably improves the success rate with only a slight increase in the computational cost.

Keywords: Algebraic curves, binary images, Cheeger sets, compressed sensing, generalized moments, generalized sampling, group testing, image reconstruction, image sampling, linear programming, measurement-consistency, randomized algorithms, shapes, signals with finite rate of innovation (FRI), sparse representations, total variation.

Résumé

Dans le monde numérique actuel, l'échantillonnage est au cœur de tout appareil d'acquisition de signal : l'appareil perçoit et enregistre les signaux analogiques à certains points dans le temps ou l'espace et utilise ses échantillons plus tard pour la représentation du signal, éventuellement après traitement. Les appareils d'imagerie sont des exemples omniprésents qui acquièrent des signaux visuels bidimensionnels et qui les enregistrent en tant que pixels d'une image discrète. Le problème principal est de savoir si, et comment, les pixels fournissent une représentation exacte ou au moins acceptable du signal visuel original dans le domaine continu. Ceci motive la conception de techniques de reconstruction exacte ou approximative pour une classe particulière d'images. De telles techniques profitent à différentes tâches d'imagerie telles que la super-résolution, la correction d'images floues et la compression.

Cette thèse se focalise sur la reconstruction de signaux visuels représentant une forme sur un fond, à partir de ses échantillons. Les images de forme ont seulement deux valeurs d'intensité différentes (0 et 1). Cependant, l'effet de filtrage induit par le noyau d'échantillonnage de l'appareil d'imagerie lisse les transitions abruptes dans l'image et crée des échantillons de niveaux d'intensité variés. Pour retrouver les limites de la forme, nous avons besoin de stratégies pour reconstruire l'image originale à deux niveaux d'intensité. Mais les changements abrupts d'intensité le long de la ligne de démarcation de la forme ainsi que les diverses géométries des formes mettent au défi la reconstruction de cette classe de signaux.

Curvelets et leurs équivalents discrets – contourlets – se sont montrés être des représentations en multi-résolution efficaces pour cette classe d'image de forme. Ceci motive l'approximation des images de forme dans les domaines susmentionnés. Dans la première partie de cette thèse, nous étudions l'échantillonnage généralisé et les techniques de détection compressée en dimension infinie pour l'approximation d'un signal dans un domaine connu pour fournir une représentation clairsemée ou efficace du signal, étant donné ses échantillons dans un domaine différent. Nous montrons que l'approche de l'échantillonnage généralisé est incapable de générer une bonne approximation, à cause de sa linéarité, en particulier à partir d'un nombre limité d'échantillons. La détection compressée en dimension infinie est une approche plus prometteuse pour retrouver les représentations efficaces de signaux dans un domaine. Cependant, le concept d'échantillonnage aléatoire de cette technique ne s'applique pas au problème de reconstruction de forme.

Dans la suite, nous proposons une approche pour l'échantillonnage et la reconstruction d'images de forme avec un taux d'innovation fini (TIF). Plus spécifiquement, nous modélisons les limites de la forme comme un sous-ensemble de la courbe algébrique avec un polynôme à deux variables implicites. Nous montrons que les paramètres de l'image – *i.e.*, les coefficients du polynôme – sont les solutions d'un ensemble d'équation d'annihilation linéaire dont les coefficients sont les moments de l'image. Nous remplaçons alors les moments 2D conventionnels par les moments généralisés plus stables qui sont ajustés selon le noyau d'échantillonnage. Ceci amène avec succès à la reconstruction d'image de forme avec une complexité modérée à partir

d'échantillons obtenus de noyaux d'échantillonnage réalistes et en présence de niveaux de bruit faible à modéré.

La solution à TIF proposée échoue pour la reconstruction d'images de forme avec des géométries compliquées depuis des échantillons réels. Notre contribution suivante est une solution pour retrouver les images de formes avec des contours lisses depuis un ensemble d'échantillons. L'image reconstruite est contrainte de recréer les mêmes échantillons (cohérence de mesure) ainsi que de former une image à deux niveaux d'intensité. Initialement, nous formulons la technique de reconstruction en minimisant le périmètre de la forme sur un ensemble de formes binaires cohérentes. Nous assouplissons ensuite la contrainte de forme non-convexe pour transformer le problème en une minimisation de la variation totale sur les images cohérentes et à valeurs non-négatives. Nous introduisons aussi une exigence – appelée réductibilité – qui garantit l'équivalence entre les deux problèmes. Nous illustrons que la propriété de réductibilité met effectivement en place une exigence sur la densité d'échantillonnage minimum. Dans cette approche, et à l'inverse des approches à TIF, nous ne contraignons pas les courbes de contour à un modèle spécifique. Au lieu de cela, nous laissons le choix au noyau d'échantillonnage et aux valeurs des échantillons. Cela aboutit à une restriction moindre sur la géométrie des formes possibles.

Dans la dernière partie de cette thèse, nous étudions un problème pertinent dans le domaine booléen : la détection compressée booléenne, aussi connue sous le nom de problème de tests de groupe. Le problème consiste à retrouver un vecteur clairsemé booléen à partir de quelques essais collectifs binaires. Nous étudions d'abord une formulation de ce problème comme un programme linéaire binaire, qui est NP-dur en général. Pour surmonter ce poids de calcul, nous pouvons assouplir la contrainte binaire sur les variables et appliquer un arrondi sur la solution du programme linéaire assoupli. Nous introduisons un algorithme aléatoire qui remplace la procédure d'arrondi. Nous montrons que l'algorithme améliore considérablement le taux de succès avec seulement un léger accroissement du coût de calcul.

Mots-clés : algorithmes aléatoires, cohérence de mesure, courbes algébriques, détection compressée, échantillonnage d'image, échantillonnage généralisé, ensemble de Cheeger, formes, images binaires, moments généralisés, programmation linéaire, reconstruction d'image, représentations clairsemées, signaux à taux d'innovation fini (TIF), test de groupe, variation totale.

Contents

Acknowledgments	ii
Abstract	v
Résumé	vii
1 Introduction	1
1.1 Motivation	1
1.2 Related Work	3
1.2.1 Signal approximation and sparse image representation	3
1.2.2 Image sampling and parametric models	5
1.2.3 Curve fitting and vectorised representations	5
1.3 Thesis Outline and Contribution	6
2 Signal Approximation	9
2.1 Motivation	9
2.2 Generalized Sampling	12
2.2.1 Problem definition	12
2.2.2 Stable signal approximation and the generalized sampling theory	14
2.3 Reconstruction of Piecewise Constant Signals	17
2.3.1 Error decay rates	17
2.3.2 Reconstruction of binary signals	18
2.4 Nonlinear Signal Approximation	19
2.4.1 Infinite-dimensional compressed sensing	21
2.4.2 Optimal sampling rate	22
2.4.3 Numerical experiments	25
2.5 Conclusion	25
3 A Robust Sampling Scheme for Shapes with Algebraic Boundaries	27
3.1 Introduction	27
3.1.1 Motivation	27
3.1.2 Contribution	28
3.2 Sampling of Algebraic Shapes	28
3.2.1 Image model	28
3.2.2 Sampling	30

3.3	Reconstruction from Moments	31
3.3.1	Annihilation equations	32
3.3.2	Stability	34
3.4	Stable Recovery	34
3.4.1	Annihilation equations with generalized moments	35
3.4.2	Constraints on the sign of the polynomial	42
3.4.3	Measurement consistency	43
3.5	Experimental Results	43
3.5.1	Noiseless recovery	43
3.5.2	Recovery in the presence of noise	43
3.5.3	Sampling kernel sensitivity	44
3.5.4	Unbounded algebraic shapes	44
3.5.5	Overfitting	48
3.5.6	Algebraic shape approximation	48
3.6	Conclusion	50
3.7	Appendix Proof of Theorem 3.2	50
4	Measurement-Consistent Shape Reconstruction	53
4.1	Introduction	53
4.2	Problem Definition	54
4.3	Cheeger Sets	55
4.4	Consistent Shape Recovery	57
4.4.1	Promoting the use of total variation for shape recovery	58
4.4.2	Theoretical results	59
4.4.3	The sampling density requirement	62
4.5	Numerical Experiments	65
4.5.1	Discrete formulation	66
4.5.2	Simulation results	68
4.6	Conclusion	73
4.7	Appendix Proof of Lemma 4.1	74
5	Randomized Recovery for Boolean Compressed Sensing	77
5.1	Introduction	77
5.2	CS and Group Testing: Recovery Bounds	79
5.3	Recovery Algorithms	80
5.4	Randomized Recovery	80
5.5	Simulation Results	83
5.6	Conclusion	84
6	Conclusion and Future Work	85
	Bibliography	89
	Curriculum Vitæ	97

Chapter 1

Introduction

اسرار ازل را نه تو دانی و نه من وین حل معما نه تو دانی و نه من
هست از پس پرده گفتگوی من و تو چون پرده برافتد نه تو مانی و نه من

The secrets eternal neither you know nor I
And answers to the riddle neither you know nor I
Behind the veil there is much talk about us, why
When the veil falls, neither you remain nor I

Omar Khayyam

1.1 Motivation

Sampling is a key block of all digital imaging devices. To store and process the data, we need to convert continuous domain visual signals $I(x, y)$ into a sequence of numbers. In digital cameras, the optical lens and the sensor array are responsible for the sampling procedure (Figure 1.1). The physics of the device imply that the measured sensor values $d_{i,j}$ –pixel values of the digital image– are samples of a filtered visual signal. The impulse response of the involved filter, denoted by $\bar{\phi}(x, y) = \phi(-x, -y)$, is called the point spread function (PSF) and is determined by the optical system. On the other hand, the sensor array controls the sampling grid and sampling density $\frac{1}{T}$. A similar model applies to other imaging devices such as magnetic resonance imaging (MRI) machines and scanners, possibly with different type of sampling kernels and sampling densities. In this sense, digital images $\mathbf{D} = [d_{i,j}]_{\{1 \leq i,j \leq m\}}$ are discrete representations of signals in the continuous world:

$$d_{i,j} = \frac{1}{T^2} \bar{\phi}\left(\frac{x}{T}, \frac{y}{T}\right) * I(x, y) \Big|_{(x,y)=(jT,iT)} = \iint_{\Omega} \frac{1}{T^2} \phi\left(\frac{x}{T} - j, \frac{y}{T} - i\right) I(x, y) dx dy, \quad (1.1)$$

where Ω represents the signal (image) domain.

Discrete images facilitate the storage, processing and transmission of visual signals. Though, they do not carry all the information of their continuous domain counterparts. For instance, one can think of geometrical features such as boundaries or edges, which are the most important perceptual information in an image and serve as descriptors in applications like object recognition,

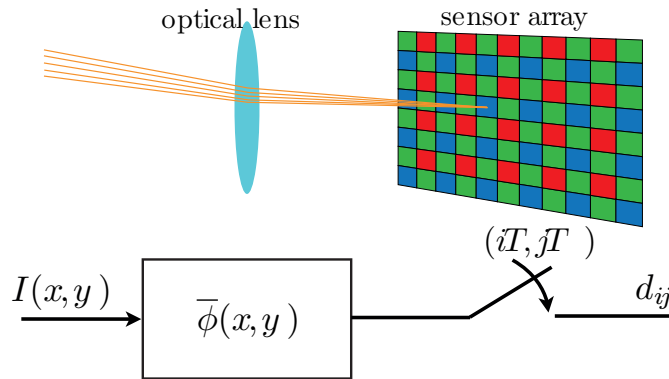


Figure 1.1: Sampling system implemented by a digital camera; the effect of the optical lens and the sensor array on 2D visual signals can be modeled by filtering followed by sampling in space.

image registration and video tracking. A given discrete image at a fixed resolution is unable to accurately describe this information. The same reason is also responsible for the unpleasant pixelated image that appears when zooming on the discrete image beyond a certain level.

On the other hand, having access to the continuous image provides us with advantages such as resolution-invariant processing and representation of the image. One immediate consequence is the unlimited zooming capability. Another consequence is that one can arbitrarily rotate a continuous domain image while in the discrete domain, only a few rotation angles are allowed without requiring a higher resolution (interpolation). The continuous domain image could also be used for feature extraction and keypoint detection (*e.g.* in the SIFT algorithm). A number of other related applications including segmentation, super-resolution and deblurring are mentioned in [77, 120].

These arguments motivate the problem of recovering continuous domain visual signals from their samples. The ideal case is when the discrete image can uniquely determine the continuous domain counterpart. But even in the absence of this condition, the recovered image $\tilde{I}(x, y)$ should be able to regenerate the same samples. This requirement assures that we cannot discriminate between the original and the recovered images, at least at the output of the sampling block. Equivalently, the reconstruction error $I - \tilde{I}$ between the original image and its approximation is in the null space of the imaging process. A reconstruction of the original image that satisfies this condition is called *measurement consistent* or *consistent* for short [109, 115, 116].

In this thesis, we study the problem of recovering measurement-consistent continuous domain visual signals from a finite number of samples. Within the broad range of visual signals, we shall focus only on the class of *shapes* over a fixed background. A shape is mathematically described as the indicator function of a union of a finite number of connected subsets \mathcal{S} over the image domain

$$\chi_{\mathcal{S}}(x, y) = \begin{cases} 1, & \text{if } (x, y) \in \mathcal{S}, \\ 0, & \text{if } (x, y) \in \Omega \setminus \mathcal{S}. \end{cases}$$

We consider shapes with arbitrary geometries and piecewise smooth boundaries. Examples of shape images can be found among artworks such as woodcut prints, planar silhouettes and



Figure 1.2: Cutout by Henri Matisse (1952) that can be classified as a shape image.

lithographs (Figure 1.2).

Shape images have only two different intensity values (0 and 1) but the filtering step of the sampling process smooths out sharp intensity transitions and results in gray scale discrete images. For a positive PSF with unit ℓ_1 norm

$$\iint \phi(x, y) \, dx \, dy = 1,$$

pixels of the discrete image shall take continuous values in the range $[0, 1]$. An example of a shape image and its associated 10×10 discrete image is shown in Figure 1.3. We recall that Figure 1.3b provides a pictorial representation of the 100 pixels in \mathbf{D} and should not be mistaken with a piecewise constant approximation of the original image.

In the consistent shape recovery problem, we look for sampling theories or approximation techniques that reconstructs a shape image from a given set of gray-scale pixels. In either case, we restrict the permissible solutions to the bilevel images which significantly adds to the difficulty of the problem. The problem of measurement-consistent shape reconstruction appears in applications where the aim is to exactly locate or describe objects in a scene; astronomical imaging, quality monitoring in manufacturing, biomedical imaging and high-quality artwork rendering are a few examples.

1.2 Related Work

The subject of this thesis can be related to several signal and image processing problems. Perhaps the most relevant topics are signal approximation, sampling and image segmentation. In the following, we briefly review related works under each of these categories, yet, we will take a sampling point of view and put the emphasis on the reconstruction of measurement-consistent shape images, in the rest of this thesis.

1.2.1 Signal approximation and sparse image representation

Consider the representation of a signal $f(x)$ in a domain spanned by a set of basis functions $\{\phi_i(x)\}_{i=0}^{\infty}$ and its dual basis $\{\tilde{\phi}_i(x)\}_{i=0}^{\infty}$

$$f(x) = \sum_{i=0}^{\infty} \langle f, \tilde{\phi}_i \rangle \phi_i(x).$$

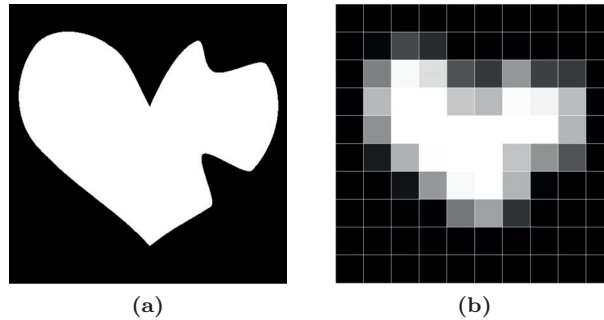


Figure 1.3: Example of a bilevel image and its acquisition: (a) a shape image, and (b) pictorial representation of 10×10 measurements, generated with a bilinear B-spline sampling kernel.

An effective representation domain captures the essence of $f(x)$ with few basis functions and provides reliable signal approximations from a few coefficients

$$f(x) \approx f_n(x) = \sum_{i=0}^n \langle f, \tilde{\phi}_i \rangle \phi_i(x).$$

The traditional Fourier expansion yields an optimal representation for regular signals [81]. For a discontinuous signal, however, the singularities have widespread effects throughout the Fourier expansion. This causes the error of the Fourier approximation of the signal to decay very slowly. In strong contrast, in the wavelet expansion, the energy associated with point singularities is mostly concentrated in just a few big coefficients. In this sense, wavelets are optimal for approximating 1D signals with bounded variation. In higher dimensions, however, other kind of singularities can be present. For example, edges in an image represent one-dimensional (1D) singularities along different directions. Neither wavelet nor Fourier provide really efficient representations for images.

An effective image representation has to deal with the intrinsic geometrical structure in images –specifically, the directional singularities– with a few coefficients. Some of the efforts towards such a representation can be found in the works of [23–26, 45, 46, 90]. In particular, the curvelet transform [26], with multiscale elongated and rotated basis functions, is shown to be optimal for functions in the continuous domain with singularities along continuously twice differentiable (C^2) curves. This transform has simple constructions in the continuous domain but the implementation for digital images is very challenging. To overcome this problem, a directional multiresolution contourlet transform was developed directly in the discrete domain [45]. This transform is the result of iteratively applying a multiscale decomposition [20, 47] and a directional filter bank [13] to the digital image and deals effectively with images having smooth contours.

The curvelet and contourlet transforms lose their (near) optimality when the image is composed of edges along irregular curves with bounded variations. These images can be optimally approximated using the adaptive bandelet transform [82, 90]. The cost for this optimality is adaptive basis functions which should be calculated individually for each image.

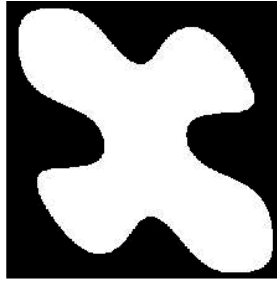


Figure 1.4: Example of an FRI shape in the range of the parametric model (1.3). The figure is taken from [88].

1.2.2 Image sampling and parametric models

The sampling problem is all about representing a continuous-time signal $f(t)$ by a discrete sequence of values $f_n, n \in \mathbb{Z}$ such that the sequence uniquely defines the original signal $f(t)$. The classical Shannon sampling theory and its variations present sampling strategies for bandlimited signals and more generally the class of signals living in a shift-invariant space [99, 114, 118]. Still, many crucial signals stay out of reach of this class. Among them are signals which can be described with a finite number of parameters, hence called signals with finite rate of innovation (FRI). In [119], a study of one-dimensional FRI signals was presented, where it was shown that the discrete samples can lead to perfect signal recovery, although the signals are not bandlimited. This work then evolved to include more general FRI signals such as piecewise polynomials [85, 119], streams of Diracs [15, 85, 119] and piecewise sinusoids [14] with sampling kernels of compact support [51, 52] and noisy samples [85, 107].

Extension of sampling schemes to images is an essential but challenging problem. Because of the sharp intensity transitions along edges, images are non-bandlimited. Also, the diverse geometry of the edges in typical images excludes them from the known shift-invariant spaces. Some preliminary efforts to generalize the FRI framework to images led to the sampling schemes with adequate sampling kernels for step-edge images and polygonal shapes [41, 84, 100]. In a recent work, an FRI-based sampling scheme is presented for images with more versatile edge geometries [88]. The curves in this model are zero level sets of a mask function that is a linear combination of a finite number of two-dimensional (2D) exponentials

$$C = \left\{ (x, y) \in [0, \tau_x] \times [0, \tau_y] : \mu(x, y) = \sum_{k=-K_0}^{+K_0} \sum_{l=-L_0}^{L_0} c_{k,l} e^{j \frac{2\pi k}{\tau_x} x + j \frac{2\pi l}{\tau_y} y} = 0 \right\}. \quad (1.3)$$

Figure 1.4 displays an example of an FRI curve in this model. The curve parameters $c_{k,l}$ are shown to satisfy an annihilation system of equations which could be solved directly, or more robustly as a minimization problem.

1.2.3 Curve fitting and vectorised representations

Continuous domain shape recovery can also be viewed as fitting boundary curves to the interpolated gray-scale image (high-resolution version of the measurements). Such methods are widely known as segmentation techniques and fit deformable curves to gray-scale images.

Different variational methods have been proposed for the image segmentation, mainly revolving around the active contour algorithm [71] and the Mumford-Shah functional [87].

Active contours, also known as snakes, are one of the most successful variational models in image segmentation and consist of evolving a contour towards the boundaries of the objects in the image. Based on the curve model, these algorithms are divided into point snakes [71], geodesic snakes [33, 71, 80] and parametric snakes [19, 63] and are mostly endowed with strong theoretical properties and good numerical results. Yet, due to the non-convexity of the energy functional, these algorithms are very sensitive to noise and initial conditions [17, 18, 43].

The Mumford-Shah functional is the other highly studied variational approach which aims at finding the best approximation of the image as a piecewise constant/smooth function through the minimization problem

$$\min_{I \in \mathbb{R}^2} \lambda \iint_{\Omega} (f - I)^2 dx dy + \iint_{\Omega \setminus C} |\nabla I|^2 dx dy + \alpha \mathcal{H}^1(C).$$

In the above equation, $f : \Omega \rightarrow \mathbb{R}$ represents the high-resolution observed image and C is the discontinuity set of I . Also, $\mathcal{H}^1(C)$ denotes the one-dimensional Hausdorff measure that weighs the regularity of C . The first integral in the functional is called the *fidelity* term and the remaining terms are the *regularization* terms. Again, this problem, in its original setting, is non-convex and different approaches have been proposed to avoid its inherent difficulty [42, 111, 117]. A convex relaxation of the piecewise constant Mumford-Shah functional was proposed in [91] leading to high quality solutions. This work was extended to the piecewise smooth functional in [92, 104].

Finally, the combination of the two mentioned variational models in a single framework has led to fast global minimization approaches for image segmentation [17, 18]. In all cases, the segmentation problem is formulated by minimizing a functional that depends on the gray-scale image and the model of the boundary curves, but does not take the PSF into account. As a consequence, the resulting piecewise constant image is likely to fail the consistency requirements.

Vectorized image representation is another way of associating a continuous shape to a discrete image. Although this representation was initially used for black and white images [98], it has been recently extended to photographic images with color [89]. The continuous domain representation could also be employed to improve the resolution of synthetic images. This application was studied in [74] for enhancing the quality of pixel arts in old video games.

1.3 Thesis Outline and Contribution

In this thesis, we study the consistent shape recovery problem along each of the three categories of the previous subsection, with a consistent emphasis on a sampling perspective. In the following, we present a summary of each chapter and its contributions.

Measurement-consistent signal approximation

The existence of (near) optimal transforms for piecewise constant images (specifically, shape images) motivates the problem of calculating the representation coefficients in one of these domains from the image samples. Obviously, we cannot calculate infinite number of coefficients from a finite number of samples. Hence, we are limited to the n -term approximations of the signal for some integer n . The ideal case is when we calculate the n largest coefficients. These are the subjects of the *generalized sampling* [1, 2] and the *infinite-dimensional compressed sensing* theories [4] that we study in Chapter 2. Generalized sampling is a linear scheme that provides

stable and quasi-optimal signal approximations in the representation domain, though with a reduced level of measurement consistency. We see that this scheme is particularly useful when the reconstruction domain, compared to the sampling domain, provides a substantially better linear approximation rate for the signals in question, whereas most of the multiresolution representations (such as wavelets and curvelets) owe their success to their fast decaying nonlinear approximation error rates.

On the contrary, the infinite-dimensional compressed sensing is a nonlinear and probabilistic approach that approximates the (semi) infinite-dimensional vector of coefficients by a sparse vector; it also retains the measurement consistency. We briefly study this theory and the *balancing property* therein, which limits the range M and the minimum number m of required samples for recovering nonlinear n -term signal approximations in some representation domain. Nonetheless, we see that the requirement of uniform (or structured) random sampling in this theory does not apply to the existing conventional imaging devices. All the studies of this section are carried out in 1D domains.

Robust sampling schemes for shapes with algebraic boundaries

The sampling result of [88] was a great success towards developing sampling theories for shape images with realistic geometries. Yet, the curve model considered in [88] (equation (1.3)) is novel and further investigation is needed to reveal its descriptive power –i.e., the range of shape geometries and the number of free parameters for generating a given shape in the range. In Chapter 3, we consider a new class of FRI bilevel images: every image in our model is the restriction of $\chi_{\{p \leq 0\}}$ to a closed domain (i.e., the image plane), where χ denotes the indicator function and p is some real bivariate polynomial. This particularly means that the boundaries in the image form a subset of an algebraic curve with the implicit polynomial p . Algebraic curves create a rich parametric model for planar curves [10, 64, 121].

We develop linear annihilation equations for the shape parameters based on the shape moments and propose robust sampling strategies for this class of shapes. To this aim, we replace the conventional 2D moments of the image by the new *generalized moments* which are less sensitive to the noise and can be adapted to a given sampling kernel. We demonstrate the performance of our algorithm in reconstructing shape images through various numerical experiments, including low to moderate noise levels and a range of realistic sampling kernels.

Measurement-consistent shape reconstruction

A parametric shape model with a bounded number of parameters allows unique recovery of the continuous domain image from a finite number of samples. Meanwhile, it admits a limited range of shape geometries. Modeling a shape image with an involved geometry (like the one in Figure 1.2) with an algebraic curve demands either a large polynomial degree or piecewise approximation of the shape contours with small-degree polynomials, both leading to computationally complex reconstructions.

In Chapter 4, we propose a variational method to recover a measurement-consistent shape image with minimum perimeter and C^2 boundary curves. Our approach in this chapter is direct in the sense that it is independent of the curve parametrization by avoiding the intermediate curve fitting step. This enables us to deal with arbitrary topologies. Besides, the choice of the PSF is arbitrary and does not need to satisfy any particular condition. In this regard, the results of this chapter can be considered as a firm sampling framework for shapes with smooth boundaries and arbitrary sampling kernels.

We formulate the method as an optimization problem constrained by the measurements (pixels), where the functional is the continuous domain total variation (TV). Ideally, we should restrict the search domain to bilevel images. This leads to a non-convex problem which is computationally intractable. Hence, we consider the convex relaxation in which the search is over the set of all non-negative-valued images. Under a minimum resolution requirements (see Definition 4.4 for an explicit explanation), we prove that all the solutions to the non-convex problem are minimizers of the convex relaxation (Theorem 4.2). This allows us to recover measurement-consistent shape images from a convex optimization problem.

Randomized recovery and boolean compressed sensing

In Chapter 5, we consider the problem of Boolean compressed sensing, which is also known as group testing. The goal is to identify a small number of defective items among a large population by grouping subset of items into a few different pools and detecting defective items based on the results of the collective tests for each pool. This problem can be formulated as a binary linear program, which is NP hard in general. To overcome the computational burden, it was recently proposed to relax the binary constraint on the variables, and apply a rounding to the solution of the relaxed linear program. In this chapter, we replace the rounding procedure by a random assignment of binary values to the variables. We use the fractional solution of the linear program as the probability of these assignments. We show that the proposed randomized algorithm considerably improves the success rate with only a slight increase in computational cost.

Finally, we conclude in Chapter 6 with a summary and a discussion of the future research avenues.

Chapter 2

Signal Approximation

2.1 Motivation

Real-world signals are inherently analog or continuous domain but we often observe them through digital measuring devices. A linear measuring process consists of sampling the signal using certain sampling kernels. The samples $\beta_i = \langle f, \phi_i \rangle$, $i = 1, 2, \dots$ of a continuous domain signal f can be regarded as its coefficients in an infinite-dimensional sampling domain $\mathcal{S} = \text{span}\{\phi_i\}_{i \in \mathbb{N}}$ with a basis made of the sampling kernels. In general, an infinite number of samples is required to precisely represent f . By adapting the sampling kernels to a specific type of signal, it is possible to reduce the infinite dimensional representation to a finite one. However, in most of the acquisition devices, the sampling kernels are limited by the physics of the device and are rarely controllable. Therefore, it is very likely that a finite collection of samples captured by a measuring device results in a poor approximation of the signal.

This is, for example, the case when we capture shape images with digital cameras. While the continuous domain boundary curves are the dominant information of shape images, the curves are hardly detectable in discrete images (Figures 2.1b and 2.1c). Adopting a continuous domain model for images implies that the discrete image per se is not a valid representation of the original image. Instead, the interpolation of pixel values (samples) with appropriate kernels generates a legitimate approximation. When the interpolating kernels form a dual basis for the sampling kernels, the approximation is equivalent to the orthogonal projection of the original image onto a finite dimensional sampling space. Yet, this approximation might be a poor reconstruction of the original shape image (Figures 2.1d and 2.1e).

One approach to reconstructing a satisfactory approximation of the signal is to represent it in another domain $\mathcal{R} = \text{span}\{\psi_j\}_{j \in \mathbb{N}}$

$$f = \sum_{j \in \mathbb{N}} \alpha_j \psi_j \quad (2.1)$$

that is proved to be efficient for the class of signals subject to the measurement. This means that any signal f in this class has fast decaying or sparse coefficients $\{\alpha_j\}_{j \in \mathbb{N}}$ in \mathcal{R} and n -term linear or non-linear approximations of f in \mathcal{R} (formed by the n first or the n largest coefficients in (2.1), respectively) rapidly converge to the signal. Subspaces spanned by wavelets are example domains

0. This chapter includes research conducted jointly with Loïc Baboulaz and Martin Vetterli [61].

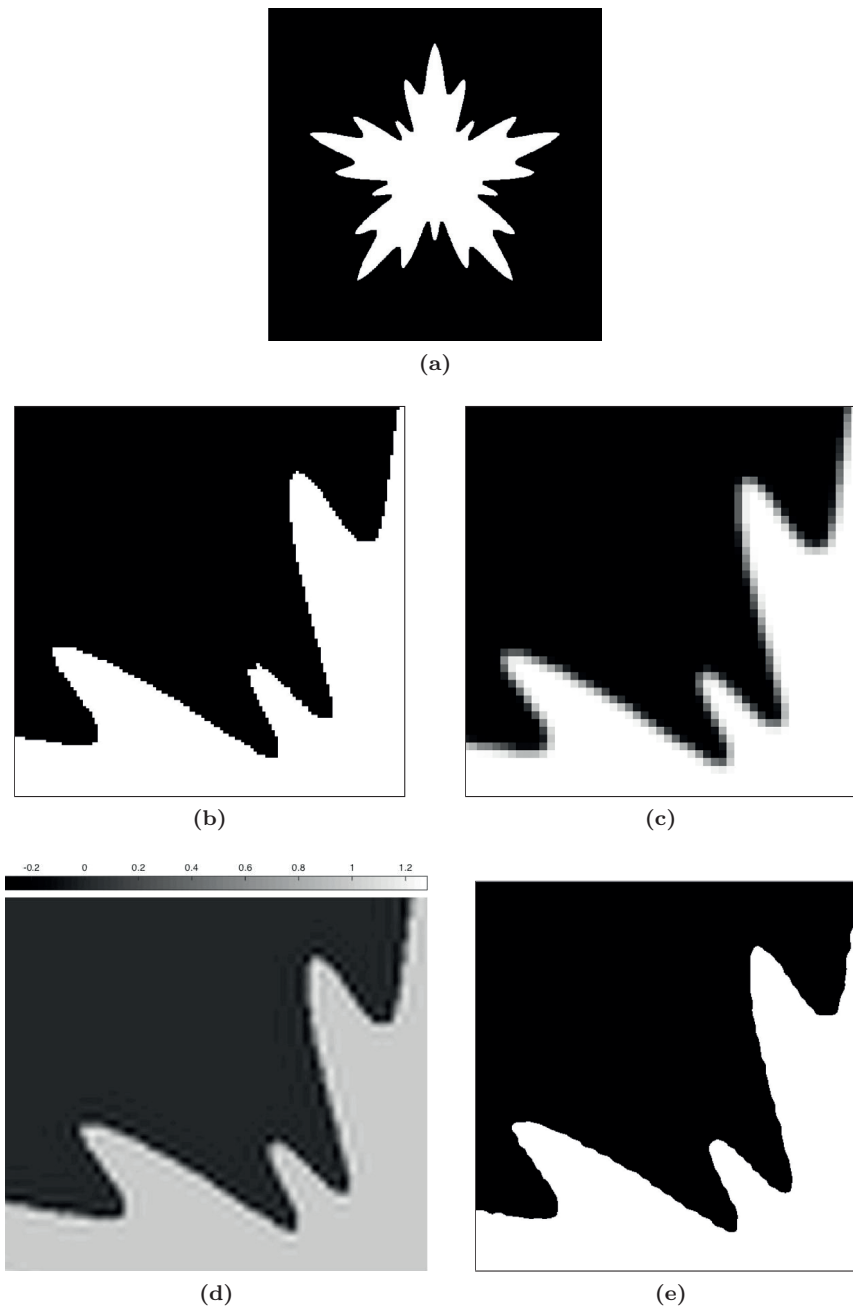


Figure 2.1: Projection of a shape image onto a finite-dimensional sampling space: Figures 2.1a and 2.1b depict a shape image (displayed at resolution 1000×1000) and an enlarged section thereof. Figure 2.1c shows the same enlarged section of a 200×200 discrete image, generated with a biquadratic B-spline PSF. Figures 2.1d and 2.1e display the same enlarged sections of the interpolated samples using the dual B-spline kernels (equivalent to the orthogonal projection to the sampling subspace) before (PSNR=26.2294 dB) and after (PSNR=26.8698 dB) thresholding at level 0.5, respectively. Also, consistency between the samples (discrete images) of the images in 2.1d and 2.1e and the original samples are 122.4234 dB and 46.3432 dB, respectively.

that provide optimal representations for piecewise continuous signals with pointwise singularities. Also, curvelet [26] and contourlet [45] domains provide fast converging approximations for shape images.

Finding the signal representation in a new domain requires having access to the signal values at every point, while in our problem, we only access a finite number, say m , of the samples in a different domain. This brings us to the following question: what is an appropriate way of calculating the signal approximation in the new domain that preserves the domain efficiency in representing the signal? In the following, we show one example of an ill-advised procedure that causes false results.

Example 2.1

Consider the representation of an image $I(x, y)$ in terms of some basis functions $\{\psi_i(x, y)\}_{i \in \mathbb{N}}$,

$$I(x, y) = \sum_{i=1}^{+\infty} \alpha_i \psi_i(x, y), \quad (2.2)$$

and the nonlinear approximation of $I(x, y)$ generated with the m largest terms in (2.2)

$$\hat{I}_m(x, y) = \sum_{i \in \mathcal{I}} \alpha_i \psi_i(x, y),$$

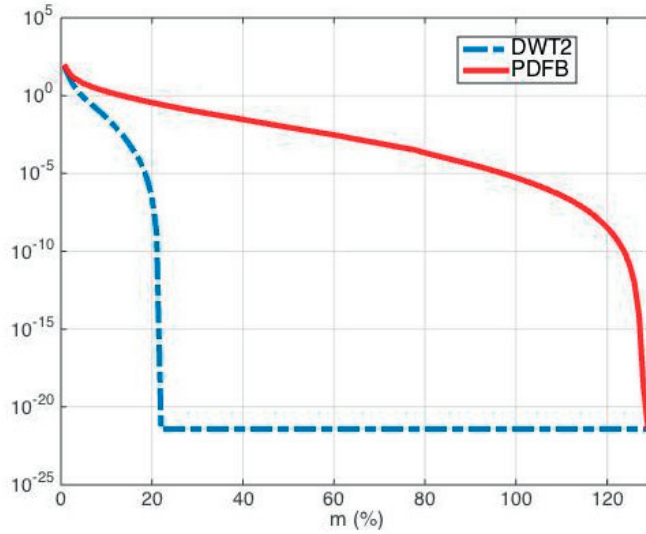
$$\mathcal{I} = \{\alpha_i : |\alpha_i| \geq |\alpha_j|, \forall j \in \mathbb{N}, j \neq i\}, \text{ with } |\mathcal{I}| = m.$$

For a piecewise regular image with discontinuities along 1D curves (e.g. a shape image), the error decay rate of the image approximation in the wavelet domain is limited to $\mathcal{O}(m^{-1})$ [81]. On the other hand, when $I(x, y)$ is a piecewise C^2 image with discontinuities along C^2 curves, the m -term contourlet approximation yields an error decay rate of $\mathcal{O}((\log m)^3 m^{-2})$ [45, 81].

Because of the existence of discrete wavelet and contourlet transforms, it might be tempting to approximate a shape image in the wavelet and contourlet domains by applying the discrete transforms to a discrete (sampled) version of the image. The plots in Figure 2.2 show the error decay rates of the naive approximations generated in this way from the discrete image partially displayed in Figure 2.1c. We see that this approach generates results that do not follow the theoretical error decay rates in the aforementioned domains. However, we recall that these plots should, in no sense, be interpreted as the approximation error rates of the continuous domain shape images.

The above example prompts us to study systematic techniques for calculating the coefficients of a signal in a domain from its samples in a different domain. This problem is the subject of *consistent reconstruction* that was first introduced in [115] and further improved in [56, 57, 116]. The consistent reconstruction method uses m samples in the sampling domain to calculate m coefficients in the reconstruction domain. This problem has been recently revisited in [1, 2], where it is argued that in general, m samples may not be enough to stably find m coefficients in \mathcal{R} . Also, a new *generalized sampling* approach is developed to stably recover n coefficients in \mathcal{R} from m samples in \mathcal{S} , where usually the stable sampling rate m is larger than n [1–3].

In this chapter, we study consistent reconstruction and generalized sampling (GS) theories. Motivated by the consistent shape reconstruction problem, we limit our study to the piecewise constant (and mostly bilevel) signals in 1D. We will see that due to the linearity of GS, one should expect considerably enhanced signal approximations only when \mathcal{R} , compared to \mathcal{S} , provides faster-converging linear approximations of the signal. In other words, the decay rates of the



(a)

Figure 2.2: Error decay rates of nonlinear approximations of the discrete image partially represented in Figure 2.1c in the contourlet (pyramidal directional filter bank) and 2D discrete wavelet domains.

linear (and not the nonlinear) approximations in \mathcal{R} and \mathcal{S} should be the reference for choosing a reconstruction domain.

To recover signal approximations that benefit from the nonlinear approximation rates in \mathcal{R} , we should calculate a number, say n , of the largest signal coefficients, from a broad range, in \mathcal{R} . We study this problem in the context of *infinite-dimensional compressed sensing* [4], which is an extension of compressed sensing (CS) ideas to the GS theory.

This chapter is organized as follows. In Section 2.2, we define the problem in details and briefly review the GS approach. In Section 2.3, we apply the GS technique to the reconstruction of piecewise constant signals in a number of experiments. We study infinite-dimensional compressed sensing in Section 2.4 and discuss the optimal sampling rates in this theory. We conclude the chapter in Section 2.5.

2.2 Generalized Sampling

2.2.1 Problem definition

Let f be an unknown signal in a Hilbert space¹ \mathcal{H} and suppose that we have access to its measurements

$$\beta_i = \langle f, \phi_i \rangle, \quad i = 1, \dots, m,$$

for a collection of sampling kernels $\{\phi_i\}_{i=1}^m$ in \mathcal{H} . Typically, the sampling kernels are linearly independent and we can assume that they form a Riesz basis for the sampling space $\mathcal{S}_m =$

1. For a complete account of Hilbert spaces and the concepts therein, we refer the readers to the books [81, 118].

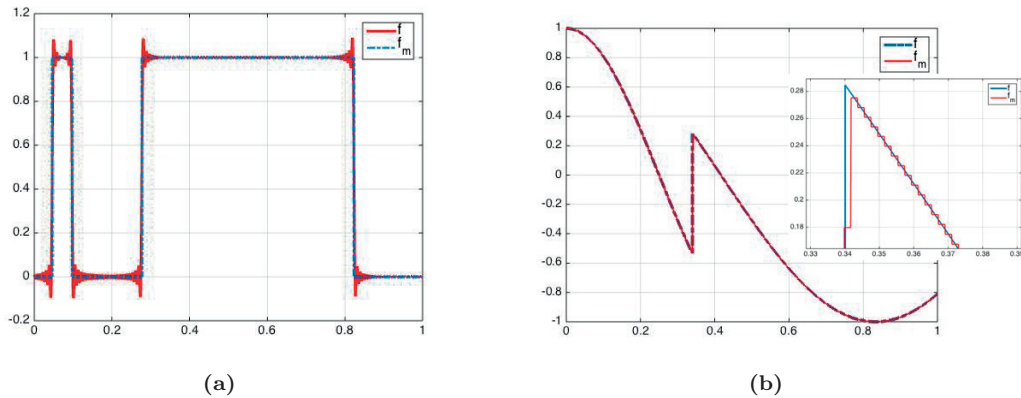


Figure 2.3: (a) Representing a piecewise constant function in terms of a finite number (here, 512) of Fourier exponentials yields the Gibbs Oscillations around the discontinuity points. (b) Representing a piecewise analytic function in terms of a finite number (here, 512) of Haar wavelets results in an undesired staircase appearance.

$\text{span}\{\phi_1, \dots, \phi_m\} \subset \mathcal{H}$. Generally, infinitely many samples are needed to exactly describe f and its approximation with a finite number of samples incurs an error $\|f - P_{\mathcal{S}_m} f\|$ that decays with m , where $P_{\mathcal{S}} f$ denotes the orthogonal projection of f onto \mathcal{S} .

Consider the situation that either $\|f - P_{\mathcal{S}_m} f\|$ decays very slowly or the approximation of f in \mathcal{S}_m generates some undesired features. Examples of the latter are the Gibbs oscillations that appear when representing a function with some discontinuities in terms of Fourier exponentials or the staircase effect of the approximation of a (piecewise) analytic function in terms of Haar wavelets (Figure 2.3).

One approach to improve the signal reconstruction is to represent it in terms of some new kernels $\{\psi_j\}_{j \in \mathbb{N}}$ that are more efficient in representing the signal, *i.e.*, the error of signal approximations in $\mathcal{R}_n = \text{span}\{\psi_1, \dots, \psi_n\}$ decays more rapidly with m . The main challenge in this problem is that, unlike typical scenarios, we do not have immediate access to the original signal but we only observe it through its measurements β_1, \dots, β_m in a different domain and any approximation \hat{f} of f in \mathcal{R} has to be built upon the observed measurements. Accordingly, we impose two requirements on the acceptable signal approximations \hat{f} :

- \hat{f} should be consistent with the available measurements, meaning that $\langle \hat{f}, \phi_i \rangle = \beta_i$, $i = 1, \dots, m$.
- The whole premise of approximating the signal in \mathcal{R} is that we know \mathcal{R} provides faster converging representations for f . Hence, it is vital for \hat{f} to retain the same convergence speed. Mathematically speaking, $\|f - \hat{f}\|$ and $\|f - P_{\mathcal{R}_n} f\|$ should have the same decay rates.

The above discussion brings up the following questions.

1. Given m samples β_1, \dots, β_m , what is the maximum number of coefficients that we can approximate in \mathcal{R} such that $\|f - \hat{f}\|$ enjoys the same decay rate as $\|f - P_{\mathcal{R}_n} f\|$?
2. How can we recover such a stable approximation of f in \mathcal{R} ?

The generalized sampling theory responds to these questions.

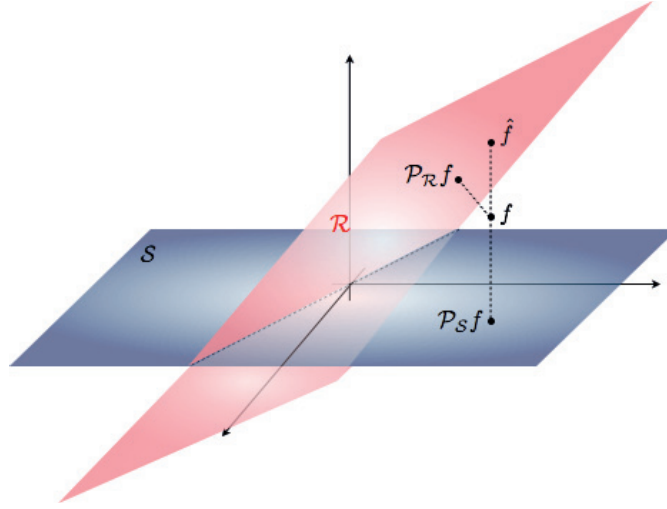


Figure 2.4: Approximation of f in \mathcal{R} from its samples in \mathcal{S} . $P_{\mathcal{R}}f$ is the best approximation of f in \mathcal{R} and \hat{f} is the consistent reconstruction.

2.2.2 Stable signal approximation and the generalized sampling theory

Assume that $\{\phi_i\}_{i=1}^{\infty}$ and $\{\psi_j\}_{j=1}^{\infty}$ form Riesz bases for the sampling and reconstruction spaces $\mathcal{S}, \mathcal{R} \subseteq \mathcal{H}$, respectively. Let $f = \sum_{j=1}^{\infty} \alpha_j \psi_j$ be the signal we wish to recover and suppose that we have access to the infinite collection of samples

$$\beta_1, \beta_2, \beta_3, \dots \quad (2.3)$$

The problem of recovering the best approximation of f in terms of $\{\psi_j\}_{j=1}^{\infty}$ from the samples in (2.3) is equivalent to seeking the best approximation of the coefficients $\boldsymbol{\alpha} = [\alpha_1, \alpha_2, \dots]^T$ from measurements $\boldsymbol{\beta} = [\beta_1, \beta_2, \dots]^T = U\boldsymbol{\alpha}$, with

$$U = \begin{pmatrix} \langle \psi_1, \phi_1 \rangle & \langle \psi_2, \phi_1 \rangle & \dots \\ \langle \psi_1, \phi_2 \rangle & \langle \psi_2, \phi_2 \rangle & \dots \\ \vdots & \vdots & \ddots \end{pmatrix}. \quad (2.4)$$

Before we proceed, we need to recap the following definitions from [1].

Definition 2.1

A mapping $\mathcal{H} \rightarrow \mathcal{R} : f \mapsto \hat{f}$ is called quasi-optimal if there exists a constant $c > 0$ such that

$$\|f - \hat{f}\| \leq c\|f - P_{\mathcal{R}}f\|, \quad \forall f \in \mathcal{H}$$

where $P_{\mathcal{R}}f$ is the orthogonal projection onto \mathcal{R} .

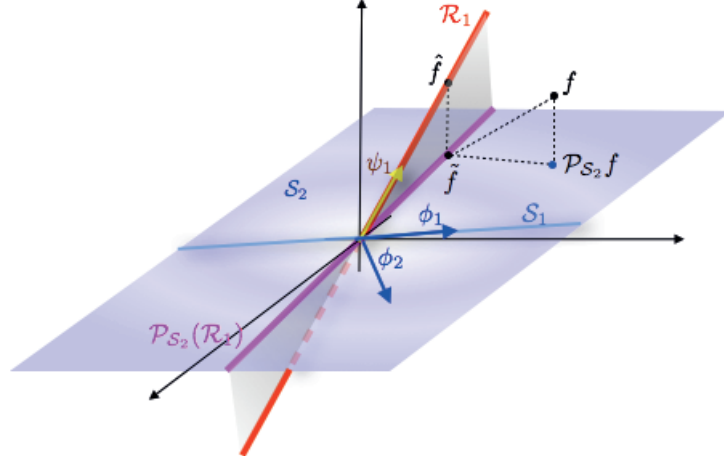


Figure 2.5: Generalized sampling reconstruction \hat{f} of f in \mathcal{R}_1 from samples in \mathcal{S}_2 .

Definition 2.2

Let U and V be closed subspaces of \mathcal{H} . The subspace angle $\theta_{UV} \in [0, \pi/2]$ between U and V is given by

$$\cos(\theta_{UV}) = \inf_{u \in U, \|u\|=1} \|P_V u\|.$$

Definition 2.3

Let U and V be closed subspaces of \mathcal{H} . A mapping $\mathcal{W}_{UV} : \mathcal{H} \rightarrow U$ is an oblique projection onto U along V if $\mathcal{W}^2 = \mathcal{W}$ and $\mathcal{W}(v) = 0, \forall v \in V$.

Consider the linear operator $\mathcal{P} : \mathcal{H} \rightarrow \mathcal{H}$, given by

$$\mathcal{P}f = \sum_{i \in \mathbb{N}} \langle f, \phi_i \rangle \phi_i.$$

When the set $\{\phi_i\}_{i \in \mathbb{N}}$ forms an orthonormal basis, \mathcal{P} coincides with $P_{\mathcal{S}}$. Otherwise, it is a well-defined, bounded and self-adjoint operator.

The consistent reconstruction of f is a point $\hat{f} \in \mathcal{R}$ that generates the same samples $\langle \hat{f}, \phi_i \rangle = \beta_i, i = 1, 2, \dots$, and hence

$$\hat{f} \in \mathcal{R} \quad \text{s.t.} \quad \mathcal{P}_{\mathcal{S}} \hat{f} = \mathcal{P}_{\mathcal{S}} f. \quad (2.5)$$

When the two subspaces satisfy $\mathcal{R} \oplus \mathcal{S}^{\perp} = \mathcal{H}$, equation (2.5) has a unique solution $\hat{f} = \sum_{j \in \mathbb{N}} \alpha_j \phi_j$ that can be found by solving the infinite-dimensional system of linear equations $U\alpha = \beta$ [56, 57, 115]. The mapping $\mathcal{H} \rightarrow \mathcal{R} : f \mapsto \hat{f}$ is quasi-optimal and coincides with the oblique projection $\mathcal{W}_{\mathcal{R}, \mathcal{S}^{\perp}}$. More specifically, it satisfies

$$\|f - P_{\mathcal{R}} f\| \leq \|f - \mathcal{W}_{\mathcal{R}, \mathcal{S}^{\perp}} f\| \leq \frac{1}{\cos(\theta_{\mathcal{R}\mathcal{S}})} \|f - P_{\mathcal{R}} f\|.$$

Figure 2.4 depicts the concept of consistent reconstruction in \mathbb{R}^3 .

Clearly in practice, we have access to a finite number of samples. Therefore, we must consider truncations of this linear system and seek the first n coefficients α^n of α . This is equivalent to looking for the n -term linear approximation of f in \mathcal{R} , *i.e.*, $\hat{f}_n = \sum_{j=1}^n \alpha_j \psi_j$.

We may think of solving this problem by taking $m = n$ samples in \mathcal{S} and considering the consistency condition in the m -dimensional subspace \mathcal{S}_m :

$$\hat{f} \in \mathcal{R}_m \text{ s.t. } \langle \hat{f}, \phi_i \rangle = \beta_i, \quad i = 1, \dots, m. \quad (2.6)$$

This approach has a stable solution only if

$$\mathcal{R}_m \oplus \mathcal{S}_m^\perp = \mathcal{H}. \quad (2.7)$$

The condition in (2.7) is equivalent to $\cos(\theta_{\mathcal{R}_m \mathcal{S}_m}) \neq 0$. In general, this condition may not hold for an arbitrary m , even if the infinite-dimensional spaces satisfy $\mathcal{R} \oplus \mathcal{S}^\perp = \mathcal{H}$. Indeed, either $\cos(\theta_{\mathcal{R}_m \mathcal{S}_m}) \geq \cos(\theta_{\mathcal{R} \mathcal{S}})$ or $\cos(\theta_{\mathcal{R}_m \mathcal{S}_m}) \leq \cos(\theta_{\mathcal{R} \mathcal{S}})$ are possible and there is even no general guarantee that $\cos(\theta_{\mathcal{R}_m \mathcal{S}_m})$ stays away from zero as $m \rightarrow \infty$ [2].

The generalized sampling approach to this problem is to decrease the number of coefficients $n < m$ (equivalently, increase the number of samples $m > n$) such that the condition $\cos(\theta_{\mathcal{R}_n \mathcal{S}_m}) \neq 0$ is met. In this case, the projection of \mathcal{R}_n onto \mathcal{S}_m is an n dimensional subspace $\mathcal{P}_{\mathcal{S}_m}(\mathcal{R}_n) = \text{span}\{\mathcal{P}_{\mathcal{S}_m} \psi_j\}_{j=1}^n$. Now, we find an approximation of $P_{\mathcal{R}_n} f$ by verifying the consistency condition in this subspace [1]

$$\hat{f} \in \mathcal{R}_n \text{ s.t. } \langle \hat{f}, \mathcal{P}_{\mathcal{S}_m} \psi_j \rangle = \langle f, \mathcal{P}_{\mathcal{S}_m} \psi_j \rangle. \quad (2.8)$$

Note that $\langle f, \mathcal{P}_{\mathcal{S}_m} \psi_j \rangle = \langle \mathcal{P}_{\mathcal{S}_m} f, \psi_j \rangle$ can be derived from the samples.

In Figure 2.5, we explain the GS reconstruction through an example in \mathbb{R}^3 . In this example, we find the approximation of f in \mathcal{R}_1 from two samples in \mathcal{S}_2 . Note that since \mathcal{R}_1 is orthogonal to $\mathcal{S}_1 = \text{span}\{\phi_1\}$, one sample of f in \mathcal{S}_1 is not sufficient for the stable approximation of f in \mathcal{R}_1 . This is while $\cos(\theta_{\mathcal{R}_1 \mathcal{S}_2}) > 0$ with $\mathcal{S}_2 = \text{span}\{\phi_1, \phi_2\}$. Consequently, we can find a quasi-optimal representation of f in \mathcal{R}_1 from its samples in \mathcal{S}_2 . The final reconstruction is an oblique projection onto \mathcal{R}_n along $[\mathcal{P}_{\mathcal{S}_m}(\mathcal{R}_n)]^\perp$ [1].

The solution of the GS equation in (2.8) is a stable approximation of f in \mathcal{R}_n and it satisfies

$$\|f - P_{\mathcal{R}_n} f\| \leq \|f - \hat{f}\| \leq \frac{1}{\cos(\theta_{\mathcal{R}_n, \mathcal{P}_{\mathcal{S}_m}(\mathcal{R}_n)})} \|f - P_{\mathcal{R}_n} f\|. \quad (2.9)$$

Also, the coefficients of \hat{f} can be calculated as

$$\alpha^n = ((U^{m,n})^* U^{m,n})^{-1} (U^{m,n})^* \beta^m, \quad (2.10)$$

where $U^{m,n}$ is the $m \times n$ subsection of U in (2.4). We remark that the generalized sampling condition in (2.8) reduces to consistent reconstruction (2.6) when $m = n$. Extension of GS results to frames and inverse problems can be found in [5].

For a fixed number n of desired coefficients in \mathcal{R} , the stable sampling rate is the minimum required number of samples that bounds the factor $\left(\cos(\theta_{\mathcal{R}_n, \mathcal{P}_{\mathcal{S}_m}(\mathcal{R}_n)})\right)^{-1}$ in (2.9) between the GS and the optimal reconstructions in \mathcal{R}_n . One can employ the theorems in [1, 3] to numerically calculate this factor for any pair \mathcal{S}_m and \mathcal{R}_n , by having access to $U^{m,n}$ and the Gram matrices

of the basis functions $\{\phi_i\}_{i=1}^m$ and $\{\psi_j\}_{j=1}^n$. However, analytic bounds should be calculated on a case by case basis. For example, it is shown that for stable and accurate reconstruction of polynomials of degree less than n (i.e., when $\mathcal{R}_n = \mathbb{P}_{n-1}$) from Fourier samples, the number of samples should grow like $m \sim n^2$ [3]. Moreover, the stable sampling rates for the reconstruction in the wavelet domains from Fourier samples scale linearly with the number of desired wavelet coefficients [7]. The linear scaling of the stable sampling rate is preserved when both wavelet and Fourier domains are lifted up to 2D by tensor products [6].

As a final remark in this section, we recall that the GS reconstruction in (2.8) does not preserve full measurement consistency. A consistent and stable solution to the GS problem for orthonormal sampling and reconstruction kernels is proposed in [93], which replaces the linear reconstruction in (2.10) with a nonlinear basis pursuit problem.

2.3 Reconstruction of Piecewise Constant Signals

2.3.1 Error decay rates

In this section, we apply the GS technique to reconstruct piecewise constant signals from their measurements in two different scenarios. First, we aim at investigating the quasi-optimality of the GS reconstructions in the Fourier and wavelet domains. For this purpose, we invoke the error decay rates for the approximation of discontinuous signals in these domains.

Theorem 2.1 ([81], Chapter 9)

Let $f \in \mathcal{H} = L^2[0, 1]$ be a discontinuous signal with bounded variations, i.e.,

$$\|f\|_V = \int_0^1 |\dot{f}(x)| dx < +\infty,$$

where \dot{f} represents the derivative (in the distributional sense). Then, the errors of the n -term linear and nonlinear approximations of f in the Fourier domain satisfy

$$e_l^F(n, f) = e_n^F(n, f) = O(\|f\|_V^2 n^{-1}).$$

Also, the wavelet approximation errors satisfy

$$e_l^W(n, f) = O(\|f\|_V^2 n^{-1})$$

and

$$e_n^W(n, f) = O(\|f\|_V^2 n^{-2}).$$

In the first experiment, the sampling kernels are the linear B-spline wavelets and the reconstruction kernels are Fourier exponentials or Haar wavelets. In either case, the infinite-dimensional sampling and reconstruction spaces span $\mathcal{H} = L^2[0, 1]$ and hence, $\mathcal{R} \oplus \mathcal{S}^\perp = \mathcal{H}$.

The experiment setup is as follows. We generate piecewise constant signals with 6 randomly distributed discontinuity points and random levels. We set the number of reconstruction coefficients to $n = 512$. For the reconstruction in the Fourier domain, we take $m = n$. This results in $\cos(\theta_{\mathcal{R}_n, \mathcal{S}_m(\mathcal{R}_n)}) = 0.72$ which assures that the error of the GS reconstruction is less than 1.4 times the optimal error. For the reconstruction in the Haar domain, we test $m = n$ and $m = 2n$,

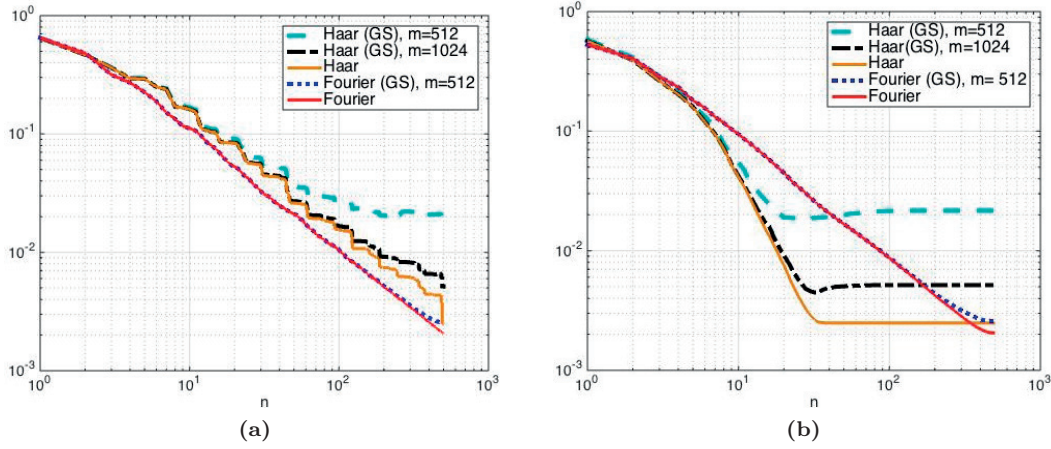


Figure 2.6: The n -term (a) linear and (b) nonlinear approximation errors of piecewise constant signals in the Fourier and Haar wavelet domains. The plots compare error decay rates of the GS approximations (calculated from m signal measurements generated with the linear B-spline sampling kernels) and the original approximations (generated immediately from the signal).

which correspond to $\cos(\theta_{\mathcal{R}_n, \mathcal{P}_{S_m}(\mathcal{R}_n)}) = 0.10$ and $\cos(\theta_{\mathcal{R}_n, \mathcal{P}_{S_m}(\mathcal{R}_n)}) = 0.86$, respectively. We solve (2.10) to find the (approximate) Fourier and wavelet coefficients. Finally, we compute n -term linear and nonlinear approximations of f in both domains for $1 \leq n \leq 512$.

Figure 2.6 displays the average linear and nonlinear approximation errors versus n for 10 realizations of the signal in a logarithmic scale. For comparison, we have also plotted the same quantities using the Fourier and Haar coefficients that are calculated from the original signals. The plots clearly confirm the theoretical error decay rates of Theorem 2.1.

A point that is worth noting here is that the (average) error of the final GS reconstructions (using all the $n = 512$ coefficients) is less in the Fourier domain, even compared to the reconstruction in the Haar domain that exploits twice as many samples. This has two reasons: (1) In case of including all the n coefficients, we obtain a linear approximation of the signal, for which the order of the error with Fourier coefficients coincides with that of the wavelet coefficients. (2) The disparity between a pair of sampling and reconstruction domains has an influence on the quality of the signal approximations in the reconstruction domain. In the GS theory, this is encoded in the angle between the two spaces, or more specifically, the factor $\left(\cos(\theta_{\mathcal{R}_n, \mathcal{P}_{S_m}(\mathcal{R}_n)})\right)^{-1}$ in (2.9).

2.3.2 Reconstruction of binary signals

In the second experiment, we focus on the reconstruction of binary (bilevel) signals with random discontinuity points in the Fourier and Haar wavelet domains. The conventional wisdom suggests that the Haar domain provides better representations for bilevel signals. To investigate this, we consider signal approximations in each of the two domains using $m = 512$ samples. We additionally use GS to switch from one domain to another and calculate the quasi-optimal signal approximations with $n = m$ coefficients. Knowing a priori that the original signals are binary,

Table 2.1: Approximation errors of bilevel signals in the Fourier and Haar domains (avg. 100 trials)

Approximation domain	Fourier	Fourier (GS)	Haar	Haar (GS)
Before thresholding	0.0281	0.0306	0.0355	0.0391
After thresholding	0.0018	0.0191	0.0433	0.0433

we also apply a threshold to each of the signal approximations.

Figure 2.7 shows a bilevel signal and its immediate and quasi-optimal (using GS technique) approximations in the Fourier F_{512} and Haar H_{512} domains. The reported approximation errors $\|f - \hat{f}\|_2$ indicate that the orthogonal and quasi-optimal approximations of the signal in the Fourier domain are superior to the signal reconstructions in the Haar wavelet domain. Moreover, thresholding the signal approximations affects differently the results in the two domains: it improves signal approximations in the Fourier domain while it worsens the ones in the Haar domain. In Table 2.1, we summarize the average of the same approximation errors for 100 random bilevel signals with 4 discontinuities in the interval $[0, 1]$. The numbers in this table also validate the same findings. Specifically, we observe that thresholding the Fourier approximations recovers the exact bilevel signal in most cases.

2.4 Nonlinear Signal Approximation

The GS technique is a linear process which at best recovers n -term linear approximations of a signal in a desired domain, where $n \leq m$ is ruled by the stable sampling rate between the sampling and reconstruction domains. Thus, we should not expect considerably better signal approximations if we switch between two domains with similar linear approximation rates, even though the reconstruction domain offers a better nonlinear approximation rate². The reconstruction of discontinuous signals in the Fourier and wavelet domains that we studied in the last section was an example of this situation.

Usually, representation of a signal in a multiresolution domain \mathcal{R} leads to a coefficient vector α that is sparse (or compressible) but the significant coefficients are spread along different resolutions. As a result, the signal is effectively approximated by its largest coefficients in \mathcal{R} , whereas the first coefficients in α produce poor signal reconstructions. This motivates the approximation of the most significant signal coefficients in \mathcal{R} from the available samples. Similar to the finite-dimensional compressed sensing (CS) [29, 49], we are interested to take advantage of the sparsity of coefficients to reduce the number of samples (equivalently, to recover larger number of significant coefficients from a fixed budget of samples).

This problem can be considered as an infinite-dimensional variant of the CS problem where the goal is to recover a sparse vector \mathbf{x} from linear measurements $\mathbf{y} = U_{m \times n} \mathbf{x}$. It is shown that if the sensing matrix $U_{m \times n}$ has the so-called *restricted isometry property* (RIP) of order $2k$, any k -sparse vector \mathbf{x} can be uniquely recovered from the measurements $\mathbf{y} = U_{m \times n} \mathbf{x}$ [28], by solving

² An exception is when the signals in question live in the finite-dimensional subspace \mathcal{R}_n in which case we can perfectly recover them in \mathcal{R}_n . However, this scenario is better classified as signals with finite rate of innovation [119].

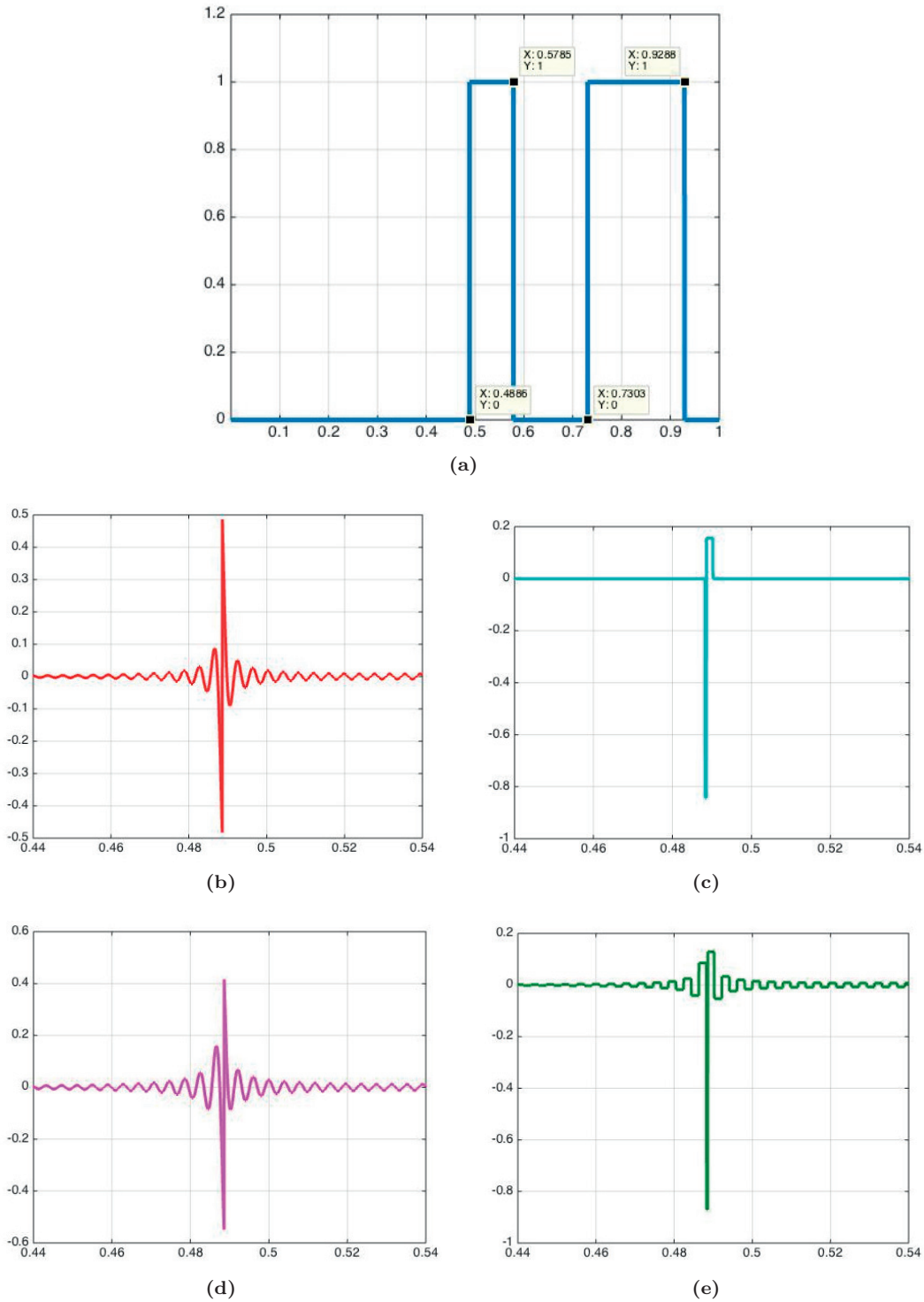


Figure 2.7: Example of a bilevel signal and its approximations in the Fourier and Haar wavelet domains using 512 coefficients. (a) Bilevel signal with discontinuity points marked on the signal. Error $f - \hat{f}$ between the signal and (b) its orthogonal projection onto F_{512} , (c) its orthogonal projection onto H_{512} , (d) its approximation in F_{512} , calculated from 512 Haar wavelet coefficients, and (e) its approximation in H_{512} , calculated from 512 Fourier coefficients, in the interval $[0.44, 0.54]$. The corresponding errors $\|f - \hat{f}\|_2$ before (after) thresholding are 0.0281 (0), 0.034304 (0.040594), 0.030381 (0.019136) and 0.037459 (0.040594), respectively.

the *basis pursuit* problem

$$\begin{aligned} \min_{\mathbf{x} \in \mathbb{R}^n} \|\mathbf{x}\|_1 \\ \text{s.t. } \mathbf{y} = U_{m \times n} \mathbf{x}. \end{aligned}$$

However, verifying the RIP condition for a matrix is computationally hard. In [27], Candès and Romberg considered orthonormal matrices $U = [u_{i,j}]_{n \times n}$ and they showed that in this case the coherence

$$\mu(U) = \max_{i,j} |u_{i,j}|$$

can be used to determine the subsampling rate m .

The infinite-dimensional CS approach was recently introduced in [4] as an extension of the CS ideas to GS. In this theory, a set of n -sparse coefficients in \mathcal{R} with the support of nonzero coefficients in $\{1, \dots, N\}$ for some large $N \in \mathbb{N}$ are recovered with high probability from m samples in \mathcal{S} chosen uniformly at random from the range $\{1, \dots, M\}$ by solving the basis pursuit problem. The subsampling rate m depends on the coherence of the underlying sensing matrix. In addition, the parameters (N, n, M, m) should satisfy a *balancing property*.

The infinite-dimensional CS is a promising framework that allows us to obtain far better approximations of signals and images, in the applications that the three ingredients (*asymptotic sparsity*, (*asymptotic*) *incoherence* and *uniform or multilevel random subsampling*) are present. In this section, we briefly study the theory and the balancing property in the infinite-dimensional CS. We also study the change of m as a function of M for the Fourier and Haar wavelet domains and discuss the optimum choices of sampling rate and support for limited choices of (N, n) .

2.4.1 Infinite-dimensional compressed sensing

Let f denote a signal with a sparse representation $f = \sum_{j \in \mathbb{N}} \alpha_j \psi_j$ in a known domain \mathcal{R} . We can assume that the significant values of α belong to the range $\Delta \in \{1, \dots, N\}$ for a large N . In this case, we can perfectly recover f with the GS approach, if we have access to a sufficient number of samples $m \geq N$. But considering the order of N , having these many samples is impractical. The infinite-dimensional CS approach in [4] exploits the sparsity of α to reduce the number of samples. The price of the subsampling, however, is to trade the stable recovery in GS with a probabilistic recovery.

Before recalling the main results in [4] for recovery of sparse or compressible signals in \mathcal{R} , we need to define the balancing property.

Definition 2.4 ([4])

Let U be the isometry matrix in (2.4). Then M and m satisfy the balancing property with respect to U, N and n if

$$\begin{aligned} \|P_N U^* P_M U P_N - P_N\| &\leq \left(4\sqrt{\log_2(4M\sqrt{n}/m)}\right)^{-1}, \\ \max_{|\Delta|=n, \Delta \subset \{1, \dots, N\}} \|P_N P_\Delta^\perp U^* P_M U P_\Delta\|_{mr} &\leq \frac{1}{8\sqrt{n}}, \end{aligned}$$

where $\|\cdot\|_{mr}$ and P_N denote the maximum ℓ^2 norm among the rows of U and the projection onto $\text{span}\{\mathbf{e}_j : j = 1, \dots, N\}$, respectively.

The following theorem considers the case that the compressible coefficient vector α with the support in $\{1, \dots, N\}$ can be decomposed as

$$\alpha = \alpha_0 + \alpha_1,$$

where α_0 is n -sparse and α_1 has small ℓ_1 norm. Here, $U_\Omega^{M \times N}$ indicates the restriction of $U^{M \times N}$ to the rows indexed by Ω .

Theorem 2.2 ([4])

Let U be an isometry matrix with coherence $\mu(U)$. Let the coefficients $\alpha \in \ell^1(\mathbb{N})$ in \mathcal{R} can be written as $\alpha = \alpha_0 + \alpha_1$ with $\alpha_0, \alpha_1 \in \ell^1(\mathbb{N})$ and $\text{supp}(\alpha_0) = \Delta \subset \{1, \dots, N\}$ and $\text{supp}(\alpha_1) = \{1, \dots, N\}$. Also, let $\epsilon > 0$ and $\Omega \subset \{1, \dots, M\}$ be chosen uniformly at random with $|\Omega| = m$. If $\beta = U\alpha$ and $\hat{\alpha}$ is a minimizer of

$$\inf_{\eta \in \ell^1(\mathbb{N})} \|\eta\|_{\ell^1} \quad \text{s.t.} \quad U_\Omega^{M \times N} \eta^N = \beta_\Omega, \quad (2.13)$$

then with probability exceeding $1 - \epsilon$ we have

$$\|\hat{\alpha} - \alpha\| \leq \left(\frac{20M}{m} + 11 + \frac{m}{2M} \right) \|\alpha_1\|_{\ell^1},$$

given that $(N, |\Delta|, M, m)$ satisfy the balancing property and m satisfies

$$m \geq CM\mu^2(U)|\Delta|(\log(\epsilon^{-1}) + 1) \log \left(\frac{MN\sqrt{|\Delta|}}{m} \right), \quad (2.14)$$

for a universal constant C .

In case that $\alpha_1 = 0$ and α is a n -sparse vector with $n = |\Delta|$, the equation (2.13) has a unique solution that coincides with α with probability greater than $1 - \epsilon$.

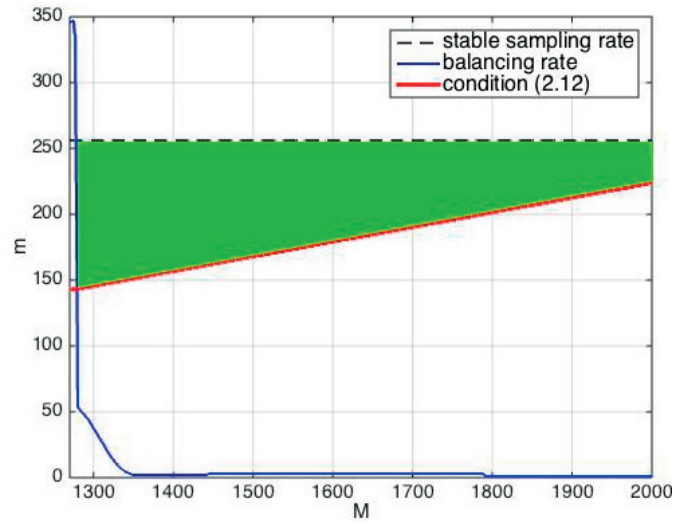
2.4.2 Optimal sampling rate

Theorem 2.2 indicates that a signal with a n -sparse representation in \mathcal{R}_N can be recovered with high probability from m random samples in \mathcal{S}_M , if m fulfills the condition in (2.14) and (N, n, M, m) satisfy the balancing property with respect to U . The condition (2.14) is a standard requirement in CS with a simple structure that relates the subsampling rate m/M to the coherence of U . On the other hand, it is not clear which values of (N, n, M, m) satisfy the balancing property with respect to a given U and how changes in (N, n) affect the sampling rate m and sampling support M . In other words, it is not clear what the subsampling gain of this setting is with respect to the stable sampling rate of GS, for a given sparsity.

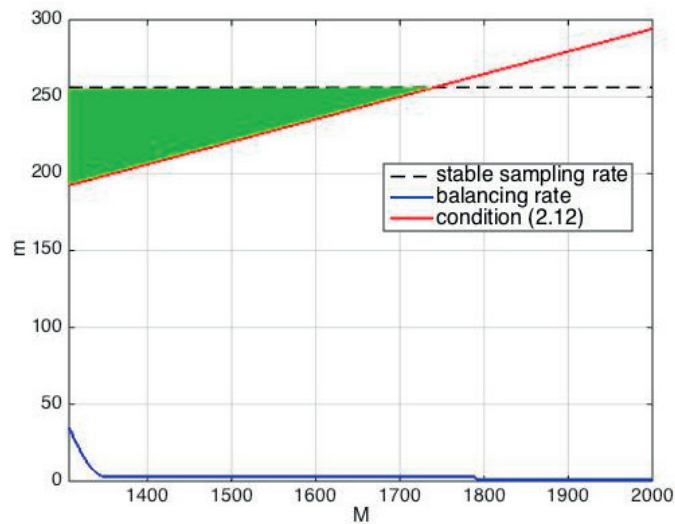
In this section, we investigate the balancing property when the underlying sampling and reconstruction domains are formed by Fourier exponentials and Haar wavelet functions in $L^2[0, 1]$. This special choice of basis functions has applications in the MRI problem [6, 7]. In our study we consider the following more convenient but stronger variant of (2.12) [4]

$$\|P_N U^* P_M U P_N - \text{diag}(P_N U^* P_M U P_N)\|_{mr} \leq \frac{1}{8\sqrt{n}}. \quad (2.15)$$

We use the following setup to find efficient sampling rates for fixed pairs of N and n . First, we find all values of M in the range $\{n, n+1, \dots, M_{\max}\}$ such that the submatrix $U^{M \times N}$ satisfies the



(a)



(b)

Figure 2.8: The acceptable range of sampling rate m and sampling support M for samples in the Fourier domain and sparse coefficients in the Haar domain, $N = 200$ and (a) $n = 30$, (b) $n = 40$. The blue and red plots display the minimum values of m as a function of M that are given by the balancing property and equation (2.14) with $\epsilon = 0.05$, respectively. The dashed lines show the stable sampling rates in GS. The green regions display the acceptable ranges of (M, m) .

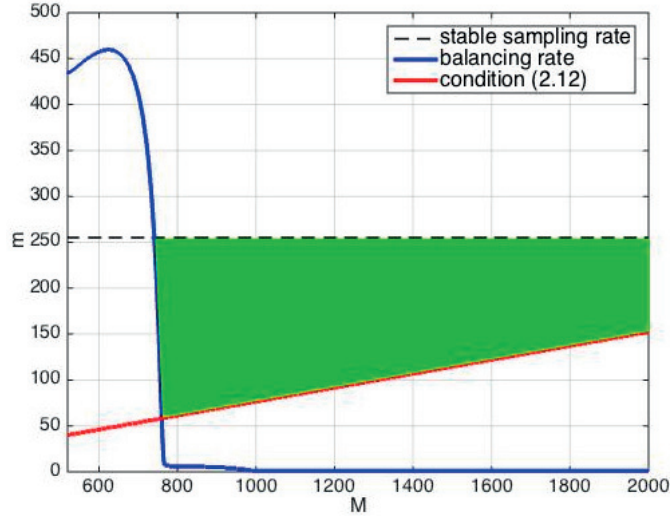


Figure 2.9: The acceptable range of sampling rate m and sampling support M for samples in the Haar domain and sparse Fourier coefficients with $N = 200$ and $n = 20$.

constraint in (2.15). An ideal choice for M_{\max} is to take it proportional to the stable sampling rate corresponding to N . However, we will see that the specific choices of sampling and reconstruction kernels in this section asks for considerably larger values M . We further point out that in general, the maximum row norm in equation (2.15) does not change monotonically with M . Thus, we should find the acceptable values of M by checking all numbers in $\{n, n + 1, \dots, M_{\max}\}$.

In the next step, for each verified M , we find the minimum m that satisfies the balancing property and the equation (2.14). Finally, we accept the pair (M, m) if $m < \min(M, M_1)$ where M_1 denotes the stable sampling rate in GS corresponding to N .

Figures 2.8a and 2.8b display the acceptable pairs (M, m) for $N = 200$, $M_{\max} = 2000$ and two different sparsity values $n = 30, 40$, for sampling in Fourier and reconstruction in Haar domains. Figure 2.9 depicts the same variables for $n = 20$, when the sampling and sparsity domains are reversed. In these figures, the minimum values of m as a function of M satisfying the balancing property and the equation (2.14) are indicated in blue and red, respectively. The error probability is $\epsilon = 0.05$. Also, the dashed lines display the stable sampling rates corresponding to $N = 200$.

The green region in each figure shows the acceptable range of (M, m) . The figures indicate that for a given setup, there are various pairs which provide high probability of reconstruction. A counter intuitive result is that the required number of samples m does not necessarily decrease as M increases. For fixed values of (N, n) , the optimal sampling rate is determined by the point that corresponds to the smallest m . For instance, Figure 2.9 shows that a signal with 20-sparse Fourier coefficients in the range $\{1, \dots, 200\}$ can be recovered with probability greater than 0.95 from 58 samples that are chosen uniformly at random from the first 760 coefficients in the Haar domain. This means that we get a large subsampling gain by solving the basis pursuit problem in equation (2.13). On the other hand, Figure 2.8b illustrates that we do not get too much subsampling gain by replacing the stable reconstruction in GS with the basis pursuit problem in (2.13) for the specific values of the parameters in this plot.

For the specific pairs of sampling and reconstruction domains discussed here, the balancing

Table 2.2: The approximation errors for the wavelet coefficients (avg. 100 trials)

	$\ \boldsymbol{\alpha} - \hat{\boldsymbol{\alpha}}\ _{\ell_\infty} / \ \boldsymbol{\alpha}\ _{\ell_\infty}$	SNR
Noiseless coefficients	0.1024×10^{-6}	104 dB
Noisy coefficients	0.7921×10^{-3}	64.1 dB

property mostly leads to inappropriate sampling ranges or subsampling rates. On the contrary, it has been shown [9, 93] that for Fourier samples and sparse coefficients in a sufficiently smooth wavelet domain (specifically, when the wavelet and scaling functions are q times continuously differentiable for $q \geq 2$), the balancing property holds whenever

$$M = C \cdot N \cdot \left(\log_2(4NM\sqrt{n}/m) \right)^{1/(4q-2)}.$$

For further details on this topic as well as the hacks for matrices with large coherence (asymptotic incoherence and multilevel random subsampling), we refer the readers to the references [8, 9, 93].

2.4.3 Numerical experiments

In this section, we use the optimal values of (M, m) in Figure 2.8a to recover signals having sparse representations in the wavelet domain from randomly chosen Fourier coefficients.

In the first experiment, we consider signals of the form

$$f(t) = \sum_{i=1}^{200} \alpha_i \phi_i(t),$$

with only 20 nonzero coefficients, where $\{\phi_i(t)\}_{i \in \mathbb{N}}$ are Haar wavelets on $[0, 1]$. In the second experiment we consider signals of the form

$$f(t) = \sum_{i=1}^{200} \alpha_{0,i} \phi_i(t) + \sum_{i=1}^{200} \alpha_{1,i} \phi_i(t),$$

where the coefficient vector $[\alpha_{0,1}, \dots, \alpha_{0,200}]^T$ is 20-sparse and $[\alpha_{1,1}, \dots, \alpha_{1,200}]^T$ has a small ℓ_1 norm. For each case, we take $m = 144$ Fourier samples chosen uniformly from the first 1280 Fourier coefficients and we recover the signal by finding the solution to (2.13). Table 2.2 summarizes the approximation errors in the wavelet coefficients. The results in this table are averages over 100 trials.

2.5 Conclusion

We studied the sampling problem of signals in Hilbert spaces that have efficient representations in a known domain. While an enforced set of sampling kernels is likely to yield poor signal approximations, adapting the representation kernels to the signal can improve the approximations. GS scheme allows us to switch between the sampling and reconstruction domains. But, the signal approximations within this framework, in the best case, enjoy linear approximation rates of the reconstruction domain. To benefit from nonlinear approximation rates, we need

an approach that calculates the most significant signal coefficients from the available samples. Infinite-dimensional CS is a technique that approximates the few (n) largest signal coefficients in a fixed range $\{1, \dots, N\}$ by adopting the random sampling approach of CS. Unlike the finite-dimensional case, the sampling scheme involves a pair (M, m) , where m samples are randomly chosen among a size M subset of possible sampling kernels. The balancing property determines the acceptable values of (N, n, M, m) for a pair of sampling and reconstruction domains.

Infinite-dimensional CS is a promising framework for recovering efficient signal approximations in the applications that the three ingredients asymptotic sparsity, asymptotic coherence and random sampling are present. However, in many practical sensing devices such as conventional digital cameras, the sampling pattern is fixed and it is impossible to ask for random sampling. In the next chapters, we study nonlinear but deterministic approaches to the consistent shape reconstruction problem.

Chapter 3

A Robust Sampling Scheme for Shapes with Algebraic Boundaries

3.1 Introduction

The contours of a shape image can be described using various functions [73]. In this chapter, we model the image contours with algebraic curves and develop sampling results for this class of shape images. The reason for the choice of this model becomes evident shortly in the next subsection.

3.1.1 Motivation

An algebraic curve is the zero level set of a finite degree bivariate polynomial. Algebraic curves can be decomposed into a finite number of smooth arcs. Nevertheless, they are dense, in the Hausdorff metric, among all smooth curves which means that every curve can be approximated by a sequence of algebraic curves arbitrarily closely [66]. This characteristic makes them an excellent candidate in modeling general image boundaries.

We call a subset of the 2D plane with an algebraic boundary curve an *algebraic domain* and the restriction of it to the image plane an *algebraic shape*. According to a classical result [70, 75], an algebraic domain of degree n can be uniquely determined from its set of 2D moments of order less than or equal to n . But as stated in [86], "there has been so far no constructive way of passing from the given moments to the unique algebraic domain, or equivalently to the defining polynomial". In [86] and [67], the authors present an algorithm for the reconstruction of a subset of bounded algebraic domains –called quadrature domains– from their moments. However, moments are inherently very sensitive to noise and consequently, the suggested algorithm (as noted by the authors) suffers from severe numerical instabilities.

Moments have been used as the standard descriptors of 2D shapes in [44, 94, 112]. Also, there are some works on the exact calculation of moments of the shapes with parametric boundary curves in terms of the curve parameters, through nonlinear equations. Examples are [101] for polygonal shapes and [69] for shapes with wavelet and spline curves.

0. This chapter includes research conducted jointly with Arash Amini and Martin Vetterli [60].

3.1.2 Contribution

In this chapter, we propose sampling and reconstruction techniques for algebraic shapes. We first derive a set of linear annihilation equations for shape parameters with coefficients being factors of 2D moments of the image. We prove that any solution of these equations will lead to a polynomial that vanishes on the boundaries of the original shape. By employing sampling kernels that reproduce polynomials like the well-known B-splines [113], we are able to calculate the shape moments from the samples.

Moments are inherently very sensitive to the noise and the reason is that noise in the image or the samples is boosted by polynomial factors before it contaminates the moments. The noise sensitivity of the moments makes the reconstruction process numerically unstable and narrows the choice of the sampling kernels to polynomial reproducing kernels. As a remedy to this problem, we replace moments with some generalized moments that are still reproducible from the samples but do not amplify the noise. This is achieved by multiplying the monomials in the conventional moments with a function that is adjusted to the sampling kernel and decays at the image borders. The benefits are threefold: (1) it relaxes the requirements on the sampling kernels, (2) it produces annihilation equations that are robust at numerical precision, and (3) it extends the results to images with unbounded boundaries.

In any sampling problem, consistency of the reconstruction with noiseless samples is a crucial constraint [109, 115, 116]. It is also proved to be a strong tool for recovering bilevel images in the absence of a parametric model [59]. In this work, we further improve the stability of our reconstruction by enforcing measurement (or sample) consistency to the recovered algebraic shape. This results in a reconstruction algorithm that is robust to moderate noise levels in the samples.

The outline of this chapter is as follows. In Section 3.2, we first define the image model and study algebraic curves in details. Then, we explicitly define the sampling problem. We derive the annihilation equations for the shape parameters in Section 3.3 and present a perfect reconstruction algorithm for the noiseless scenario. In Section 3.4, we develop a stable reconstruction algorithm. For this purpose, we introduce the notion of generalized moments and present an algorithm for generating the adequate generalized moments corresponding to the given sampling kernel. Also, we prove that any solution of the annihilation equations formed from (generalized) moments generates the original shape boundaries. We present some experimental results with different curves in the noiseless and noisy scenarios in Section 3.5 and conclude in Section 3.6.

3.2 Sampling of Algebraic Shapes

3.2.1 Image model

Consider a bivariate polynomial of degree n with real coefficients $a_{i,j}$

$$p(x, y) = \sum_{0 \leq i, j, i+j \leq n} a_{i,j} x^i y^j. \quad (3.1)$$

The set of points $\{(x, y) \in \mathbb{R}^2 : p(x, y) \leq 0\}$ defines an algebraic domain. The boundary of this domain, defined by the zero level set of p , is an algebraic curve of degree n ,

$$\mathcal{C} = \{(x, y) \in \mathbb{R}^2 : p(x, y) = 0\}.$$

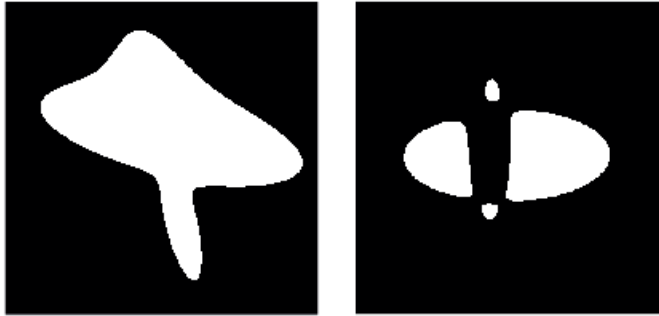


Figure 3.1: Algebraic domains of degree 4.

Let Ω denote a closed domain in \mathbb{R}^2 modeling the image plane. Without loss of generality, we take $\Omega = [-L, L]^2$ for some $L \in \mathbb{Z}^+$. We define an algebraic shape in Ω as the binary image

$$I(x, y) = \chi_{\{p(x, y) \leq 0\}}, \quad (x, y) \in \Omega. \quad (3.2)$$

This means that the edges of I are contained in the algebraic curve \mathcal{C} .

An algebraic shape of degree n is specified with $\binom{n+2}{2}$ parameters (the coefficients in (3.1)). In developing the annihilation equations of Section 3.3, we assume that the algebraic shapes have closed boundaries. This restricts the polynomial degree to the even integers. We later remove this assumption by introducing generalized moments in Section 3.4.

Typical examples of algebraic domains of degree 2 are circles and ellipses. Figure 3.1 displays two algebraic domains of degree 4. We see in this figure that an algebraic domain of degree 4 can have four disconnected components. The following remark asserts that this is an upper bound.

Remark 3.1 ([72])

An algebraic domain of degree n cannot have more than n disconnected closed components.

This remark is a consequence of Bezout's theorem [121]. We will also make use of this theorem in Section 3.4 to prove our result.

Theorem 3.1 (*Bezout*)

Two algebraic curves of degree n and m that do not share a common component intersect in at most mn points.

Bezout's theorem also provides us a handy tool to roughly estimate the degree of an algebraic shape. Consider a shape image I with boundary \mathcal{C} . \mathcal{C} should have a degree of at least n if it intersects a line (a first-degree polynomial) at n points or if it intersects an ellipse (a polynomial of degree 2) at $2n$ points. This is illustrated with an example in Figure 3.2.

Algebraic curves have been studied and applied to data fitting and object recognition in computer vision (*e.g.* [72, 106, 108]). This rather long history of application has revealed that polynomials of modest degree (*e.g.* degree 4 with 15 parameters) have enough descriptive power to generate a diverse range of curve geometries. Hence, in the rest of this chapter, we mostly consider $n \leq 4$. Nevertheless, all results remain valid for higher degree polynomials.

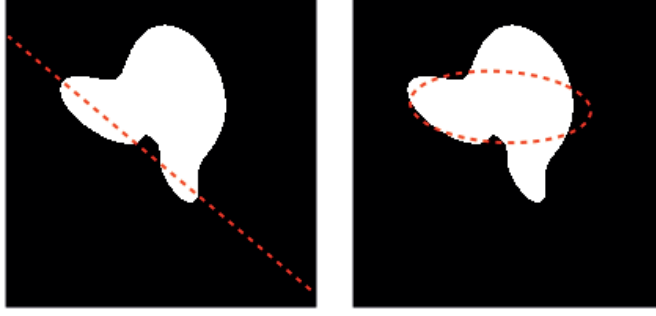


Figure 3.2: An algebraic shape of degree at least 4.

3.2.2 Sampling

In a typical sampling setup (Figure 1.1), the image is first convolved with a 2D kernel and then sampled at a uniform grid to generate the samples

$$d_{k,l} = \frac{1}{T^2} \iint_{\Omega} I(x,y) \phi\left(\frac{x}{T} - k, \frac{y}{T} - l\right) dx dy.$$

In a noisy setup, the noise vector will be added to the measurements after spacial sampling. The sampling kernel $\phi(x,y)$ is determined by the physics of the sampling device but in most cases it can be considered as a separable kernel $\phi(x)\phi(y)$. In the first part of this chapter, we consider separable kernels that can reproduce polynomials up to some degree. $\phi(x)$ is a polynomial reproducing kernel of degree \mathcal{N} if there exist coefficients $c_k^{(i)}$ such that [52]

$$\sum_{k \in \mathbb{Z}} c_k^{(i)} \phi(x - k) = x^i, \quad i = 0, \dots, \mathcal{N}.$$

B-splines are well-known examples of polynomial reproducing kernels [113]. A zero order B-spline $\beta^{(0)}(x)$ is defined as

$$\beta^{(0)}(x) = \begin{cases} 1, & -0.5 < x < 0.5 \\ 0.5, & |x| = 0.5 \\ 0, & \text{otherwise.} \end{cases}$$

A B-spline of order m is obtained by convolving $m + 1$ kernel $\beta^{(0)}(x)$

$$\beta^{(m)}(x) = \underbrace{\beta^{(0)} * \beta^{(0)} * \dots * \beta^{(0)}}_{m+1 \text{ times}}.$$

The first few B-spline kernels are displayed in Figure 3.3. The B-spline kernel $\beta^{(m)}$ can reproduce monomials up to degree m and the corresponding coefficients are obtained as

$$c_k^{(i)} = \langle x^i, \tilde{\beta}^{(m)}(x - k) \rangle,$$

where $\tilde{\beta}^{(m)}(\cdot)$ is the dual of $\beta^{(m)}(\cdot)$ [113].

In any image sampling scenario, the question is whether and how we can reconstruct the original image $I(x,y)$ from a finite number of samples $d_{k,l}$ (Figure 3.4). In the next sections, we present a technique for the reconstruction of the boundary curve \mathcal{C} and hence the algebraic shape $I(x,y)$ from adequate noiseless or noisy samples $d_{k,l}$.

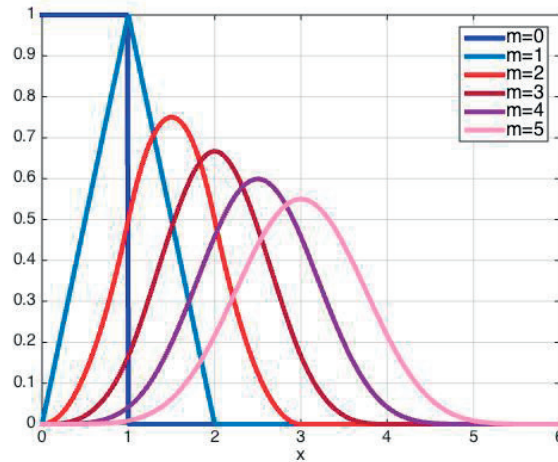


Figure 3.3: B-spline kernels of order 0 to 5.

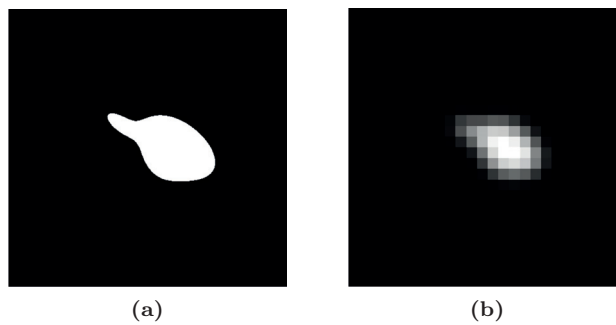


Figure 3.4: (a) An algebraic shape. (b) Samples generated with the tensor product of B-spline kernels of order 6.

3.3 Reconstruction from Moments

For an exact reconstruction of an algebraic shape image, we should estimate its boundary –the algebraic curve \mathcal{C} – from the samples. In the sequel, we first derive some annihilating equations for the curve parameters based on the shape moments. Then, we use the existing FRI techniques [52] to calculate shape moments from the samples. The overall procedure is summarized in Algorithm 3.1.

Algorithm 3.1 Algebraic shape reconstruction from noiseless samples

Input: noiseless samples $d_{k,l}$, degree n of the algebraic shape, polynomial reproducing coefficients $c_k^{(i)}$ of the sampling kernel.

Output: boundary curve \mathcal{C} .

- 1: Calculate shape moments $M_{i,j}$ from samples for any $0 \leq i, j \leq 3n/2$, according to the equation (3.11).
 - 2: Form the annihilation equations (3.8) and (3.9) for any $0 \leq r, s \leq n/2$ and put them into a linear system of the form $\mathbf{M}\mathbf{a} = \mathbf{0}$.
 - 3: Solve $\mathbf{M}\mathbf{a} = \mathbf{0}$ for the polynomial coefficients \mathbf{a} with the constraint $\mathbf{a}[0] = a_{0,0} = 1$.
 - 4: Form the polynomial $p(x, y)$ from the coefficients in \mathbf{a} according to (3.1).
 - 5: Set \mathcal{C} equal to the zero level set of $p(x, y)$ inside Ω . $=0$
-

3.3.1 Annihilation equations

Consider a closed algebraic curve \mathcal{C} inside the domain Ω and the corresponding shape image I . We can rewrite I in equation (3.2) as

$$I(x, y) = \begin{cases} 1, & (x, y) \in \overline{Int(\mathcal{C})} \\ 0, & \text{otherwise,} \end{cases}$$

where $\overline{Int(\mathcal{C})}$ denotes the closure of the interior of \mathcal{C} . This equation explains that the partial derivatives $\frac{\partial I(x, y)}{\partial x}$ and $\frac{\partial I(x, y)}{\partial y}$ vanish everywhere in Ω except possibly on \mathcal{C} , where they behave like the Dirac δ function. So, similar to the equation $x\delta(x) = 0$, we conclude that

$$p(x, y) \frac{\partial I(x, y)}{\partial x} \equiv 0, \quad (3.3)$$

$$p(x, y) \frac{\partial I(x, y)}{\partial y} \equiv 0, \quad (3.4)$$

inside Ω .

We can multiply the above equations with $x^r y^s$ for any $r, s \in \mathbb{Z}^{\geq 0}$ and integrate over the domain to obtain the equations

$$\iint_{\Omega} x^r y^s p(x, y) \frac{\partial I(x, y)}{\partial x} dx dy = 0, \quad (3.5)$$

$$\iint_{\Omega} x^r y^s p(x, y) \frac{\partial I(x, y)}{\partial y} dx dy = 0. \quad (3.6)$$

By substituting $p(x, y)$ from equation (3.1) in (3.5) and using integration by parts, we get

$$\sum_{\substack{0 \leq i, j \\ i+j \leq n}} (i+r) a_{i,j} \iint_{\Omega} x^{(i+r-1)} y^{(j+s)} I(x, y) dx dy = 0. \quad (3.7)$$

In the derivation of (3.7), we also used the fact that \mathcal{C} is a closed curve inside Ω and hence, I is zero at the domain borders.

The integrals in equation (3.7) represent 2D moments of the image I

$$M_{i,j} = \iint_{\Omega} x^i y^j I(x, y) dx dy.$$

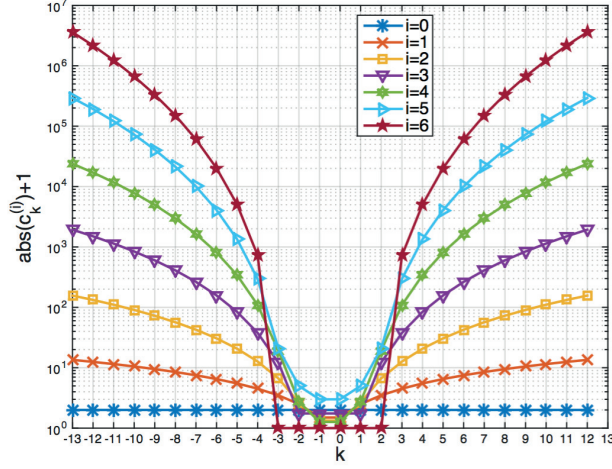


Figure 3.5: The exponential growth rate of polynomial reproducing coefficients of the B-spline kernel $\beta^{(6)}(x)$.

Hence, we can rewrite equation (3.7) as

$$\sum_{0 \leq i, j, i+j \leq n} (i+r) M_{i+r-1, j+s} a_{i, j} = 0. \quad (3.8)$$

We can similarly modify equation (3.6) to derive the additional equation

$$\sum_{0 \leq i, j, i+j \leq n} (j+s) M_{i+r, j+s-1} a_{i, j} = 0. \quad (3.9)$$

For any pair of (r, s) , formula (3.8) and (3.9) give us two linear annihilation equations for the $\binom{n+1}{2}$ coefficients $a_{i, j}$, in terms of the image moments. We get enough equations to build a linear system of the form

$$\mathbf{M}\mathbf{a} = \mathbf{0} \quad (3.10)$$

and derive the curve parameters, if we consider all pairs (r, s) , $0 \leq r, s \leq n/2$. This implies that we require all image moments of degree up to $3n/2$, i.e., $M_{i, j}$, $0 \leq i, j \leq 3n/2$.

To avoid the trivial solution $\mathbf{a} = \mathbf{0}$, we set the term corresponding to $x^0 y^0$ to 1. We recall that a scaling of the polynomial coefficients does not change its level sets. In Theorem 3.2, we prove that the zero level set of the polynomial $q(x, y)$ formed by any solution of (3.10) contains \mathcal{C} . This specifically means that although the system of equations in (3.10) might have a null space with dimension larger than 1, any vector \mathbf{a} in this null space generates a polynomial that vanishes on the boundary of I . Hence, we can recover the boundary curve \mathcal{C} and the algebraic shape I from any solution of (3.10).

Finally, it remains to retrieve moments from the samples. Suppose that the kernel $\phi(x)$ can reproduce polynomials up to degree $3n/2$, with the corresponding coefficients $c_k^{(i)}$, $i = 0, \dots, 3n/2$.

The 2D moments of the image can be calculated as

$$\begin{aligned}
M_{i,j} &= \iint_{\Omega} x^i y^j I(x, y) \, dx \, dy \\
&= \iint_{\Omega} \sum_{k \in \mathbb{Z}} c_k^{(i)} \phi(x - k) \sum_{l \in \mathbb{Z}} c_l^{(j)} \phi(y - l) I(x, y) \, dx \, dy \\
&= \sum_{k \in \mathbb{Z}} \sum_{l \in \mathbb{Z}} c_k^{(i)} c_l^{(j)} \iint_{\Omega} \phi(x - k) \phi(y - l) I(x, y) \, dx \, dy \\
&= \sum_{k \in \mathbb{Z}} \sum_{l \in \mathbb{Z}} c_k^{(i)} c_l^{(j)} d_{k,l} = \sum_{k \in \mathcal{K}} \sum_{l \in \mathcal{L}} c_k^{(i)} c_l^{(j)} d_{k,l}, \tag{3.11}
\end{aligned}$$

where \mathcal{K} and \mathcal{L} indicate the set of indices k and l such that $\phi(x - k)\phi(y - l)$ is nonzero over Ω .

3.3.2 Stability

Algorithm 3.1 restores the exact algebraic curve when it has access to the noiseless samples. But it breaks down in the presence of noise. The reason is that the polynomial reproducing coefficients $c_k^{(i)}$ have the same growth rate as the polynomials, i.e., they grow like $|k|^i$. (To illustrate this, we show the polynomial reproducing coefficients $c_k^{(i)}$ of a 1D 6th order B-spline kernel for $i = 0, \dots, 6$ in Figure 3.5.) This specially implies that in equation (3.11), the weight of samples that are away from the image center are considerably larger than the weight of the central samples. But for images in our model, samples at the image borders mostly contain noise. This transfers an amplified noise to the moments and results in severely degraded moments SNR. The noise boosting effect becomes more critical as the order of moments grow. This makes Algorithm 3.1 unstable even at a sample SNR as high as 100 dB.

We recall that in the related works of [12] and [41], only the first order moments are required as they focus on first degree polynomials (step edges). Hence, the aforementioned noise boosting effect is not an issue.

In the next section, we introduce some generalized moments that have slower growth rates and discard the noise at the image borders. Above all, they are still reproducible from the samples generated with a wider range of sampling kernels.

3.4 Stable Recovery

The sampling scheme of Section 3.3 has some limitations: (i) the reconstruction algorithm succeeds only in the absence of noise; (ii) the acceptable sampling kernels $\phi(\cdot)$ are limited to the ones that exactly reproduce polynomials; and (iii) the algebraic shapes should have closed boundary curves. In this section, we modify Algorithm 3.1 in three steps to resolve these limitations:

First and foremost, we introduce a fast decaying (or even compact-support) function $g(x, y)$ in the integrands of equations (3.5) and (3.6) to reduce the growth rate of polynomials, especially at the borders of Ω . This translates into the annihilation equations as replacing moments with some generalized moments. We prove in Theorem 3.2 that under noiseless samples, the resulting annihilation equations restore the exact boundary curve of any algebraic shape. Our proof is general and includes the case $g(x, y) = 1$ which leads to conventional moments. Next, we

describe the requirements for $g(x, y)$ to ensure stable generalized moments and we propose an optimization procedure for finding the best candidate g that pairs with a given sampling kernel. Interestingly, the inclusion of g allows for extension of the image model to algebraic shapes with open boundaries.

For our second step, we note that the image moments do not take full advantage of the available samples. For instance, the samples allow for prediction of the sign of the implicit polynomial on a subset of the sampling grid points and this prediction is fairly robust against noise. To further improve the reconstruction, we enforce sign consistency of the polynomial with the prediction of the available samples.

In our last step, we encourage full measurement consistency (not just sign) through bounded changes in the coefficients of the implicit polynomial.

3.4.1 Annihilation equations with generalized moments

We developed the annihilation equations of Section 3.3.1 by multiplying equations (3.3) and (3.4) with $x^r y^s$. This caused the image moments to appear in the equations. To control the growth rate of the polynomials and hence the moments, we replace $x^r y^s$ with $g(x, y)x^r y^s$ for an appropriate function g .

Definition 3.1

For any bivariate function $g(.,.)$ and integers $i, j \geq 0$, we call

$$M_{i,j}^{g(x,y)} = \int_{-\infty}^{+\infty} \int_{-\infty}^{+\infty} x^i y^j g(x, y) I(x, y) dx dy.$$

a 2D generalized moment of I , associated with g .

Having separable sampling kernels, we also take $g(x, y)$ to be separable of the form $g(x, y) = g(x)g(y)$. Though, the results can be similarly extended to the non-separable kernels. In the following, we derive the new annihilation equations and discuss the requirements on g afterwards.

We multiply equations (3.3) and (3.4) with $g(x)g(y)x^r y^s$ and repeat similar steps as in Section 3.3.1 to obtain

$$\sum_{\substack{0 \leq i,j \\ i+j \leq n}} a_{i,j} \iint_{\Omega} \frac{\partial x^{r+i} g(x)}{\partial x} y^{s+j} g(y) I(x, y) dx dy = 0, \quad (3.12)$$

$$\sum_{\substack{0 \leq i,j \\ i+j \leq n}} a_{i,j} \iint_{\Omega} x^{r+i} g(x) \frac{\partial y^{s+j} g(y)}{\partial y} I(x, y) dx dy = 0. \quad (3.13)$$

In Section 3.3, we had to assume that I is zero at the borders of the image plane in order to use integration by parts. Here, we assume that $g(\cdot)$ is either zero outside $(-L, L)$ or decays so fast that the integral outside of this interval becomes negligible. This allows I to take non-zero values at the borders of Ω ; consequently, I can represent an unbounded shape.

We can further simplify equations (3.12) and (3.13) and substitute the integrals with generalized moments to get the new annihilation equations

$$\sum_{\substack{0 \leq i, j \\ i+j \leq n}} \left((i+r)M_{i+r-1, j+s}^{g(x)g(y)} + M_{i+r, j+s}^{\dot{g}(x)g(y)} \right) a_{i,j} = 0, \quad (3.14)$$

$$\sum_{\substack{0 \leq i, j \\ i+j \leq n}} \left((j+s)M_{i+r, j+s-1}^{g(x)g(y)} + M_{i+r, j+s}^{g(x)\dot{g}(y)} \right) a_{i,j} = 0, \quad (3.15)$$

where \dot{g} stands for the derivative of g . The above equations are valid for any $0 \leq r, s$. Note that $g = 1$ restores the annihilation equations (3.8) and (3.9) when I represents a closed shape. In Theorem 3.2, we state a unified result for recovery of algebraic shapes without singular edges¹ either from conventional annihilation equations or the generalizations in (3.14) and (3.15). The proof of this theorem is provided in the appendix².

Theorem 3.2

Let I denote an algebraic shape of degree n defined on Ω without singular edges. Also, let $M_{i,j}^{g(x)g(y)}$, $M_{i,j}^{g(x)\dot{g}(y)}$ and $M_{i,j}^{\dot{g}(x)g(y)}$ denote the generalized moments of I (Definition 3.1) corresponding to a function $g(\cdot)$ for which $I(x, y)g(x)g(y)$ vanishes outside $\text{Int}(\Omega)$ and $g(x)g(y)$ remains strictly positive inside Ω . If $\tilde{\mathbf{a}} = [\tilde{a}_{i,j}]_{i+j \leq n} \neq \mathbf{0}$ satisfies the annihilation equations (3.14) and (3.15) for all $0 \leq r, s$, $r + s \leq 2n - 1$, then, the zero level set of the polynomial

$$\tilde{p}(x, y) = \sum_{0 \leq i, j, i+j \leq n} \tilde{a}_{i,j} x^i y^j$$

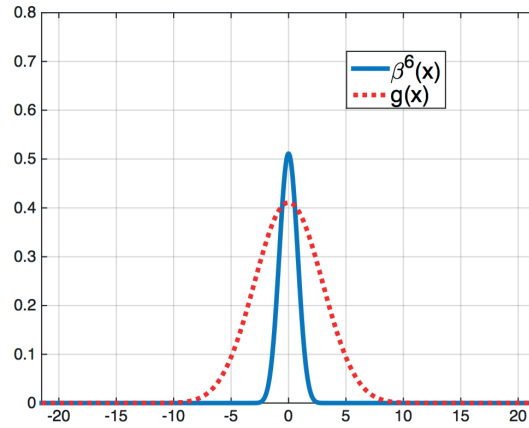
contains the boundaries (edges) of I .

Remark 3.2

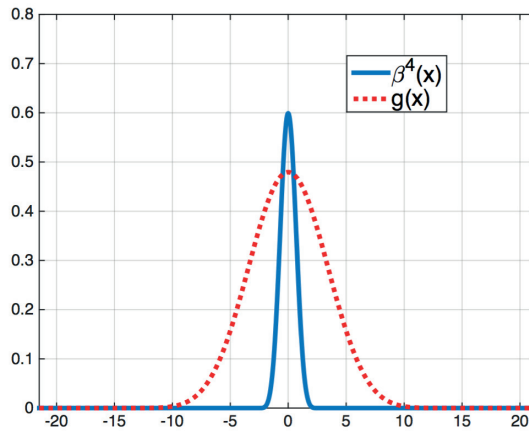
Unique recovery of $p(x, y)$ is not generally possible. Obviously, the zero level sets of $p(x, y)$ and $2p(x, y)$ are the same, leading to the same algebraic shapes. However, there are less obvious examples that prevent unique recovery: the zero level sets of both $(x^2 + y^2 - 1)(x^2 - 2x + 2)$ and $(x^2 + y^2 - 1)(x^2 + y^2 + 2xy + 1)$ coincide with the unit circle, while the two bivariate polynomials have the same degree. The important point in Theorem 3.2 is that the curve \mathcal{C} is uniquely determined, but possibly with a different implicit polynomial.

1. We call an edge singular if the image level does not change on either of its sides; for instance the image associated with $\chi_{\{(x-y)^2 \leq 0\}}$ has a singular edge at points with equal coordinates.

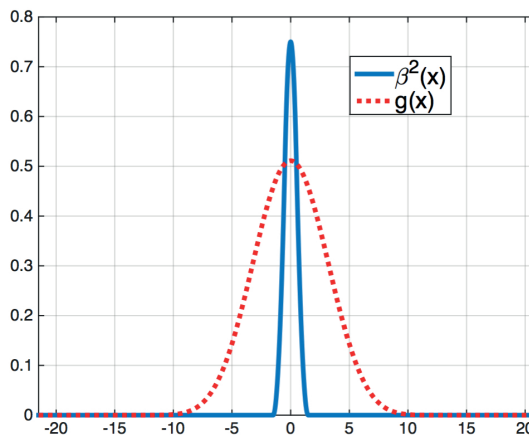
2. Shortly after arxivng the results of this chapter, we were informed about the recent work of [76] that studies the problem of reconstructing algebraic shapes from their conventional 2D moments, which has some parts in common with the content of this chapter. Specifically, it proposes the same set of annihilation equations for recovering the polynomial coefficients and contains a result similar to Theorem 3.2, but with a substantially different proof technique.



(a)



(b)



(c)

Figure 3.6: B-spline kernels and their associated g 's for reproducing stable generalized moments of order less than or equal to 6. The indices (\mathcal{I}) of the contributing kernels in equations (3.16) and (3.17) and the minimum number of required samples (m) are (a) $\mathcal{I} = \{-13, -12, \dots, 13\}$ and $m = 27$, (b) $\mathcal{I} = \{-14, -13, \dots, 14\}$ and $m = 29$, (c) $\mathcal{I} = \{-20, -19, \dots, 20\}$ and $m = 41$, respectively.

Remark 3.3

Theorem 3.2 requires that the coefficients of $\tilde{p}(x, y)$ satisfy the annihilation equations (3.14) and (3.15) for every $0 \leq r + s \leq 2n - 1$. This generates an over-determined system of the form $\mathbf{M}\mathbf{a} = \mathbf{0}$ with about 8 times more rows than columns. In our experiments, we have confirmed successful recovery of algebraic curves from the annihilation equations corresponding to $0 \leq r, s \leq n/2$ (yielding an almost balanced system). Our proof technique, however, falls short of this stronger result.

Optimal generalized moments

The primary reason of introducing $g(x)g(y)$ to the equations is to control the growth rate of the monomials $x^r y^s$, especially at the image borders. Ideally, the $g(\cdot)$ function in (3.12) and (3.13) should be set such that g and \dot{g} both vanish outside $(-L, L)$. The faster they decay near the borders of $[-L, L]$, the more stable will be the annihilation equations (3.14) and (3.15). However, the bottleneck in setting $g(\cdot)$ is the reproduction of moments from the samples. That is the functions $x^i g(x)$ and $x^i \dot{g}(x)$, $i = 0, \dots, \frac{3n}{2}$ should be reproducible by the sampling kernel $\phi(x)$, i.e., we need coefficients $\{c_k^{(i)}\}$ and $\{\tilde{c}_k^{(i)}\}$ that satisfy

$$\sum_{k \in \mathcal{I}} c_k^{(i)} \phi(x - k) \approx x^i g(x), \quad (3.16)$$

$$\sum_{k \in \mathcal{I}} \tilde{c}_k^{(i)} \phi(x - k) \approx x^i \dot{g}(x). \quad (3.17)$$

Here, \mathcal{I} represents k values for which $\phi(x - k)$ has an effective support in $[-L, L]$; this ensures that $g(x)$ and $\dot{g}(x)$ vanish outside $[-L, L]$.

For recovering an algebraic curve (domain) from samples using the generalized moment technique, we need to linearly combine the samples in correspondence to the coefficients $\{c_k^{(i)}\}$ and $\{\tilde{c}_k^{(i)}\}$. In other words, we never require the function g explicitly in practice. Consequently, instead of looking for the best g function, we can search for coefficients $\{c_k^{(i)}\}$ and $\{\tilde{c}_k^{(i)}\}$ such that

$$\begin{aligned} \sum_{k \in \mathcal{I}} c_k^{(i)} \phi(x - k) &\approx x \sum_{k \in \mathcal{I}} c_k^{(i-1)} \phi(x - k), \quad i \geq 1, \\ \sum_{k \in \mathcal{I}} \tilde{c}_k^{(i)} \phi(x - k) &\approx x \sum_{k \in \mathcal{I}} \tilde{c}_k^{(i-1)} \phi(x - k), \quad i \geq 1, \\ \frac{d}{dx} \sum_{k \in \mathcal{I}} c_k^{(i)} \phi(x - k) &\approx \sum_{k \in \mathcal{I}} (i c_k^{(i-1)} + \tilde{c}_k^{(i)}) \phi(x - k). \end{aligned}$$

To find such coefficients, we introduce the following objective function

$$\begin{aligned} \mathcal{G}(\{c_k^{(i)}\}, \{\tilde{c}_k^{(i)}\}) = & \\ & \sum_{i=1}^{3n/2} \left\| \sum_{k \in \mathcal{I}} (c_k^{(i)} - x c_k^{(i-1)}) \phi(x-k) \right\|^2 \\ & + \sum_{i=1}^{3n/2} \left\| \sum_{k \in \mathcal{I}} (\tilde{c}_k^{(i)} - x \tilde{c}_k^{(i-1)}) \phi(x-k) \right\|^2 \\ & + \sum_{i=0}^{3n/2} \left\| \sum_{k \in \mathcal{I}} c_k^{(i)} \phi(x-k) - \sum_{k \in \mathcal{I}} (i c_k^{(i-1)} + \tilde{c}_k^{(i)}) \phi(x-k) \right\|^2. \end{aligned}$$

Next, we solve the quadratic program

$$\begin{aligned} \min_{c_k^{(i)}, \tilde{c}_k^{(i)}} \mathcal{G}(\{c_k^{(i)}\}, \{\tilde{c}_k^{(i)}\}) & \quad (3.18) \\ \text{s.t.} \quad \begin{cases} \sum_{k \in \mathcal{I}} c_k^{(0)} \phi(x-k) \geq 0, \\ c_0^{(0)} = 1. \end{cases} \end{aligned}$$

The equality constraint in the above minimization is to avoid the trivial zero solution and the inequalities guarantee that g is non-negative. Although solving a quadratic program is computationally manageable, we have frequently observed that (3.18) is ill-conditioned³ in the sense that iterative methods are very slow in achieving the global solution, and usually terminate much earlier than desired. This shortcoming could be improved by using a sufficiently good initialization. Furthermore, any set of coefficients which result in a small cost according to the objective function could be used.

We recall that an implicit parameter in this problem is the size of the index set \mathcal{I} . This parameter also affects the modeling of $\Omega = [-L, L]^2$ and the minimum required sampling density for this sampling kernel. In fact, by increasing the index set \mathcal{I} the global cost in (3.18) can only reduce. Thus, the larger the \mathcal{I} , the lower the cost. However, larger \mathcal{I} translates into more image samples, and consequently more complexity.

For the B-spline kernels, we found surprisingly good candidates g that make the objective function almost zero. Figure 3.6 shows the kernels $\beta^{(6)}(x)$, $\beta^{(4)}(x)$, $\beta^{(2)}(x)$ and their associated g 's that reproduce stable generalized moments of order 6 or less. This implies that we can form the annihilation equations and recover algebraic shapes of degree 4 even when the sampling kernel is the tensor product of 2nd order B-splines. The cost is a larger number of required samples.

Our final remark concerns using an asymmetric function $g(x, y)$ in the form of $f(x)h(y)$ in the annihilation equations, when $\phi(x)$ fails to generate both set of functions $x^i g(x)$ and $x^i \dot{g}(x)$ for a single $g(x)$. In this case, we can multiply equations (3.3) and (3.4) with $f(x)h(y)x^r y^s$ and

3. Essentially, the source is the same as the one causing instability in Algorithm 3.1 except there is no noise here: the error terms corresponding to different i 's in the objective function grow polynomially and this makes the problem ill-conditioned.

$h(x)f(y)x^r y^s$, respectively and follow the same steps to obtain

$$\sum_{\substack{0 \leq i, j \\ i+j \leq n}} a_{i,j} \iint_{\Omega} \frac{\partial x^{r+i} f(x)}{\partial x} y^{s+j} h(y) I(x, y) dx dy = 0,$$

$$\sum_{\substack{0 \leq i, j \\ i+j \leq n}} a_{i,j} \iint_{\Omega} x^{r+i} h(x) \frac{\partial y^{s+j} f(y)}{\partial y} I(x, y) dx dy = 0.$$

We can calculate the integrals from the samples and obtain the polynomial coefficients $a_{i,j}$ by solving the above equations, if we find two positive and compact-support functions f and h such that

$$\sum_{k \in \mathcal{I}} c_k^{(i)} \phi(x - k) \approx x^i h(x),$$

$$\sum_{k \in \mathcal{I}} \tilde{c}_k^{(i)} \phi(x - k) \approx \frac{d}{dx} (x^i f(x)), \quad i = 0, \dots, 3n/2.$$

For finding $c_k^{(i)}$ and $\tilde{c}_k^{(i)}$, (3.18) needs to be divided into two quadratic programs that accommodate $c_k^{(i)}$ and $\tilde{c}_k^{(i)}$ separately, with the cost functions

$$\mathcal{H}(c_k^{(i)}) = \sum_{i=1}^{3n/2} \left\| \sum_{k \in \mathcal{I}} (c_k^{(i)} - x c_k^{(i-1)}) \phi(x - k) \right\|^2$$

and

$$\mathcal{F}(\tilde{c}_k^{(i)}) = \sum_{i=1}^{3n/2} \left\| \sum_{k \in \mathcal{I}} (\tilde{c}_k^{(i)} - x \tilde{c}_k^{(i-1)}) \bar{\phi}(x - k) \right\|^2,$$

where $\bar{\phi}(x) = \int_0^x \phi(\tau) d\tau$.

Patch-based recovery

Equations (3.16) and (3.17) show that $g(x)$ and consequently $g(x)g(y)$ have compact support. This indicates that the generalized moments are computed from a finite window of the image samples –namely, of size $m \times m$, where m amounts to the number of contributing kernels in \mathcal{I} . Having access to more samples, we can slide a $m \times m$ window over the image samples, calculate 2D moments and form the annihilation equations for each window. This results in a linear system with more equations and improves the noise stability of the reconstruction.

There is only one issue requiring further attention: in the annihilation equations of each window, the coordinates origin is taken at the window's center (Figure 3.7). This means that the variables of each set of annihilation equations are the coefficients of the polynomial in those coordinates. Hence, we should compensate for the shifts in the coordinates before concatenating the equations of different windows. For this purpose, we choose the reference coordinates as the symmetry axes of the image plane. When the coordinates are shifted by (x_0, y_0) , the polynomial

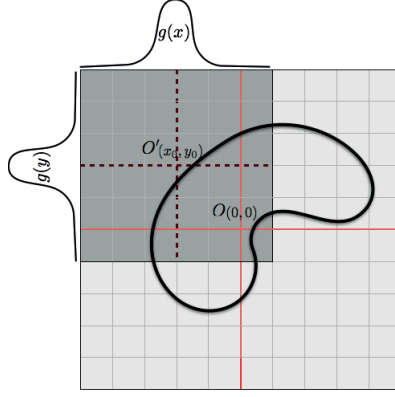


Figure 3.7: A compact support function $g(x, y)$ facilitates the calculation of 2D generalized moments and the annihilation equations for different windows of the image samples. However, the coordinate shifts between different windows should be compensated before concatenating the equations in one system.

$p(x, y) = \sum_{0 \leq i, j, i+j \leq n} a_{i,j} x^i y^j$ in the original system shall be mapped to the polynomial

$$\begin{aligned} \tilde{p}(x, y) &= p(x + x_0, y + y_0) \\ &= \sum_{0 \leq i, j, i+j \leq n} a_{i,j} (x + x_0)^i (y + y_0)^j \\ &= \sum_{0 \leq i, j, i+j \leq n} a_{i,j} \sum_{k=0}^i \binom{i}{k} x_0^{i-k} \sum_{l=0}^j \binom{j}{l} y_0^{j-l} x^k y^l. \end{aligned}$$

This reveals the mapping between the coefficients of $\tilde{p}(x, y)$, denoted by $b_{k,l}$, and $a_{i,j}$'s as

$$b_{k,l} = \sum_{\substack{k \leq i, l \leq j \\ i+j \leq n}} \binom{i}{k} \binom{j}{l} x_0^{i-k} y_0^{j-l} a_{i,j},$$

for any $0 \leq k, l, k + l \leq n$. We can represent the above relations for all polynomial coefficients simultaneously as

$$\mathbf{b} = \mathbf{B}^{(x_0, y_0)} \mathbf{a}, \quad (3.19)$$

where $\mathbf{B}^{(x_0, y_0)}$ is an upper triangular square matrix with diagonal entries equal to 1. This allows us to relate the annihilation equations of a window centered at (x_0, y_0) to the polynomial coefficients \mathbf{a} in the reference coordinate system through the equation

$$\mathbf{M}^{(x_0, y_0)} \mathbf{b} = \mathbf{M}^{(x_0, y_0)} \mathbf{B}^{(x_0, y_0)} \mathbf{a} = \mathbf{0}.$$

In a nutshell, we should multiply the annihilation equations of different windows with the corresponding matrix $\mathbf{B}^{(x_0, y_0)}$ in equation (3.19) before concatenating them in a bigger system.

3.4.2 Constraints on the sign of the polynomial

So far, we have built a system of equations in terms of the image parameters that is stable at numerical precision. In the presence of noise, the annihilation equations are only approximately singular. In this case, as a common practice, we consider the solution of the least squares minimization problem

$$\begin{aligned} \min_{\mathbf{a}} \|\mathbf{M}\mathbf{a}\|_2^2 \\ \text{s.t. } \mathbf{a}[0] = a_{0,0} = 1. \end{aligned} \quad (3.20)$$

The least squares denoising works well at low noise levels, especially when \mathbf{M} is a tall matrix. Nevertheless, since algebraic curves are dense among continuous curves, distortion in the image moments (originated from moderate noise levels in the samples) can lead to substantially different solutions.

Recently, the Cadzow's denoising algorithm [22] has been used for denoising of the annihilation equations of 1D [15] and 2D [88] FRI signals. The common feature in these works that makes denoising successful is having annihilation equations with a Toeplitz structure. Our system of annihilation equations –although almost each element in \mathbf{M} has a few duplicates– is not Toeplitz and the Cadzow's denoising algorithm does not help⁴.

In our problem, the best reconstruction is an algebraic shape that is as consistent as possible with the image samples (i.e., up to the samples SNR). Theoretically, this can be achieved with a brute-force search over the space of image parameters. But this problem is nonconvex with many parameters and hence, computationally intractable. In the rest of this section, we exploit the local information provided by the samples to improve the reconstruction in the presence of noise.

Sample values represent the area of the intersection of the corresponding kernels with the interior of the shape in a weighted form. For example, $d_{k,l} = 1(0)$ indicates that $I(x, y) = 1(0)$ everywhere in the support of $\phi(x - k, y - l)$ ⁵. We further incorporate the samples in our reconstruction by interpreting them as the central points of the corresponding kernels lying inside or outside the shape. More precisely, if $d_{k,l}$ is above $1 - \epsilon$ for an $\epsilon < 0.5$, we assume its center to be inside the shape, i.e., $I(k, l) = 1$ or equivalently $p(k, l) \leq 0$. Also, we take $I(k, l) = 0$ or $p(k, l) > 0$, if $d_{k,l} < \epsilon$. Eventually, we constrain the solution of the least squares problem with the inferred signs:

$$\begin{aligned} \min_{\mathbf{a}} \|\mathbf{M}\mathbf{a}\|_2^2, \\ \text{s.t. } \mathbf{A}_{\text{in}}\mathbf{a} \leq \mathbf{0}, \\ \mathbf{A}_{\text{out}}\mathbf{a} < \mathbf{0}, \end{aligned} \quad (3.21)$$

where \mathbf{A}_{in} and \mathbf{A}_{out} encode respectively, the normal and sign-negated polynomial evaluation matrices at central locations of the sampling kernels; \mathbf{A}_{in} corresponds to locations with large sample values, while \mathbf{A}_{out} corresponds to locations with small sample values. The minimization problem (3.21) can be solved with quadratic programming algorithms.

4. In our implementation of Cadzow's algorithm, we observed that it converges to a rank deficient matrix with the expected structure which stays very close to the noisy matrix \mathbf{M} .

5. We assume that $T = 1$ and $\phi(x, y)$ has a unit integral.

3.4.3 Measurement consistency

At moderate noise levels (sample SNRs around 25 dBs), the recovered curves from (3.21) are close enough to the original boundaries to let us approximate the function mapping the polynomial coefficients to the image samples with a 1st order Taylor expansion around the correct coefficients. We exploit this assumption to improve the measurement consistency of the reconstruction.

Let \mathcal{D} denote the mapping from the polynomial coefficients into the samples of the algebraic shape. For instance, if \mathbf{a}^* stands for the polynomial coefficients associated with an algebraic curve, $\mathbf{d}^* = \mathcal{D}(\mathbf{a}^*)$ represents the vector of noiseless image samples via the sampling kernel.

For a given set of noisy samples $\widetilde{\mathbf{d}}^*$, let \mathbf{a}_{cur} be the solution to the sign consistency technique in (3.21), which corresponds to $\mathbf{d}_{\text{cur}} = \mathcal{D}(\mathbf{a}_{\text{cur}})$. For moderate to low noise levels, we know that \mathbf{a}_{cur} is a good approximation of \mathbf{a}^* . Thus, we use the linearization of \mathcal{D} around \mathbf{a}_{cur} (1st order Taylor expansion) to write that

$$\mathbf{d}^* \approx \mathbf{d}_{\text{cur}} + \left(\frac{\partial}{\partial \mathbf{a}} \mathcal{D}(\mathbf{a}_{\text{cur}}) \right) (\mathbf{a}^* - \mathbf{a}_{\text{cur}}),$$

where $\frac{\partial}{\partial \mathbf{a}} \mathcal{D}(\mathbf{a}_{\text{cur}})$ is a matrix that relates the small input variations in \mathcal{D} to its output around the point \mathbf{a}_{cur} . In practice, we find $\frac{\partial}{\partial \mathbf{a}} \mathcal{D}(\mathbf{a}_{\text{cur}})$ by numerically varying \mathbf{a}_{cur} in all directions and observing the corresponding \mathbf{d} 's. Finally, we improve our current estimate of \mathbf{a}^* by

$$\mathbf{a}_{\text{new}} = \mathbf{a}_{\text{cur}} + \left(\frac{\partial}{\partial \mathbf{a}} \mathcal{D}(\mathbf{a}_{\text{cur}}) \right)^{-1} (\widetilde{\mathbf{d}}^* - \mathbf{d}_{\text{cur}}).$$

In our algorithm, we apply few iterations of the above update rule. Each time we evaluate the associated \mathbf{d} vector and continue the iterations as long as this vector gets closer to $\widetilde{\mathbf{d}}^*$.

3.5 Experimental Results

We evaluate the performance of the proposed algorithm in different scenarios. We select bounded algebraic shapes for most of the experiments. For this purpose, we restrict the polynomial degree to even integers. But a randomly generated even degree polynomial very likely has unbounded level sets. A full characterization as well as a model for the generation of bivariate polynomials of degree 4 with bounded level sets was presented in [72] and [108]. We adopt this model to generate shapes for our experiments.

3.5.1 Noiseless recovery

In the first experiment, we study reconstruction of algebraic shapes from noiseless samples. Recalling the results of the last section, we expect to recover the exact image by solving the least squares problem (3.20). Figure 3.8 displays perfect reconstruction of an algebraic shape of degree 4, when the sampling kernel is the tensor product of the 6th order B-splines.

3.5.2 Recovery in the presence of noise

In this experiment, we aim at studying the effect of each step of the algorithm on the reconstructed image from noisy samples. For this purpose, we consider two distinct algebraic shapes

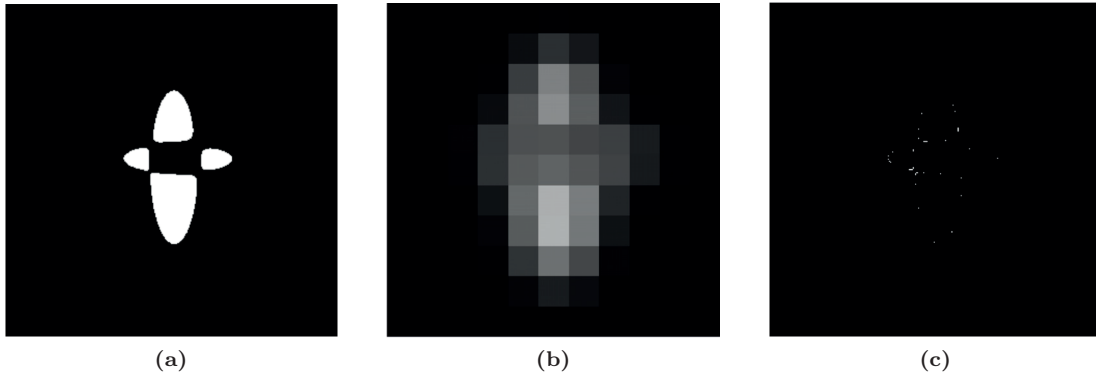


Figure 3.8: Exact reconstruction of algebraic shapes from noiseless samples. (a) An algebraic shape of degree 4. (b) Noiseless samples (size 11×11), when the sampling kernel is $\phi(x, y) = \beta^{(6)}(x)\beta^{(6)}(y)$. (c) Absolute difference between the original shape and the least squares solution.

of degree 4 with different levels of noise in their samples and we plot each stage of the reconstruction (Figures 3.9 and 3.10). The samples of both images are generated with the sampling kernel $\phi(x, y) = \beta^{(6)}(x)\beta^{(6)}(y)$ and the annihilation equations involve generalized moments corresponding to the function $g(x)$ in Figure 3.6(a). We see that although the least squares solution might be offbeat in presence of noise, the constraints on the sign of the polynomial substantially restrain the solution and lead to satisfactory reconstructions at moderate signal to noise ratios (SNRs).

3.5.3 Sampling kernel sensitivity

Earlier, we mentioned that a consequence of replacing conventional moments with generalized moments is relaxing the restrictive polynomial-reproducing requirement on the sampling kernel. Specifically, we worked out the reproducing coefficients for the B-spline kernels of order 2, 4, and 6 that generate stable generalized moments of order less than or equal to 6 (see Figure 3.6). This, for example, allows us to recover algebraic shapes of degree 4 from samples generated with the sampling kernel $\phi(x, y) = \beta^{(2)}(x)\beta^{(2)}(y)$. In this experiment, we study the sensitivity of the reconstruction to the choice of the kernel. Figure 3.11 displays the absolute difference between an image and its reconstructions from samples generated with different sampling kernels and similar signal-to-noise-ratios. The results are comparable irrespective of the choice of the sampling kernel (note the expected difference in the sample sizes that calls for different noise realizations for the three samples).

3.5.4 Unbounded algebraic shapes

Introducing generalized moments to the annihilation equations facilitated sampling and reconstruction of algebraic shapes with open boundaries (also referred as unbounded algebraic shapes). This additionally allows the reconstruction to enjoy oversampling by forming annihilation equations for each sample window, without caring about the image content of the window. Figure 3.12 shows the reconstruction of an unbounded image from its noisy samples, where the

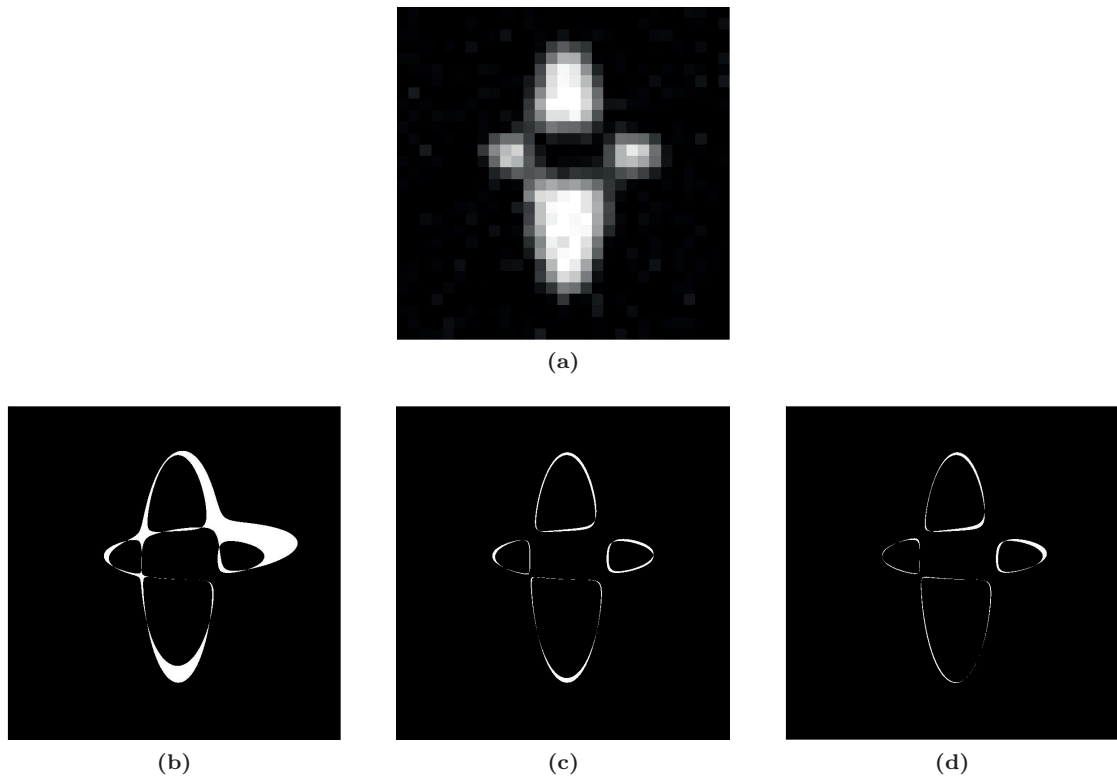


Figure 3.9: Reconstruction from noisy samples. (a) Noisy samples of the shape in Figure 3.8(a) with size 29×29 and $\text{SNR} = 17$ dB. (b) Absolute error of the least squares solution ($\text{PSNR} = 13.7$ dB). (c) Absolute error of the quadratic programming (equation (3.21)) reconstruction ($\text{PSNR} = 20.4$ dB). (d) Absolute error of the output of the consistency improvement algorithm ($\text{PSNR} = 21.3$ dB). SNR between the samples of the final reconstruction and the noisy samples (a) is 15.4 dB.

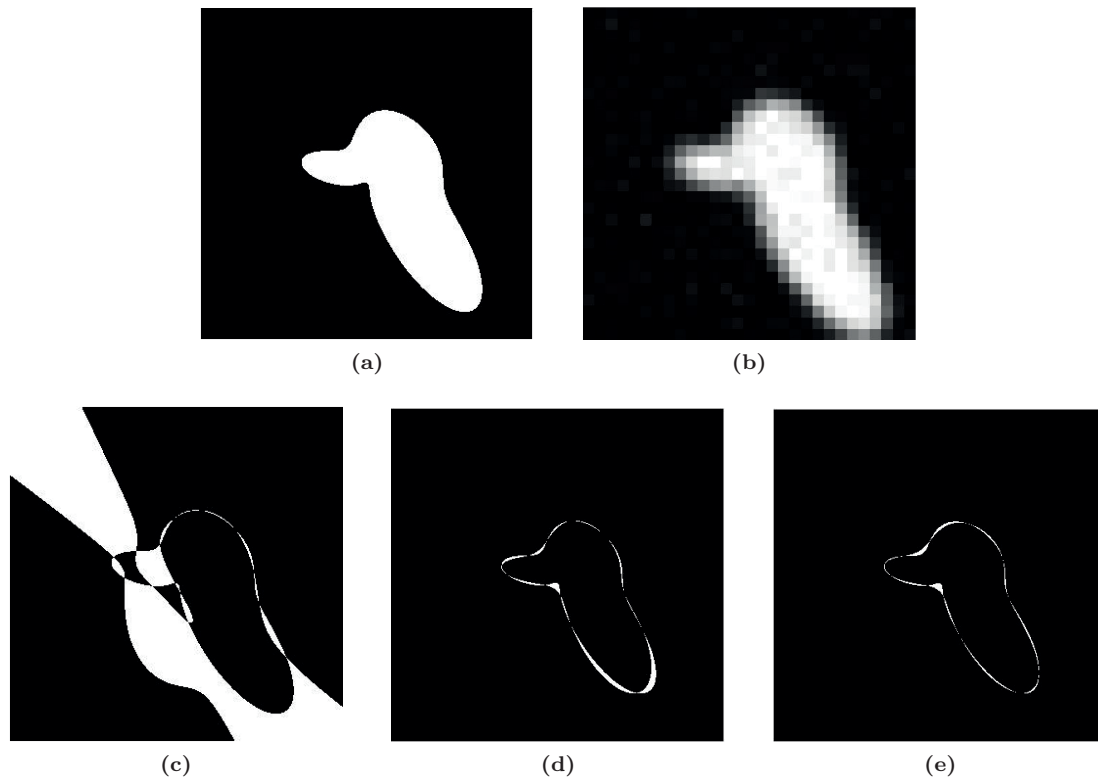


Figure 3.10: Reconstruction from noisy samples. (a) Original image. (b) Noisy samples of size 29×29 with $\text{SNR} = 22$ dB. (c) Absolute error of the least squares solution. (d) Absolute error of the quadratic programming solution ($\text{PSNR} = 21.0$ dB). (e) Absolute error of the output of the consistency improvement algorithm ($\text{PSNR} = 22.8$ dB). SNR between the samples of the final reconstruction and the noisy samples (b) is 20.9 dB.

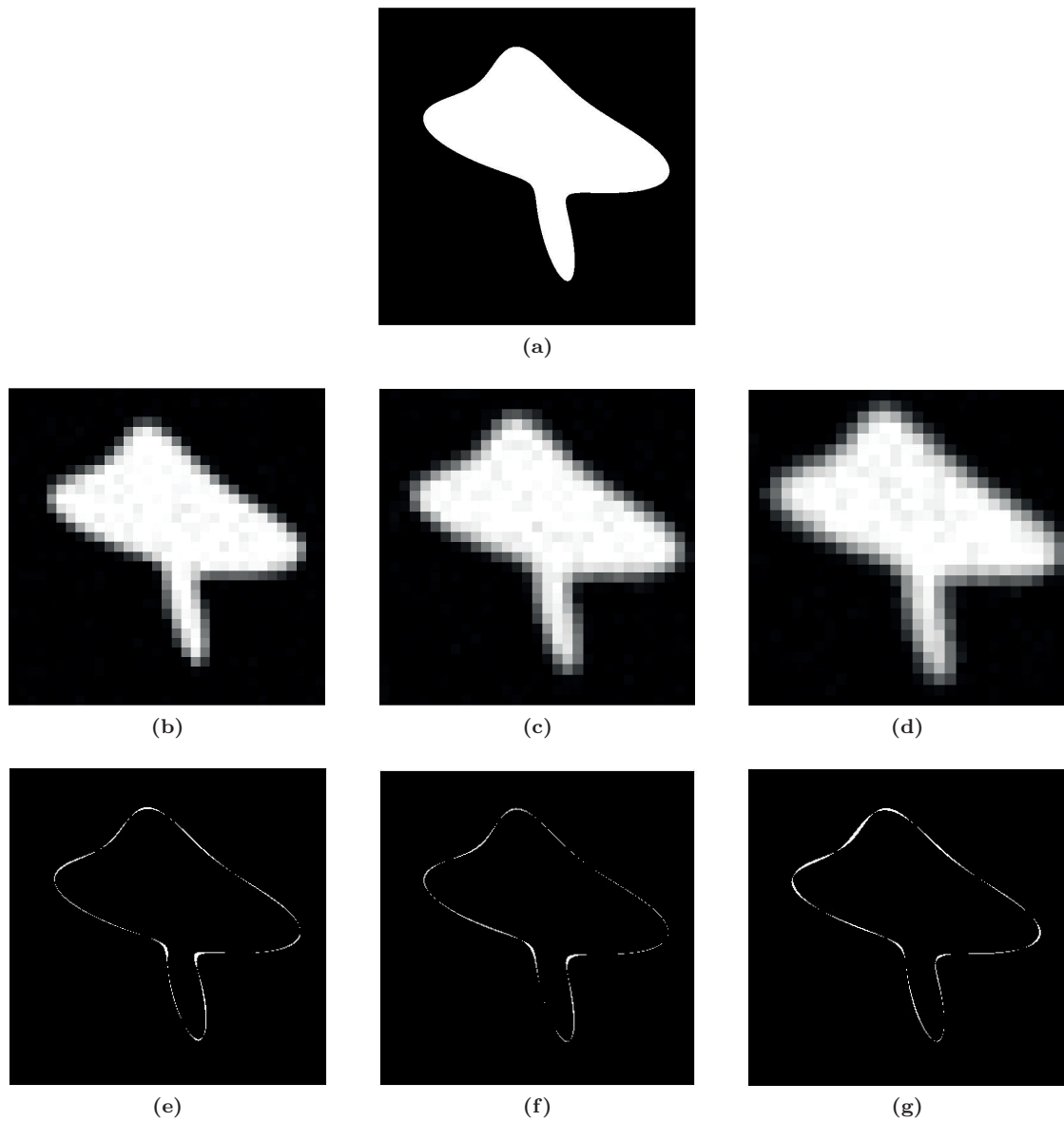


Figure 3.11: Sensitivity of the reconstruction to the choice of the sampling kernel. (a) Algebraic shape of degree 4. (b),(c),(d) Noisy samples ($\text{SNR} = 27$ dB) of size 33×33 , 31×31 and 29×29 , generated with B-spline kernels of degree 2, 4, and 6, respectively. (e),(f),(g) Absolute error of the reconstructions from samples in (b),(c) and (d) with reconstruction PSNRs 22.2 dB, 23.2 dB and 21.3 dB, respectively.

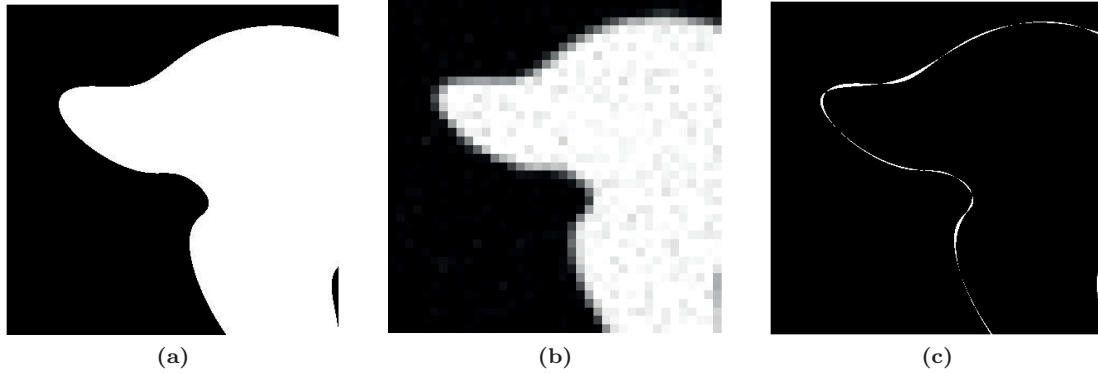


Figure 3.12: (a) Unbounded algebraic shape of degree 4. (b) Noisy samples of size 39×39 with $\text{SNR} = 25$ dB. (c) Absolute reconstruction error.

sampling kernel is the tensor product of 2nd order B-splines. The peak signal-to-noise ratio (PSNR) of the reconstructed image is 20.1 dB and SNR between its samples and the original noisy samples (sample consistency) is equal to 23.1 dB. These numbers clearly indicate the success of our proposed algorithm for reconstructing unbounded shapes.

3.5.5 Overfitting

In the last two experiments, we address uncertainties in the image model. First, we study the situation where we overestimate degree of an algebraic shape. Recalling Theorem 3.2 of the previous section, we expect the recovered polynomial from the annihilation equations to vanish on the boundaries of the original shape in the noiseless scenario. Figure 3.13 displays the results when we approximate an ellipse with algebraic shapes of degree 4 from its noiseless and noisy samples. Figures 3.13(c) and 3.13(f) show the least squares solutions for noiseless and noisy samples, respectively. Both figures indicate that the boundaries of the recovered images contain the boundary of the original ellipse. Equivalently, the recovered polynomials are factors of the original polynomial of degree 2. The extra factors are resolved in the next steps of the algorithm, resulting in exact reconstructions in both scenarios.

3.5.6 Algebraic shape approximation

Another type of uncertainty in the image model happens when the image boundary is not an algebraic curve. Regarding the descriptive power of algebraic curves, we still expect to find a good approximation of the image. To investigate this, we generated a shape with a Bézier curve boundary with four control points and generated its 15×15 -samples with 2nd order B-spline sampling kernels. Then, we obtained the approximate algebraic shape from the noiseless samples. The original image and the absolute error of its algebraic approximation are depicted in Figure 3.14. We observe that the reconstructed curve is a rather accurate descriptor of the original Bézier curve.

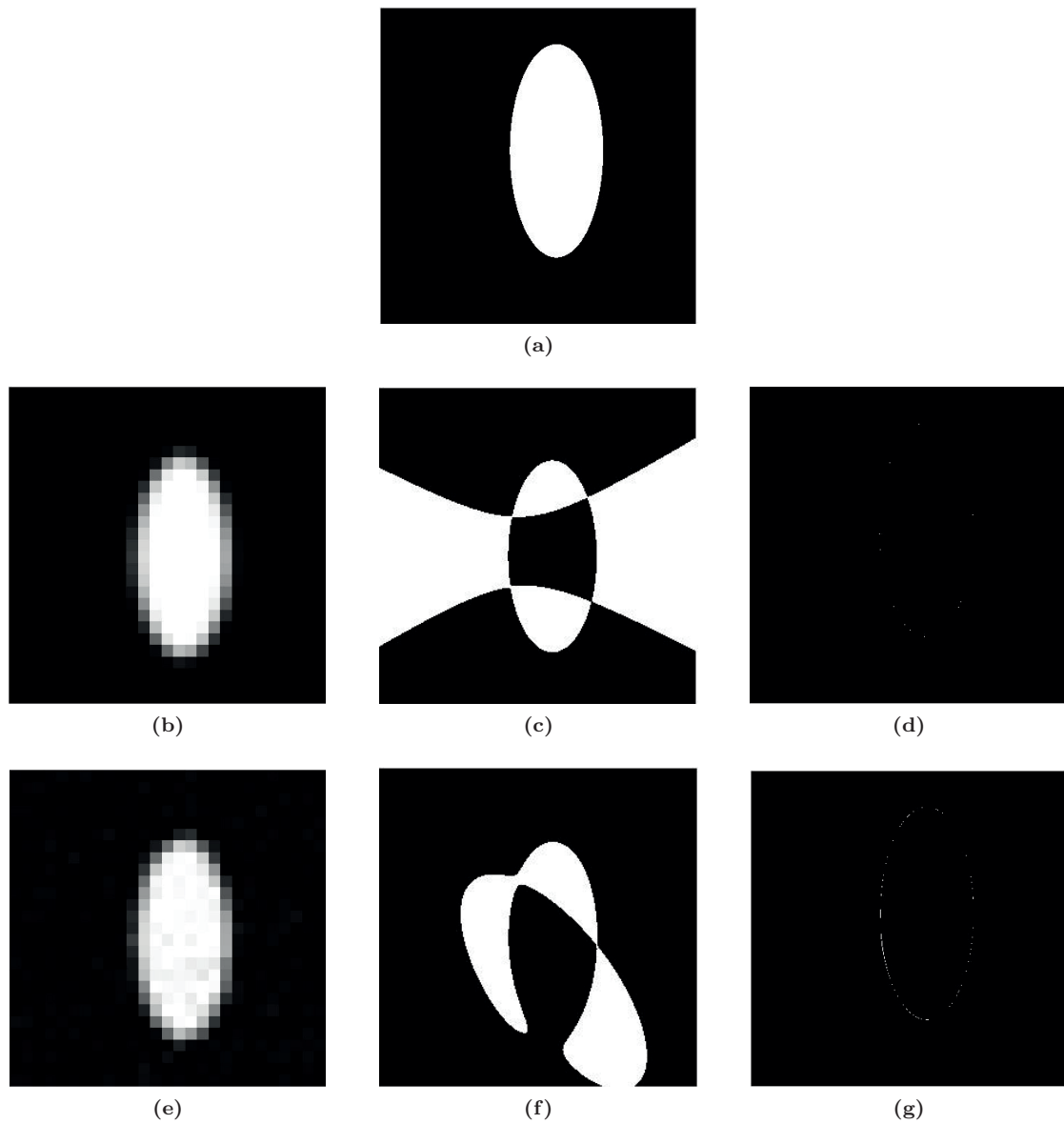


Figure 3.13: Approximation of an ellipse with algebraic shapes of degree 4. (a) Original ellipse. (b) Noiseless samples of size 27×27 , generated with B-splines of degree 2. (c) Least squares solution for noiseless samples. (d) Absolute error of the final reconstruction of the algorithm. (e) Noisy samples with $\text{SNR} = 22$ dB. (f) Least squares solution for noisy samples. (g) Absolute error of the final reconstruction from noisy samples.

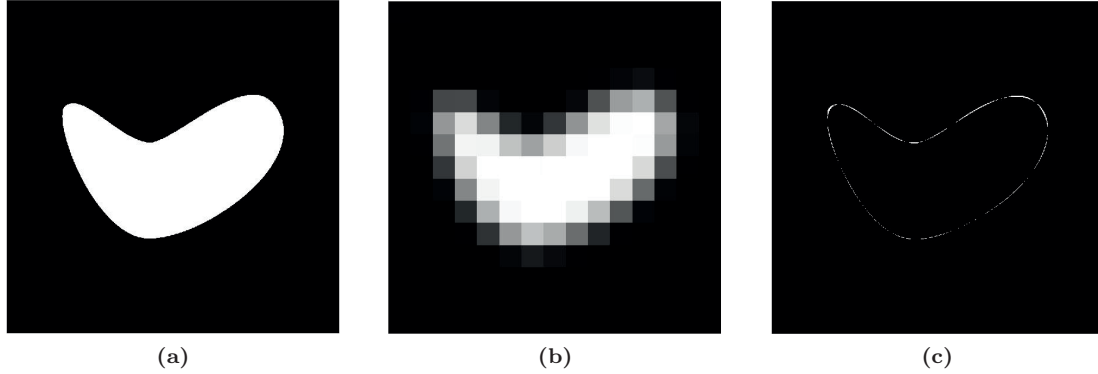


Figure 3.14: Approximation of non-annihilable curves with algebraic curves. (a) A shape with a Bézier curve boundary. (b) 15×15 noiseless samples. (c) The absolute error between the original shape and its approximation with an algebraic shape of degree 4. The reconstruction PSNR is 19.8 dB.

3.6 Conclusion

Designing sampling schemes for images with arbitrary edge geometries is still a challenging research problem. In this chapter, we proposed a sampling and reconstruction algorithm for binary images with boundary curves that are zeros of an implicit bivariate polynomial. We developed a set of linear annihilation equations from the image samples and proved that every solution of the equations restores the image boundaries, in the noiseless scenario. The primary equations involve 2D moments of the image. To make the reconstruction robust against noise, we replaced conventional moments with generalized moments associated with a compact-support 2D function that is paired with the given sampling kernel. This leads to a reconstruction algorithm from more realistic samples and extends the model to images with open boundaries.

The image model we considered in this chapter is very rich and may be used for the approximation of general shapes from their samples. Also, the idea of replacing conventional moments with generalized moments might find applications in other image processing tasks which use moments as the image descriptors.

3.7 Appendix Proof of Theorem 3.2

Proof We prove by contradiction. Assume the zero level set of \tilde{p} does not fully include \mathcal{C} ; thus, $p(x, y)$ can be factorized as

$$p(x, y) = \zeta(x, y) h(x, y),$$

where $h(x, y)$ is coprime with \tilde{p} and ζ , and has a non-trivial zero level set \mathcal{C}_h . Meanwhile, the zero level set \mathcal{C}_ζ of $\zeta(x, y)$ is included in that of \tilde{p} . Roughly speaking, h and ζ stand for parts of \mathcal{C} that are excluded and included in the zero level set of \tilde{p} , respectively. Further, let $r(x, y)$ be a polynomial with minimum degree such that $\mathbb{1}_{h(x, y) \leq 0} = \mathbb{1}_{r(x, y) \leq 0}$. If h is irreducible, we shall have $r(x, y) = h(x, y)$, otherwise, r might be different from h . In either case, we have $\deg r \leq \deg h$.

The validity of annihilation equations (3.14) and (3.15) imply

$$\iint_{\Omega} g(x)g(y)x^r y^s \tilde{p}(x, y) \frac{\partial I(x, y)}{\partial x} dx dy = 0$$

for all $0 \leq r, s, r + s \leq 2n - 1$. By linearly combining these equalities, we conclude that

$$\iint_{\Omega} g(x)g(y)q(x, y)\tilde{p}(x, y) \frac{\partial I(x, y)}{\partial x} dx dy = 0 \quad (3.22)$$

holds for any polynomial $q(x, y)$ of degree no higher than $2n - 1$. From this point on, we set q as

$$q(x, y) = \tilde{p}(x, y) \frac{\partial}{\partial x} (\zeta(x, y)r(x, y)).$$

Because $\deg q \leq \deg \tilde{p} + \deg p - 1 = 2n - 1$, this choice of q fulfills the degree constraint.

Let y^* be such that the line $y = y^*$ intersects \mathcal{C} . According to Bezout's theorem, the number of intersections m^* shall be limited to n . We assume the intersections are at $x \in \{x_i^*\}_{i=1}^{m^*}$ and conclude that

$$\frac{\partial}{\partial x} I(x, y^*) = \sum_{i=1}^{m^*} s_i \delta(x - x_i^*), \quad (3.23)$$

where $\delta(\cdot)$ is the Dirac's delta function and $\{s_i\}_i$ are sign values; $s_i = 1$ ($s_i = -1$) if $p(x, y_i^*)$ is positive (negative) at $x = x_i^* - \epsilon$ and negative (positive) at $x = x_i^* + \epsilon$ for small enough $0 < \epsilon$. Hence,

$$\begin{aligned} -s_i &= \lim_{\epsilon \rightarrow 0^+} \text{sign} \left(\frac{p(x_i^* + \epsilon, y^*) - p(x_i^* - \epsilon, y^*)}{2\epsilon} \right) \\ &= \lim_{\epsilon \rightarrow 0^+} \text{sign} \left(\frac{(\zeta \cdot r)(x_i^* + \epsilon, y^*) - (\zeta \cdot r)(x_i^* - \epsilon, y^*)}{2\epsilon} \right). \end{aligned}$$

This shows that the value of $\frac{\partial}{\partial x} (\zeta \cdot r)(x, y)$ at (x_i^*, y^*) is either 0 or has the opposite sign as s_i . This implies that

$$s_i \frac{\partial}{\partial x} (\zeta \cdot r)(x_i^*, y^*) \leq 0,$$

where equality happens only if $\frac{\partial}{\partial x} (\zeta \cdot r)(x_i^*, y^*) = 0$. By taking advantage of (3.23), we can rewrite the inner integral in (3.22) as

$$\begin{aligned} &\int g(x)g(y^*)q(x, y^*)\tilde{p}(x, y^*) \frac{\partial I(x, y^*)}{\partial x} dx \\ &= \sum_{i=1}^{m^*} s_i g(x_i^*)g(y^*)q(x_i^*, y^*)\tilde{p}(x_i^*, y^*) \\ &= \sum_{i=1}^{m^*} s_i g(x_i^*)g(y^*) (\tilde{p}(x_i^*, y^*))^2 \frac{\partial}{\partial x} (\zeta \cdot r)(x_i^*, y^*) \leq 0. \end{aligned}$$

Thus, for (3.22) to hold, $q(x, y)$ needs to vanish at all points on \mathcal{C} , and in particular, at points on \mathcal{C}_h . As h and \tilde{p} are coprime, $\tilde{p}(x, y)$ can vanish only on a finite number of points on \mathcal{C}_h (Bezout's

theorem) . This forces the zero level set of $\frac{\partial}{\partial x}(\zeta \cdot r)$ to include \mathcal{C}_h (inclusion of \mathcal{C}_h except finitely many points implies inclusion of the whole \mathcal{C}_h).

For any $(x^*, y^*) \in \mathcal{C}_h$, because of $r(x^*, y^*) = h(x^*, y^*) = 0$ we have that

$$\frac{\partial}{\partial x}(\zeta \cdot r)(x^*, y^*) = \zeta(x^*, y^*) \frac{\partial}{\partial x} r(x^*, y^*).$$

Again, since h and ζ are coprime, $\zeta(x^*, y^*) = 0$ can happen only for a finite number of points $(x^*, y^*) \in \mathcal{C}_h$. Therefore, $\frac{\partial}{\partial x} r(x^*, y^*) = 0$ should hold for all $(x^*, y^*) \in \mathcal{C}_h$; *i.e.*, the zero level set of $\frac{\partial}{\partial x} r(x, y)$ includes the zero level set of $r(x, y)$. This, however, contradicts our initial assumption that r is a polynomial with minimum degree that satisfies this property. ■

Chapter 4

Measurement-Consistent Shape Reconstruction

4.1 Introduction

The operation of capturing continuous domain visual signals as discrete (digital) images is not invertible in general. That is, the continuous domain signal cannot be exactly reconstructed based on the discrete image, unless it satisfies certain constraints such as bandlimitedness or a parametric model. In this chapter, we study the problem of recovering shape images with smooth boundaries but otherwise arbitrary geometries from a set of gray-scale samples. Among the possibly many candidates, we look for the consistent shape with minimum perimeter. We formulate this problem as a constrained optimization over the set of bilevel images, where the functional is the continuous domain total variation (TV) and the constraints encode the consistency criteria.

The number of constraints in this problem equals the number of pixels. However, we demonstrate that when a minimum-resolution requirement is satisfied, the multiple constraints can be replaced with a single one formed by a properly chosen linear combination. This reduces the problem to an equivalent TV minimization problem with a single constraint, which is known in the literature as the *Generalized Cheeger problem* [68]. A generalized Cheeger set is a shape with minimum perimeter and a fixed weighted integral. This equivalence allows us to apply the existing results that relate the Cheeger solutions to the minimizers of its convex relaxation [30, 68].

The outline of this chapter is as follows. We explicitly define the problem and the used notations in Section 4.2. We continue by reviewing the concept of Cheeger sets and the existing results in Section 4.3. In Section 4.4, we present the theoretical results that establish the equivalence between the consistent shape reconstruction and its convex relaxation. We employ the primal-dual algorithm of [104] for the numerical approximation of the solutions to the convex minimization problem in Section 4.5. This algorithm enables us to study the performance of the proposed shape recovery method of Section 4.4 through numerical experiments. Finally, we conclude the chapter in Section 4.6.

0. This chapter includes research conducted jointly with Arash Amini, Loïc Baboulaz and Martin Vetterli [59].

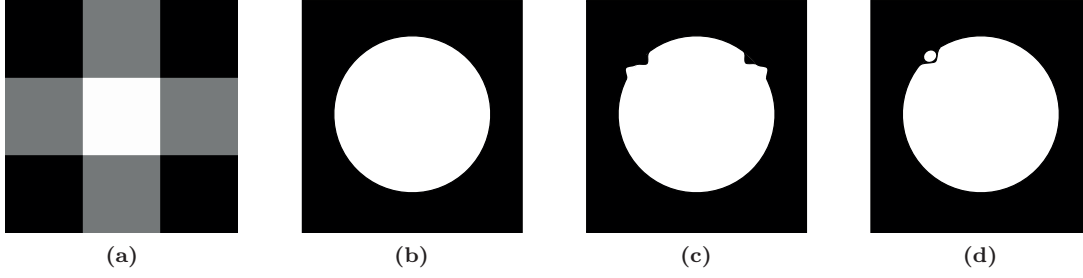


Figure 4.1: Perimeter minimization prevents unnecessary details and extra connected components to appear in the shape. In this figure, all shapes are consistent with the measurements in (a) but the shapes in (c) and (d) have higher perimeters due to the extra details on the boundary and an additional component, respectively.

4.2 Problem Definition

Let us fix the image domain as $\Omega = [0, 1]^2$ and let $\mathbf{D} = [d_{i,j}]_{\{1 \leq i,j,m\}}$ represent the output of an $m \times m$ -pixel digital camera with PSF $\bar{\phi}(x, y) = \phi(-x, -y)$ (equation (1.1)).

In the consistent image recovery problem, we wish to find an approximation $\tilde{I}(x, y)$ of the original image $I(x, y)$ that regenerates the same measurement pixels. This ensures that I and \tilde{I} are perceived as identical by the imaging device. Let $k = (j - 1)m + i$, $1 \leq k \leq m^2$ represent the equivalent index of d_{ij} in the vertical raster scan of \mathbf{D} . Also, let

$$f_k(x, y) = \frac{1}{T^2} \phi\left(\frac{x}{T} - \lceil k/m \rceil, \frac{y}{T} - ((k \bmod m) + 1)\right)$$

indicate the sampling kernel in (1.1) associated with d_k . We denote by $\mathcal{C}_\Omega(\mathbf{D}; f_1, \dots, f_{m^2})$ the set of all non-negative-valued images over the domain Ω that are consistent with $\mathbf{D} = [d_k]_{1 \leq k \leq m^2}$,

$$\mathcal{C}_\Omega(\mathbf{D}; f_1, \dots, f_{m^2}) = \left\{ I \in BV(\Omega), I \geq 0 ; \iint_\Omega I f_k \, dx \, dy = d_k, 1 \leq k \leq m^2 \right\}.$$

Here, $BV(\Omega)$ stands for the set of functions over Ω with bounded variation; i.e., all elements of $BV(\Omega)$ have well-defined and finite total variation values.

Consistent image recovery is equivalent to finding an element of $\mathcal{C}_\Omega(\mathbf{D}; f_1, \dots, f_{m^2})$. In the consistent shape recovery problem, we limit the permissible solutions to the shape characteristic functions. Let \mathcal{S} be a subset of Ω . We call \mathcal{S} a shape if it is the union of a finite number of connected subsets of Ω . In this case, we call $\chi_{\mathcal{S}}$ in equation (1.2) a shape image.

The consistent shape reconstruction problem is equivalent to finding a shape image $I = \chi_{\mathcal{S}}(x, y) \in \mathcal{C}_\Omega(\mathbf{D}; f_1, \dots, f_{m^2})$ for the set of m^2 pixels $0 \leq d_k \leq 1$ in \mathbf{D} . Among all possible candidates, we are interested in shape images with minimum perimeter. This way we reject shapes with extra connected components and excessive boundary details (see Figure 4.1).

Minimum-perimeter consistent shapes are the global minimizers of the following problem

$$\begin{aligned} & \inf_{\mathcal{S} \subseteq \Omega} \text{Per}(\mathcal{S}), & (P_0) \\ & \text{s.t. } I = \chi_{\mathcal{S}} \in \mathcal{C}_\Omega(\mathbf{D}; f_1, \dots, f_{m^2}), \end{aligned}$$

where $\text{Per}(\mathcal{S})$ is the perimeter of \mathcal{S} . Problem (P_0) is a variational non-convex problem and it is prone to having many local minima. This makes it very likely that common gradient descent methods get trapped in local minima. While in problems of this sort, global minimizers are usually all reasonable solutions, the local minima can be blatantly false. In the next sections, we show that if the discrete image \mathbf{D} satisfies a resolution requirement defined in Definition 4.4, the minimum-perimeter consistent shapes are the minimizers of a convex relaxation of (P_0) . Furthermore, we conjecture that under this condition, there is a unique minimum-perimeter consistent shape which is also the unique solution of the convex problem. In the experimental section, we present an algorithm for the recovery of this solution.

4.3 Cheeger Sets

An image is called consistent with the measurements if it complies with all the constraints in (P_0) . Essentially, each pixel of the discrete image enters (P_0) as a constraint, resulting in an optimization with many constraints. In addition, we are also restricting the search domain to bilevel images, which further complicates the minimization task. The simplest scenario of having only one single pixel (measurement) is a well-studied topic known as the Cheeger problem. There is already a rich literature regarding the existence, uniqueness properties, regularity (smoothness) of the boundary and numerical evaluation of such sets for almost arbitrary kernels f . In this section, we present a brief review of the Cheeger problem and related results upon which we build our general multi-constraint minimization problem. The details for the latter will be discussed in the next section.

The Cheeger problem can be directly extended to higher dimensions; however, for the purpose of image recovery, we focus on 2D signals in this chapter. Let Ω be a subset of \mathbb{R}^2 . The Cheeger sets of Ω are defined as those $\mathcal{S} \subset \Omega$ that minimize the ratio of the perimeter over the area,

$$\frac{\text{Per}(\mathcal{S})}{\iint_{\mathcal{S}} dx dy}. \quad (4.1)$$

It is common to represent $\text{Per}(\mathcal{S})$ in terms of the total variation of the shape image $\chi_{\mathcal{S}}$. For this purpose we invoke the *coarea* formula that for a positive function $u(x, y) : \Omega \rightarrow \mathbb{R}^{\geq 0}$ implies that

$$TV(u) = \iint_{\Omega} |\nabla u| dx dy = \int_0^{\infty} \text{Per}(E(u; \mu)) d\mu,$$

where

$$E(u; \mu) = \{(x, y) \in \Omega \mid u(x, y) \geq \mu\}$$

are the level-sets of $u(x, y)$. This immediately indicates that $\text{Per}(\mathcal{S}) = TV(\chi_{\mathcal{S}})$.

We can expand the definition of a Cheeger set by introducing two weight kernels in the nominator and denominator of (4.1) [68]. Indeed, a generalized Cheeger set is a shape minimizer of

$$\inf_{\mathcal{S} \subset \Omega, \chi_{\mathcal{S}} \in BV} \frac{\iint_{\Omega} g |\nabla \chi_{\mathcal{S}}| dx dy}{\iint_{\Omega} f \chi_{\mathcal{S}} dx dy}. \quad (4.2)$$

Note that for $f = g \equiv 1$ we obtain the standard Cheeger sets. For a simple domain such as a square, the Cheeger set is unique and has a certain shape but depending on the choice of the

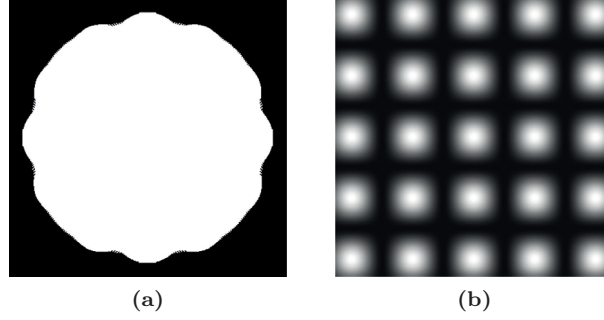


Figure 4.2: Example of (a) a generalized Cheeger set, for the weight kernels $g \equiv 1$ and f as displayed in (b).

weight kernels, generalized Cheeger sets can have very diverse shapes. Figure 4.2 displays an example of a generalized Cheeger set for $g \equiv 1$ and f as in Figure 4.2b.

Except for special choices of f and g , the minimizer of (4.2) shall not be unique. Furthermore, the minimization in (4.2) is over a non-convex set, which is computationally intractable in general. However, an interesting result by Strang in [102] (see also [30, 103]) shows that all global minimizers of (4.2) (all Cheeger sets) are the level-sets of the solution(s) to

$$\inf_{I: \Omega \rightarrow \mathbb{R}^{\geq 0}} \frac{\iint_{\Omega} g |\nabla I| \, dx \, dy}{\iint_{\Omega} f I \, dx \, dy}.$$

Note that the search domain in the latter problem consists of all non-negative-valued images (not necessarily bilevel), which is a convex set. The following statement of this result by [30] is more aligned with our approach in the next section.

Theorem 4.1 ([30])

Let I be a minimizer of

$$\inf_{I \in BV_{\Omega}(f)} \iint_{\Omega} g |\nabla I| \, dx \, dy, \quad (4.3)$$

where

$$BV_{\Omega}(f) = \left\{ I \in BV(\Omega), I \geq 0 ; \iint_{\Omega} f I \, dx \, dy = 1 \right\}.$$

Then, for every $\mu \geq 0$ such that the level-set $E(I; \mu)$ is nonempty,

$$\frac{1}{\iint_{E(I; \mu)} f \, dx \, dy} \chi_{E(I; \mu)}$$

is also a minimizer of (4.3).

In a nutshell, Theorem 4.1 states that the minimizer set of (4.3) is closed under level-set evaluation; i.e., normalized (scaled) non-empty level-sets of a minimizer also belong to the set of minimizers. This helps in finding a bilevel solution to (4.2), as finding any minimizer of the convex problem (4.3) necessarily leads to (at least) a bilevel image.

Another result proved in [30] indicates that the Cheeger sets are closed under set union. This immediately establishes the existence of a unique maximal Cheeger set that contains all the other ones [21]. Thus, we can remove the inherent ambiguity caused by non-uniqueness of the solutions to (4.3) by searching for the maximal set. However, finding the maximal set is not generally easy by considering the minimization of (4.3). A regularization technique is proposed in [21] that applies asymptotically vanishing penalty terms to the cost function (4.3) and achieves the maximal set at the limit of the minimizers. Based on this idea, a numerical method is introduced in [31] that approximates the maximal Cheeger set on a finite grid. The method is robust to discretization as the approximations converge point-wise to the continuous domain Cheeger set when the grid resolution increases.

As a final note, we discuss the influence of the weight kernels f and g . In fact, Cheeger sets consist of smooth C^2 boundaries, irrespective of the choice of f and g [68]. Nevertheless, it is known that the curvature of the boundaries is tightly controlled by these weight kernels. Formally, at each boundary point we have that [68]

$$|\kappa| \leq \frac{\mathcal{J}(\mathcal{S}) \sup f + \sup \|\nabla g\|}{\inf g}$$

where κ stands for the curvature and $\mathcal{J}(\mathcal{S})$ is the cost value of the Cheeger set determined by the ratio in (4.2). As we set $g \equiv 1$ in the rest of the chapter, the effective bound on the curvature simplifies to $|\kappa| \leq \mathcal{J}(\mathcal{S}) \sup f$. We will just briefly comment on employing a non-constant weight kernel g in Section 4.6.

4.4 Consistent Shape Recovery

Let us consider the problem (P_0) for the case where the measurement image $\mathbf{D} = [d_k]_{1 \leq k \leq m^2}$ consists of more than one pixel. Similar to the single-measurement setting, non-convexity of the problem is a computational barrier. Therefore, we opt to use a convex relaxation in the form of

$$I \in \mathcal{C}_\Omega(\mathbf{D}; f_1, \dots, f_{m^2}) \iint_\Omega |\nabla I| dx dy. \quad (P_1)$$

By extending the search domain from binary (bilevel) shapes to all non-negative-valued images, the problem becomes convex. Nevertheless, due to multiple measurement constraints, this scenario obviously deviates from the conventional Cheeger problem.

In Theorem 4.2 we show that under certain conditions, the minimization in (P_1) constrained by multiple measurements can be replaced with a similar minimization subject to a single constraint; i.e., we prove that (P_1) could potentially have an equivalent Cheeger problem. In fact, we use a wisely chosen linear combination of the measurements as the single measurement. The interpretation of (P_1) in form of a Cheeger problem automatically implies the existence of a bilevel minimizer (e.g., the maximal Cheeger set) for (P_1). Thus, all shape minimizers of (P_0) are also minimizers of the relaxed problem (P_1). Further, it proves the existence and uniqueness of a maximal consistent shape. In Theorem 4.3, we provide a simple test to verify whether a minimizer of (P_1) is the maximal shape. This helps us to validate a numerical solution obtained via minimizing (P_1)—which might not have a unique minimizer—as a binary consistent shape.

The mathematical requirements for the equivalence of (P_1) with a Cheeger problem (existence of a suitable linear combination of the measurements) is stated in Definition 4.4; essentially these

requirements imply that the sampling density used for obtaining the measurement image needs to be fine enough.

4.4.1 Promoting the use of total variation for shape recovery

Before presenting the theoretical results, we advocate the use of total variation in (P_1) for the reconstruction of bilevel images. The application of total variation in image processing goes back to the work of Rudin, Osher and Fatemi (ROF) [96] for restoring a piecewise smooth function I from its blurred and noisy version I_0

$$I_0 = AI + n,$$

where A is a linear operator (modeling, for instance, the blur in the image) and n is a random noise. The approach proposed in [96] consists in solving the following constrained minimization problem

$$\begin{aligned} \min \quad & \iint_{\Omega} |\nabla I|, \\ \text{s.t.} \quad & \iint_{\Omega} AI = \iint_{\Omega} I_0 \text{ and } \iint_{\Omega} |AI - I_0|^2 = \sigma^2, \end{aligned}$$

where σ is the standard deviation of noise. Using Lagrange multipliers, this problem was linked to the unconstrained problem

$$\min \iint_{\Omega} |\nabla I| + \frac{\lambda}{2} \|AI - I_0\|_2^2$$

for a given multiplier λ [36]. Besides, it was shown that this approach is well suited to the reconstruction of nearly piecewise constant (also called as *blocky*) images and not other images [36, 48].

Further studies revealed that the ROF model preserves the geometry of images but not the contrast, in the presence of noise [105], while replacing the ℓ_2 norm of the data fidelity term with the ℓ_1 norm makes the algorithm robust to both the contrast and geometry perturbations [38]. Specifically, it was shown that the convex minimization problem

$$\min \iint_{\Omega} |\nabla I| + \lambda \|I - \chi_{\tilde{\mathcal{S}}}\|_1$$

is equivalent to the non-convex shape denoising

$$\min_{\mathcal{S}} \text{Per}(\mathcal{S}) + \lambda |\mathcal{S} \Delta \tilde{\mathcal{S}}|,$$

where $\tilde{\mathcal{S}}$ is a noisy (with perturbed geometry) shape and Δ denotes the symmetric set difference $A \Delta B = (A - B) \cup (B - A)$ [35, 38].

Related results have been also established for the two-phase piecewise constant segmentation of a gray-scale image $\tilde{I}(x, y) : \Omega \rightarrow [0, 1]$, where the aim is to find the best approximation of $\tilde{I}(x, y)$ among all bilevel functions. This can be formulated with the functional

$$MS(\mathcal{S}, c_1, c_2) = \text{Per}(\mathcal{S}) + \lambda \iint_{\mathcal{S}} (\tilde{I}(x, y) - c_1)^2 + \lambda \iint_{\Omega \setminus \mathcal{S}} (\tilde{I}(x, y) - c_2)^2,$$

in which \mathcal{S} represents the interface between the two values c_1 and c_2 in the two-phase approximation of $\tilde{I}(x, y)$. Then, the segmentation is carried out by the minimization problem

$$\min_{\mathcal{S} \subset \Omega, c_1, c_2 \in \mathbb{R}} MS(\mathcal{S}, c_1, c_2).$$

An interesting result in [39] asserts that for any given $c_1, c_2 \in \mathbb{R}$, every non-empty level set of the solution of the convex relaxation

$$\min_{0 \leq I(x, y) \leq 1} \iint_{\Omega} |\nabla I| + \lambda \iint_{\Omega} \left\{ (\tilde{I}(x, y) - c_1)^2 - (\tilde{I}(x, y) - c_2)^2 \right\} I(x, y)$$

forms a global minimizer for $MS(\mathcal{S}, c_1, c_2)$.

Finally, we would like to mention the immediate application of the Cheeger results in 3D shape modeling and reconstruction [110].

4.4.2 Theoretical results

We start by defining the maximal consistent shape.

Definition 4.1

A maximal consistent shape with minimum perimeter, or MCSMP in short, is a solution to (P_0) whose support contains the support of all other minimizers of (P_0) .

Note that a MCSMP does not always exist. In general, the support union of two minimizers of (P_0) does not necessarily generate a minimizer by scaling. It is evident by this fact that the claimed equivalent Cheeger problem plays a crucial role in our results. In Definition 4.4 below we will describe the sufficient conditions that enable us to associate (P_0) or (P_1) to a Cheeger problem.

Before stating Definition 4.4, we introduce a few notations used in the rest of this section. As we need to linearly combine the measurement constraints, we represent the n -dimensional coefficient set for the convex combinations by Δ_n :

$$\Delta_n \triangleq \left\{ (\lambda_1, \dots, \lambda_n) \in \mathbb{R}^n \mid 0 \leq \lambda_i, \sum_{i=1}^n \lambda_i = 1 \right\}.$$

For non-negative-valued images, a zero measurement can only happen when the image vanishes over the support of the corresponding sampling kernel. Thus, we can exclude the support region from our search domain.

Definition 4.2

For the measurements $\mathbf{D} = [d_k]_{1 \leq k \leq m^2}$ corresponding to the pixels $0 \leq d_k \leq 1$ and sampling kernels f_1, \dots, f_{m^2} , let ρ denote the number of non-zero pixels and

$$A = \{i \mid d_i > 0\} = \{a_1, \dots, a_\rho\}$$

stand for the index set of active pixels. We define the reduced domain Ω_r by

$$\Omega_r = \Omega_r(\mathbf{D}; f_1, \dots, f_{m^2}) = \Omega \setminus \bigcup_{i \in \{1, \dots, m^2\} \setminus A} \text{supp}(f_i).$$

Definition 4.3

For the measurements $\mathbf{D} = [d_k]_{1 \leq k \leq m^2}$, sampling kernels f_1, \dots, f_{m^2} , and a vector $\boldsymbol{\lambda} \in \Delta_\rho$, we define the reduced kernel $f^\boldsymbol{\lambda} : \Omega_r \mapsto \mathbb{R}^{\geq 0}$ by

$$f^\boldsymbol{\lambda} = \left(\sum_{k=1}^{\rho} \lambda_k f_{a_k} \right) / \left(\sum_{k=1}^{\rho} \lambda_k d_{a_k} \right).$$

Here, ρ , Ω_r , and a_k are as defined in Definition 4.2.

Now, we are prepared to state the Cheeger problem equivalence requirements.

Definition 4.4

As before, let $\mathbf{D} = [d_k]_{1 \leq k \leq m^2}$ be the measurements captured by sampling kernels f_1, \dots, f_{m^2} with $0 \leq d_i$, leading to ρ , A , and Ω_r as in Definition 4.2. For an arbitrary $\boldsymbol{\lambda} \in \Delta_\rho$, we define $I^\boldsymbol{\lambda} = \alpha \chi_S$ to be the solution of (4.3) corresponding to the maximal Cheeger set S with $f^\boldsymbol{\lambda}$, when the domain is restricted to Ω_r . We call $(\mathbf{D}; f_1, \dots, f_{m^2})$ reducible if A can be partitioned into K_1 and K_2 such that

1. $\forall k \in K_1, \boldsymbol{\lambda} \in \Delta_\rho, \lambda_k = 0 : \iint_{\Omega_r} I^\boldsymbol{\lambda} f_k \, dx \, dy < d_k$,
2. $\forall k \in K_2, \boldsymbol{\lambda} \in \Delta_\rho : \iint_{\Omega_r} I^\boldsymbol{\lambda} f_k \, dx \, dy \leq d_k$.

It was explained earlier that the measurements d_i obtained from a binary shape through normalized sampling kernels satisfy $0 \leq d_i \leq 1$. The requirements in Definition 4.4 simply indicate that the maximal Cheeger solution corresponding to any convex combination of the kernels except a given one, should result in a strictly smaller measurement observed by the excluded kernel. Intuitively, we expect the Cheeger solution to have less contribution over the support of the excluded kernel. However, there are some exceptions; imagine the case where the support of a 3×3 block of measurement kernels completely coincide with the interior of the binary shape. Thus, we shall have a block of all-one measurements. Now, it is likely that the maximal Cheeger set corresponding to a linear combination of the 8 surrounding kernels (but missing the middle one) using symmetric weights fully covers the support of the kernel in the middle. Hence, measuring this solution via the middle kernel results in $d_i = 1$, instead of being strictly less than 1. The partitions K_1 and K_2 in Definition 4.4 are introduced to distinguish between the ordinary (K_1) and exceptional (K_2) cases. We postpone further discussion and clarifications about this definition to Section 4.4.3.

Theorem 4.2

Let $(\mathbf{D}; f_1, \dots, f_{m^2})$ be reducible according to Definition 4.4. Then, all solutions of the non-convex problem (P_0) are included in the minimizers of its convex relaxation (P_1) . Moreover, the solution set of (P_1) contains a unique MCSMP.

Our proof of Theorem 4.2 relies on the following lemma, the proof of which is provided in the appendix.

Lemma 4.1

For a given dimension n and a set $\{d_k\}_{k=1}^n \subset \mathbb{R}$, let K_1, K_2 be a partition of $\{1, \dots, n\}$, with the possibility of $K_1 = \emptyset$ or $K_2 = \emptyset$, and let $v : \Delta_n \mapsto \mathbb{R}^n$ be a continuous function that satisfies

1. $\forall \boldsymbol{\lambda} \in \Delta_n : \boldsymbol{\lambda}^T \cdot v(\boldsymbol{\lambda}) = \sum_{k=1}^n \lambda_k d_k$,
 2. $\forall k \in K_1, \boldsymbol{\lambda} \in \Delta_n : v_k(\boldsymbol{\lambda}) < d_k$.
- $$\lambda_k=0$$
3. $\forall k \in K_2, \boldsymbol{\lambda} \in \Delta_n : v_k(\boldsymbol{\lambda}) \leq d_k$

Then, there exists $\boldsymbol{\lambda}^* \in \Delta_n$ such that $v(\boldsymbol{\lambda}^*) = [d_1, \dots, d_n]^T$.

Proof of Theorem 4.2. The main ingredient of the proof is to show that under reducibility condition, (P_0) and (P_1) can be associated with a Cheeger problem. To show this, first note that $\mathcal{C}_\Omega(\mathbf{D}; f_1, \dots, f_{m^2})$ is essentially the same as $\mathcal{C}_{\Omega_r}(\mathbf{D}_r; f_{a_1}, \dots, f_{a_\rho})$, where ρ, A, Ω_r are defined in Definition 4.2 and $\mathbf{D}_r = [d_k]_{k \in A}$. In addition, for all $\boldsymbol{\lambda} \in \Delta_\rho$, we have that

$$\mathcal{C}_{\Omega_r}(\mathbf{D}_r; f_{a_1}, \dots, f_{a_\rho}) \subseteq \mathcal{C}_{\Omega_r}(1; f^\lambda) = BV_{\Omega_r}(f^\lambda).$$

Therefore, any minimizer of (4.3) that falls inside $\mathcal{C}_{\Omega_r}(\mathbf{D}_r; f_{a_1}, \dots, f_{a_\rho})$ is also a minimizer of (P_1) . Besides, if (P_1) and (4.3) have a common minimizer, then, all the solutions of (P_1) shall be among the solutions of (4.3). This is indeed, what we aim to prove.

Let I^λ be the maximal Cheeger set solution of (4.3) on Ω_r corresponding to the weight kernel f^λ . Consider the function

$$v(\boldsymbol{\lambda}) \triangleq \left[\iint_{\Omega_r} I^\lambda f_{a_1}, \dots, \iint_{\Omega_r} I^\lambda f_{a_\rho} \right]^T.$$

We demonstrate that $v(\cdot)$ satisfies the conditions of Lemma 4.1. The first condition directly follows from

$$1 = \iint_{\Omega_r} I^\lambda f^\lambda = \frac{1}{\sum_{k=1}^\rho \lambda_k d_{a_k}} \iint_{\Omega_r} I^\lambda \sum_{k=1}^\rho \lambda_k f_{a_k}.$$

The reducibility property of $(\mathbf{D}_r; f_{a_1}, \dots, f_{a_\rho})$ also establishes Conditions (2) and (3) of Lemma 4.1. Consequently, there exists $\boldsymbol{\lambda}^* \in \Delta_\rho$ such that

$$v_k(\boldsymbol{\lambda}^*) = \iint_{\Omega_r} I^{\lambda^*} f_{a_k} dx dy = d_{a_k}, \quad 1 \leq k \leq \rho.$$

This means that the bilevel maximal Cheeger solution I^{λ^*} , which minimizes (4.3), is also consistent with the measurements \mathbf{D}_A . Hence, I^{λ^*} is also a minimizer of (P_1) as well as (P_0) ; *i.e.*, the three problems (4.3) with f^{λ^*} over Ω_r , (P_1) and (P_0) share a minimizer. This proves the first part of the claim.

As for the second part, note that all minimizing shapes of (P_0) are Cheeger solutions of (4.3). Thus, their support should be included in the support of the maximal Cheeger solution I^{λ^*} . In words, I^{λ^*} is a MCSMP. \blacksquare

Theorem 4.2 states that under reducibility, the solution set of (P_1) is guaranteed to contain a MCSMP. Although we believe that the MCSMP is the unique solution of (P_1) under reducibility, it is yet to be proven. However, we introduce a test in Theorem 4.3 to verify whether an obtained

solution to (P_1) is the MCSMP. This test helps us in simulation results, where we implement a minimization technique and eventually obtain a solution with a numerical precision. First, it is difficult to make sure whether the result is precisely bilevel, and second, even if it is bilevel, is it the MCSMP?

Theorem 4.3

Let $(\mathbf{D}; f_1, \dots, f_{m^2})$ with $d_i = 1$ for some i be reducible (at least one measurement equal to one). If the point values of a solution to (P_1) never exceed 1, then, this solution is the MCSMP and it is binary (non-zero values are all 1).

Proof. Let $I(x, y) \leq 1$ be a solution to (P_1) , and let i be the index of a measurement equal to 1, i.e., $d_i = 1$. By comparing $I(x, y) \leq 1$ and $d_i = 1$, we conclude that for all $(x, y) \in \text{supp}(f_i)$ we should have $I(x, y) = 1$ (the kernels are normalized). If I is the MCSMP, as it takes the value 1, it needs to be binary and the proof is complete. Therefore, let us assume the MCSMP to be $\tilde{I} \neq I$. As previously shown, the support of \tilde{I} contains the support of I , which obviously contains the support of f_i . As \tilde{I} is constant over its support and is also consistent with measurement d_i , we should have that $\tilde{I}(x, y) = 1$ for all $(x, y) \in \text{supp}(f_i)$. Thus, \tilde{I} is binary. However, this implies that I never exceeds \tilde{I} at any point, while they generate the same set of measurements. In turn, this suggests that I cannot be less than \tilde{I} on a set of non-zero measure. In other words, I and \tilde{I} are essentially equal at all points. ■

For recovering a binary shape from discrete measurements, we infer the following: when the sampling density is high enough to provide the reducibility condition for the measurements, the studied convex problem is potentially able to return a consistent binary shape with minimum perimeter. Besides, the boundary of the output shall be a C^2 curve.

Remark 4.1

The reducibility requirement is a sufficient condition for the claims of Theorem 4.2 and 4.3 to hold. However, it is by no means a necessary condition. In fact, we have experimentally found cases for which the claims hold, while the reducibility requirement is not fulfilled.

4.4.3 The sampling density requirement

Earlier, we claimed that the reducibility condition in Definition 4.4 is effectively a requirement on the minimum sampling density. Here, we illustrate this intuition by some examples.

First, we consider the sampling of the shape in Figure 4.3a over a 3×3 -pixel grid, employing the bilinear B-spline sampling kernel depicted in Figure 4.3b. This generates the measurements

$$\mathbf{D} = \begin{bmatrix} 0.5634 & 0.0523 & 0.5750 \\ 0.8996 & 0.9016 & 0.8882 \\ 0.5247 & 0.8817 & 0.5097 \end{bmatrix}.$$

Particularly, we focus on the d_4 measurement pixel (or d_{12} in the usual matrix indexing format). It is evident that the value of this measurement is considerably lower than its neighboring measurement pixels. Intuitively, this sharp transition violates the resolution requirement. Now, we check the reducibility condition: let us exclude the d_4 pixel and apply equal weights for a convex combination of the remaining measurements, i.e., $\boldsymbol{\lambda} = [1, 1, 1, 0, 1, 1, 1, 1, 1]/8 \in \Delta_9$. Figure 4.3c depicts the reduced sampling kernel f^λ , and Figure 4.3d shows the corresponding maximal

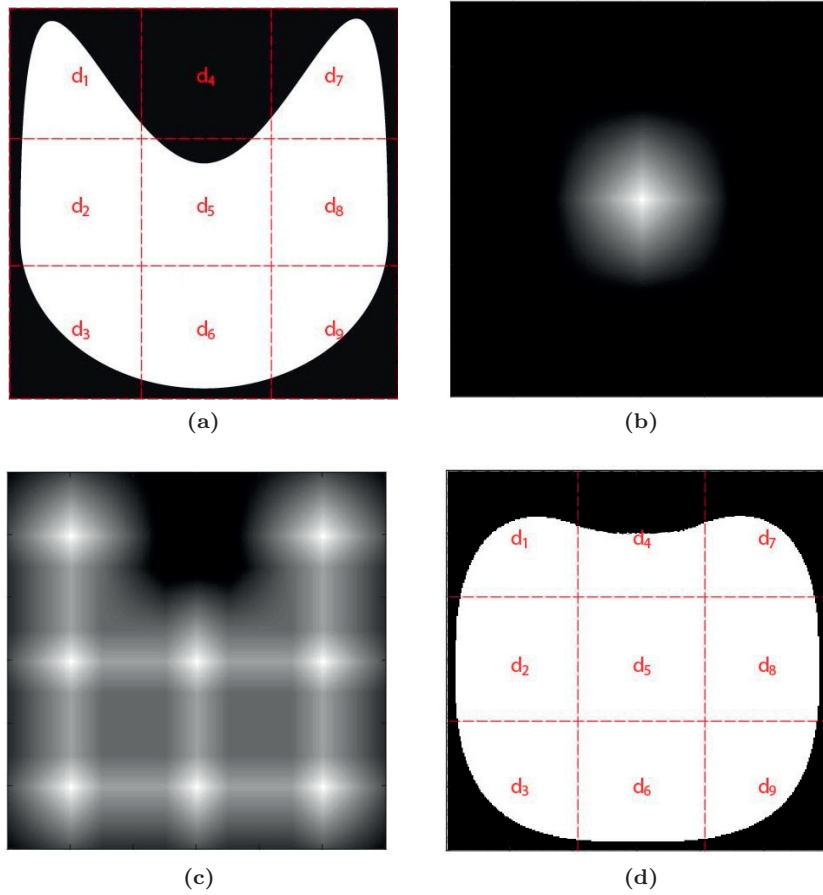


Figure 4.3: Violation of the reducibility criterion due to the low sampling density. (a) shows the original binary image over a 3×3 sampling grid. This generates the measurement $d_4 = 0.0523$, when the sampling kernels are the shifts of the bilinear B-spline kernel in (b). (c) shows the reduced sampling kernel f^λ corresponding to $\lambda = [1, 1, 1, 0, 1, 1, 1, 1, 1]/8$, that results in the Cheeger solution (d) with levels 0 and 0.9577 (reproducing the larger measurement $d_4 = 0.5247$).

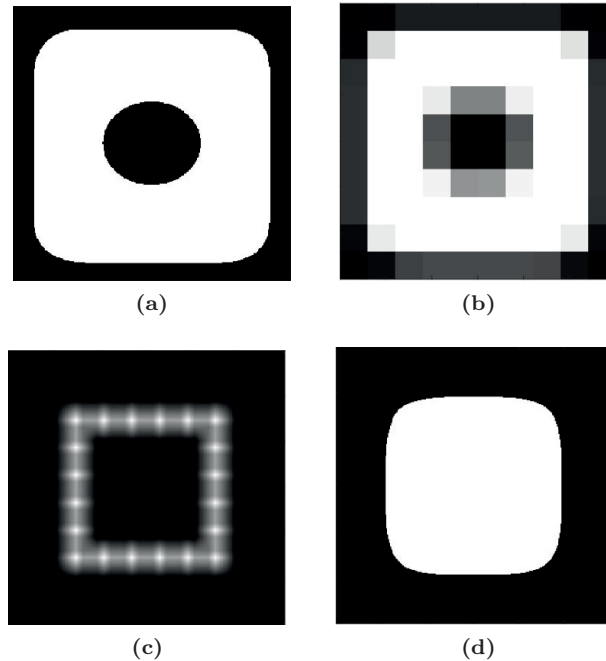


Figure 4.4: The measurements of shapes with internal holes never satisfy the reducibility requirement, no matter how high is the measurement density, unless the original domain is replaced with the reduced domain. (a) A binary shape image with an internal hole, (b) the corresponding 10×10 measurements, with $d_{55} = d_{56} = d_{65} = d_{66} = 0$, (c) reduced kernel f^λ , with equal contributions from the 20 kernels associated with pixels on the borders of the central 6×6 sub-grid, and (d) the maximal Cheeger solution with levels 0 and 0.9891.

Cheeger solution. Although d_4 did not contribute in this Cheeger solution, we observe substantial leakage over its region from the neighboring pixels. Thus, $(\mathbf{D}, f_1, \dots, f_9)$ is not reducible. Oftentimes, sharp transitions between neighboring pixel values indicate lack of sufficient density for sampling the boundary curve of the shape (possibly, parts with high curvature). Similarly, the reducibility condition prevents the value of a pixel dropping substantially below its neighbors.

One of the shortcomings of reformulating (P_1) as (4.3) using a single reduced kernel f^λ is that the Cheeger solution never admits a hole. Figure 4.4 provides a pictorial explanation. Here, we would like to recover the shape image in Figure 4.4a from its discrete measurements on a 10×10 grid. The hole causes four vanishing middle pixels (Figure 4.4b), which make it obvious that the shape content is 0 in the middle. We now consider a reduced kernel by linearly combining (with equal weights) only the 20 kernels associated with the pixels on the perimeter of the central 6×6 sub-grid (Figure 4.4c). As claimed, the Cheeger solution to (4.3) depicted in Figure 4.4d has no holes and completely covers the middle part. This seems to violate the reducibility condition, no matter how high we set the sampling density. However, note that we remove the 0 pixels from the domain in Definition 4.4. Therefore, the Cheeger solution over the reduced domain is forced to have a hole, although it is not considered as hole with respect to the reduced domain.

The reducibility condition in Definition 4.4 is a useful guarantee for recovering a shape image.

However, verifying it for a given set of measurements and sampling kernels is a combinatorial problem in general. For the purpose of illustration, we investigate the simple case with 2×2 measurement pixels. Let $\mathbf{D} = \begin{bmatrix} d_1 & d_3 \\ d_2 & d_4 \end{bmatrix}$ with elements in $[0, 1]$ represent the measurement matrix. Without loss of generality, we assume that $d_4 = \rho \leq 1$ is the largest element. To verify the reducibility condition, we need to exclude each pixel, apply an arbitrary convex combination on the rest and check an inequality. As we can categorize d_4 to the K_2 set in Definition 4.4, the inequalities when d_4 is excluded are trivial. To verify other inequalities, note that we can scale all measurements by the factor $\frac{1}{\rho}$ (or any other positive real). In fact, the scaling does not affect the support set of the Cheeger solutions. Consequently, the reducibility condition for \mathbf{D} , boils down to a set of inequalities on each of $\frac{d_1}{\rho}, \frac{d_2}{\rho}, \frac{d_3}{\rho}$ in terms of the other two:

$$\begin{aligned} d_1 &> \rho Z\left(\frac{d_2}{\rho}, \frac{d_3}{\rho}\right), \\ d_2 &> \rho Y\left(\frac{d_1}{\rho}, \frac{d_3}{\rho}\right), \\ d_3 &> \rho Y\left(\frac{d_1}{\rho}, \frac{d_2}{\rho}\right). \end{aligned}$$

The symmetries of the problem indicate that the lower-bounds on d_2 and d_3 can be represented using the same function ($Y(\cdot, \cdot)$), and the lower-bound $Z(\cdot, \cdot)$ on d_1 is symmetric with respect to the two inputs. In Figures 4.5 and 4.6 we depict the functions Y, Z for two choices of the sampling kernel, namely, the box-spline (Figure 4.5) with non-overlapping kernels and bilinear B-spline kernels with 50% overlap (Figure 4.6). The overlap introduces correlation among the neighboring pixels, which naturally leads to tighter regions for validity of the reducibility condition. This is indicated by larger Y and Z values. For instance, the measurement set $\mathbf{D} = \begin{bmatrix} 0.576 & 0.72 \\ 0.216 & 0.216 \end{bmatrix}$ is reducible under the box-spline sampling kernels, but not under the bilinear B-spline kernels. This issue is explicitly explained in the following remark.

Remark 4.2

The involved notion of local smoothness in the reducibility requirement is relative to the sampling kernel. For PSFs with wider supports, we expect more correlation among neighboring samples, resulting in smoother local transitions. However, in the same way, the neighboring samples are likely to contribute in the support of an excluded sample when examining the reducibility requirement. Therefore, the reducibility requirement for a wider PSF sets stronger constraints on the variations among neighboring samples (i.e., smoothness of higher degree/level). This explains that the reducibility requirement mainly depends on the sampling density, rather than the PSF.

4.5 Numerical Experiments

In this section, we aim at numerically calculating the optimal solution(s) of the convex problem (P_1). For this purpose, we restrict the simulations to the discrete setting. Below, we first explain the equivalent problem in the discrete domain and then, present the simulation results.

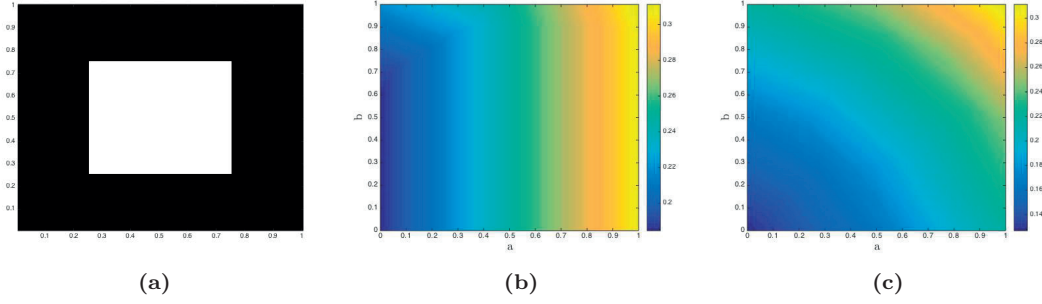


Figure 4.5: The approximate functions (b) Y and (c) Z for the characterization of reducible measurements $\mathbf{D}_{2 \times 2}$ when the kernels f_1, f_2, f_3, f_4 are shifts of the box-spline kernel in (a) centered at point $(0.25, 0.75)$, $(0.25, 0.25)$, $(0.75, 0.75)$ and $(0.75, 0.25)$, respectively.

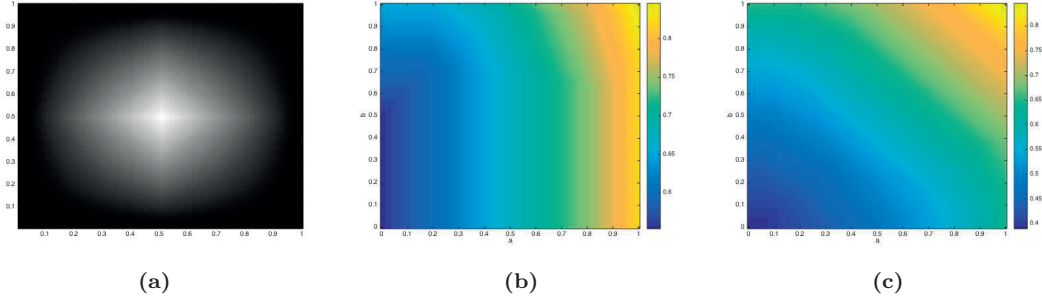


Figure 4.6: The approximate functions (b) Y and (c) Z for the characterization of reducible measurements $\mathbf{D}_{2 \times 2}$ when the kernels f_1, f_2, f_3, f_4 are shifts of the bilinear B-spline kernel in (a) centered at point $(0.25, 0.75)$, $(0.25, 0.25)$, $(0.75, 0.75)$ and $(0.75, 0.25)$, respectively.

4.5.1 Discrete formulation

For conducting computer simulations, we are limited to discrete scenarios. Therefore, we discretize the domain Ω (and subsequently all the functions defined on Ω) with a finite step-size $h \sim \frac{1}{N}$ for some large integer N . This will approximate Ω and the continuous domain objects I, f_1, \dots, f_{m^2} by their pseudo samples at the 2D grid

$$\{(ih, jh); i, j = 1, 2, \dots, N\}$$

resulting in $\mathbb{R}^{N \times N}$ matrices. In the discretized version, we approximate the gradient operator by evaluating the forward differences; for instance we approximate ∇I with an $\mathbb{R}^{N \times N \times 2}$ tensor defined as

$$(\nabla \mathbf{I})_{i,j,k} = (\nabla \mathbf{I})_{i,j}^k \quad (4.4)$$

where

$$\begin{aligned} (\nabla \mathbf{I})_{i,j}^1 &= \begin{cases} \mathbf{I}_{i+1,j} - \mathbf{I}_{i,j} & \text{if } i < N, \\ 0 & \text{if } i = N, \end{cases} \\ (\nabla \mathbf{I})_{i,j}^2 &= \begin{cases} \mathbf{I}_{i,j+1} - \mathbf{I}_{i,j} & \text{if } j < N, \\ 0 & \text{if } j = N. \end{cases} \end{aligned} \quad (4.5)$$

It is shown that in the asymptotic regime of $N \rightarrow \infty$, the results obtained with the discretized model converge to their continuous domain counterpart introduced in (P_1) [34].

One of the standard approaches for solving the associated discrete minimization is the gradient descent algorithm, which is rather slow in high dimensions (small step-size h). Recently, the piecewise-smooth Mumford-Shah functional for image restoration has been relaxed and reformulated as a min-max problem. The latter formulation allows for its implementation via primal-dual projection algorithms [92, 104]. These algorithms are fast and enjoy convergence guarantees. In this chapter, we use the dual formulation of total variation [32, 34, 40] to cast (P_1) (with a general non-negative-valued weight kernel g) as the min-max problem

$$\begin{aligned} \min_{I \in \mathcal{C}} \iint g |\nabla I| &= \min_{I \in \mathcal{C}} \max_{|\zeta|_2 \leq g} \left\{ \iint -I \operatorname{div} \zeta \right\} \\ &= \min_{I \in \mathcal{C}} \max_{|\zeta|_2 \leq g} \langle -I, \operatorname{div} \zeta \rangle, \end{aligned} \quad (4.6)$$

with the dual variable $\zeta : \Omega \rightarrow \mathbb{R}^2$. Then, we apply a variation of the aforementioned primal-dual algorithms to solve (4.6). Here, div stands for the divergence and is defined as the negative of the gradient adjoint.

Each iteration of the obtained algorithm alternates between a gradient descent and a gradient ascent on the primal and dual variables, respectively. In short, the update equations are as follows:

$$\zeta^{(k+1)} = \operatorname{Proj}_{\mathcal{B}(\mathbf{g})}(\zeta^k + \sigma_k \nabla \bar{\mathbf{I}}^{(k)}), \quad (4.7)$$

$$\mathbf{I}^{(k+1)} = \operatorname{Proj}_{\mathcal{C}_\Omega(\mathbf{D}; \mathbf{f}_1, \dots, \mathbf{f}_{m_2})}(\mathbf{I}^{(k)} + \tau_k \operatorname{div} \zeta^{(k+1)}), \quad (4.8)$$

$$\theta_k = \frac{1}{\sqrt{1 + 4\tau_k}}, \quad \tau_{k+1} = \theta_k \tau_k, \quad \sigma_{k+1} = \sigma_k / \theta_k,$$

$$\bar{\mathbf{I}}^{(k+1)} = \mathbf{I}^{(k+1)} + \theta_k (\mathbf{I}^{(k+1)} - \mathbf{I}^{(k)}),$$

where k represents the iteration index. Here, the notation $\operatorname{Proj}_A(\cdot)$ stands for the orthogonal projection of the argument onto the set A and $\mathcal{B}(\mathbf{g})$ represents the ball with radius \mathbf{g} in the space of $N \times N \times 2$ tensors:

$$\mathcal{B}(\mathbf{g}) = \left\{ \mathbf{u} \in \mathbb{R}^{N \times N \times 2} ; \sqrt{\mathbf{u}_{i,j,1}^2 + \mathbf{u}_{i,j,2}^2} \leq \mathbf{g}_{i,j} \right\}.$$

Hence, $\operatorname{Proj}_{\mathcal{B}(\mathbf{g})}(\cdot)$ in (4.7) scales only the points outside the ball $\mathcal{B}(\mathbf{g})$. In this chapter, we only consider $g \equiv 1$; nevertheless, the algorithm works for general non-negative weight kernels g .

The more involved operator $\operatorname{Proj}_{\mathcal{C}_\Omega(\mathbf{D}; \mathbf{f}_1, \dots, \mathbf{f}_{m_2})}(\mathbf{I})$ in (4.8) projects \mathbf{I} onto the set of non-negative-valued matrices that are consistent with samples in \mathbf{D} . To better explain this projection, we use the notation $\operatorname{vec}(\mathbf{I})$ for the vector formed by concatenating all the columns of \mathbf{I} . This

way, the samples are represented by $\mathbf{F}\text{vec}(\mathbf{I})$, where \mathbf{F} is the $m^2 \times N^2$ matrix

$$\mathbf{F} = \begin{bmatrix} (\text{vec}(\mathbf{f}_1))^T \\ (\text{vec}(\mathbf{f}_2))^T \\ \dots \\ (\text{vec}(\mathbf{f}_{m^2}))^T \end{bmatrix}.$$

With this convention, projection onto the set of measurement consistent images returns the solution to

$$\begin{aligned} \arg \min_{\text{vec}(\tilde{\mathbf{I}})} \|\text{vec}(\mathbf{I}) - \text{vec}(\tilde{\mathbf{I}})\|_2^2 \\ \text{s.t. } \mathbf{F}\text{vec}(\tilde{\mathbf{I}}) = \text{vec}(\mathbf{D}), \end{aligned}$$

which admits the closed form

$$\text{vec}(\tilde{\mathbf{I}}) = \text{vec}(\mathbf{I}) - \mathbf{F}^T(\mathbf{F}\mathbf{F}^T)^{-1}(\mathbf{F}\text{vec}(\mathbf{I}) - \text{vec}(\mathbf{D})).$$

For separable sampling kernels, i.e. $\phi(x, y) = \phi(x)\phi(y)$, we can implement sampling along the rows and columns separately using a matrix $\mathbf{F}_{m \times N}$ as $\mathbf{F}\mathbf{I}\mathbf{F}^T$. In this case,

$$\tilde{\mathbf{I}} = \mathbf{I} - \mathbf{F}^T(\mathbf{F}\mathbf{F}^T)^{-1}(\mathbf{F}\mathbf{I}\mathbf{F}^T - \mathbf{D})(\mathbf{F}\mathbf{F}^T)^{-1}\mathbf{F}^T.$$

Finally, we find $\text{Proj}_{\mathcal{C}_\Omega(\mathbf{D}; \mathbf{f}_1, \dots, \mathbf{f}_{m^2})}(\mathbf{I})$ by alternating the projections onto the set of measurement-consistent and non-negative valued matrices, using the POCS algorithm [16].

The initial values $\mathbf{I}^{(0)}$ and $\zeta^{(0)}$ are arbitrary, with $\tilde{\mathbf{I}}^0 = \mathbf{I}^{(0)}$ and time steps $\tau_0\sigma_0\|\nabla\|^2 < 1$ [104]. By analogy (continuous setting), the divergence in (4.8) shall be the negated adjoint of the discrete gradient used in (4.7). For the forward difference gradient in equations (4.4)-(4.5), this leads to

$$\begin{aligned} (\text{div}\zeta)_{ij} = & \begin{cases} \zeta_{i,j}^1 - \zeta_{i-1,j}^1 & \text{if } 1 < i < N, \\ \zeta_{i,j}^1 & \text{if } i = 1, \\ -\zeta_{i-1,j}^1 & \text{if } i = N, \end{cases} \\ & + \begin{cases} \zeta_{i,j}^2 - \zeta_{i,j-1}^2 & \text{if } 1 < j < N, \\ \zeta_{i,j}^2 & \text{if } j = 1, \\ -\zeta_{i,j-1}^2 & \text{if } j = N. \end{cases} \end{aligned}$$

4.5.2 Simulation results

In the first experiment, we study the effect of the number of measurements on the reconstructed images obtained with the proposed algorithm. Recalling the result of the previous section, we expect the solution of (P_1) to be binary, given adequate number of measurement pixels. In this experiment, we employ a shape image with a parametric description, composed of a semicircle laid on one side of an equilateral triangle (Figure 4.7a). This enables us to precisely access and display the image at arbitrary fine resolutions as a reference. Figure 4.7a shows the image at the resolution 2000×2000 . Figs. 4.7b, 4.7c and 4.7d show the solutions of algorithm (P_1) with the same resolution applied to the measurement of sizes 40×40 , 50×50 and 80×80 , respectively. All measurements are generated with a box-spline kernel. The original shape has

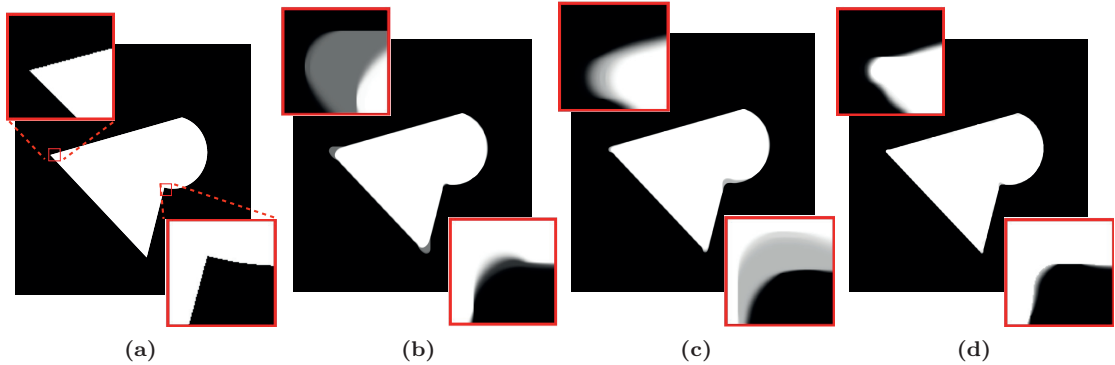


Figure 4.7: The performance of algorithm (P_1) in shape recovery: (a), (b), (c) and (d) show the original shape image displayed with the resolution 2000×2000 and its approximations using 40×40 , 50×50 and 80×80 measurements, respectively. Note that the reconstructed images are binary only when the number of measurements is large enough.

non-smooth details around the corners and thus, to facilitate comparison, we enlarged the reconstructed images around these areas. The results reveal that with lack of enough measurements, the reconstructed images have more than two levels. It seems that the 80×80 -pixel image provides enough measurements to have a binary optimal solution for (P_1) .

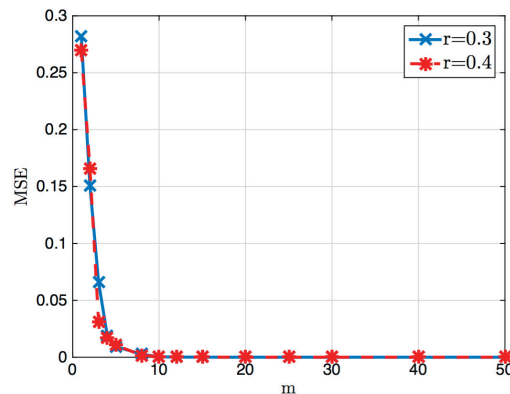


Figure 4.8: The average MSE of the recovered binary images constrained by $m \times m$ samples of random circles with fixed radius for two radii $r = 0.3$ and $r = 0.4$.

In a similar experiment, we examine the performance of our algorithm in recovering circles from different number of measurements. For this purpose, we run a Monte Carlo experiment by generating 20 circles with fixed radius and random centers in the image plane. We then consider outputs of the algorithm at resolution 600×600 constrained with $m \times m$ analytic measurements of the circles with box-spline PSFs and different values of m . Figure 4.8 shows the average mean squared errors of the reconstructed images (after thresholding at level 0.5) versus m for two different radii. The plots in this figure clearly indicate that the algorithm always perfectly

Table 4.1: Quantitative evaluation of the proposed algorithm (numbers in dB)

	shape in Figure 4.9a		shape in Figure 4.9e	
	image PSNR	measurement PSNR	image PSNR	measurement PSNR
proposed solution	29.1507	58.3316	43.8839	63.3429
linear interpolation	26.4397	41.4224	33.7172	49.1746

recovers the circles from $m \times m$ measurements when m is greater than 10.

Next, we examine the solutions of (P_1) to 200×200 -pixel discrete images of the shapes depicted in Figures 4.9a and 4.9e at resolution 1000×1000 (Figure 4.9e is taken from the middle part of Figure 1.2). The sampling kernel for this experiment is the biquadratic B-spline. Figure 4.9 presents the same enlarged sections of the original shapes, the discrete images (just for a visual comparison) and their reconstructions with the proposed algorithm. The figures demonstrate that both reconstructed images are almost binary. Also, Table 4.1 shows the quantitative evaluation of the reconstructed images. In this table, we also compare our results with the ones obtained by the interpolation of the measurement images with the bilinear B-spline kernel, followed by a thresholding at level 0.5. For a fair comparison, we also threshold our results to calculate the PSNRs. The numbers in this table clearly indicate the success of our proposed algorithm for consistent shape reconstruction.

For a given shape image, the resolution requirement in Definition 4.4 mainly depends on the sampling grid, rather than the PSF. To examine this fact, we repeat the experiment in Figure 4.9 by regenerating a 200×200 discrete image from Figure 4.9a using a stretched biquadratic B-spline sampling kernel with an effective support of 40×40 pixels. The result is the highly blurred image in Figure 4.10a. Also, Figure 4.10b shows the enlarged section equivalent to Figure 4.9b. The quality of the reconstructed image in Figure 4.10c (PSNR = 33.8dB) confirms that the sampling grid outweighs the choice of the PSF in determining the performance.

Finally in the last experiment, we study the performance of the proposed method in a setting severely deficient in the number of measurements. For this purpose, we consider a recent image by the *New Horizons* spacecraft in July 2015 from a moon of Pluto named *Hydra*. Figure 4.11a depicts the received measurements. Although a high resolution imager is used, due to the long distance of the spacecraft to Hydra compared to the size of Hydra, we observe a highly pixelated image. According to the available data, the effective PSF width of the imager is around 1.5 pixels, which we model by a dilated biquadratic B-spline. Figure 4.11b shows the output of the convex program to the measurements by applying the approximate PSF. As the measurements are too few, the reconstructed image is not bilevel (indeed, it is not unlikely to assume the image of Hydra being binary from this distance). Nevertheless, it is interesting to note that the obtained multi-level image is not far from the processed image released by NASA in Figure 4.11c.

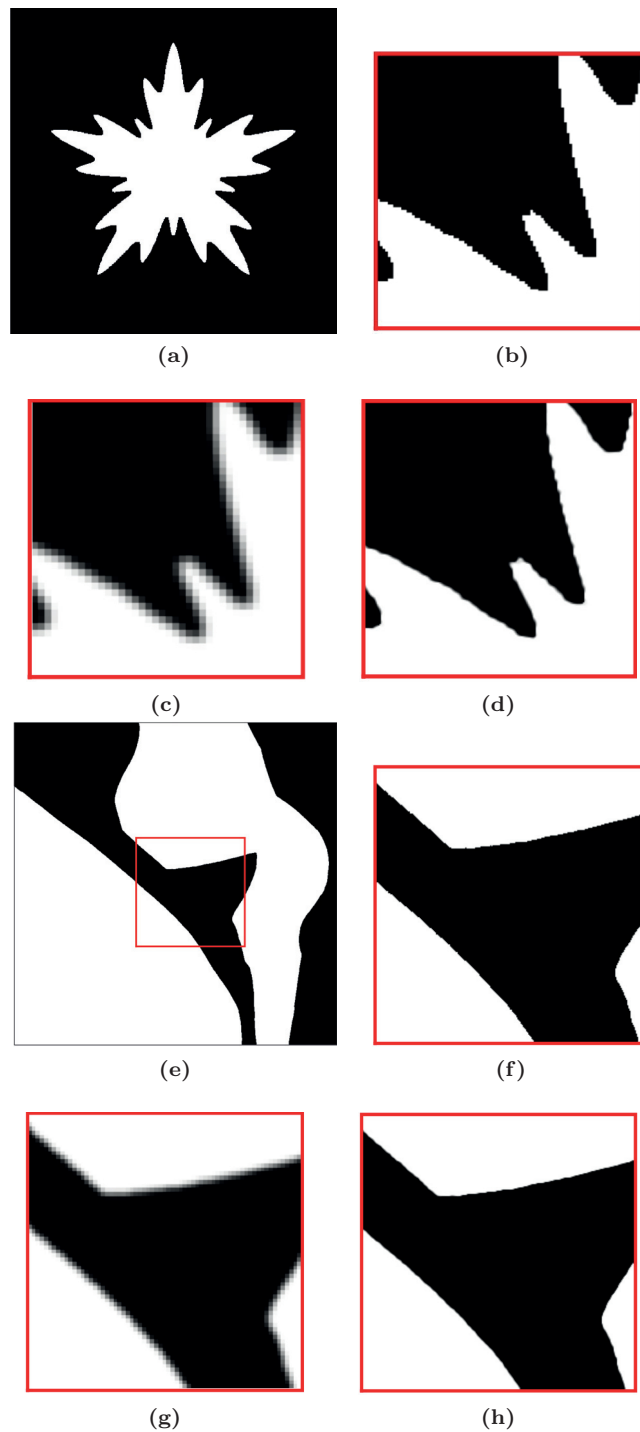


Figure 4.9: Consistent shape reconstruction with the proposed algorithm: Figs. 4.9a and 4.9e display two shapes at the resolution 1000×1000 that will be approximated from 200×200 discrete images, generated with biquadratic B-spline sampling kernels. Figs. 4.9b, 4.9c and 4.9d show the same enlarged sections of the original shape 4.9a, the corresponding discrete image and reconstructed shape, respectively. Figs. 4.9f, 4.9g and 4.9h display the same for the shape in Figure 4.9e.

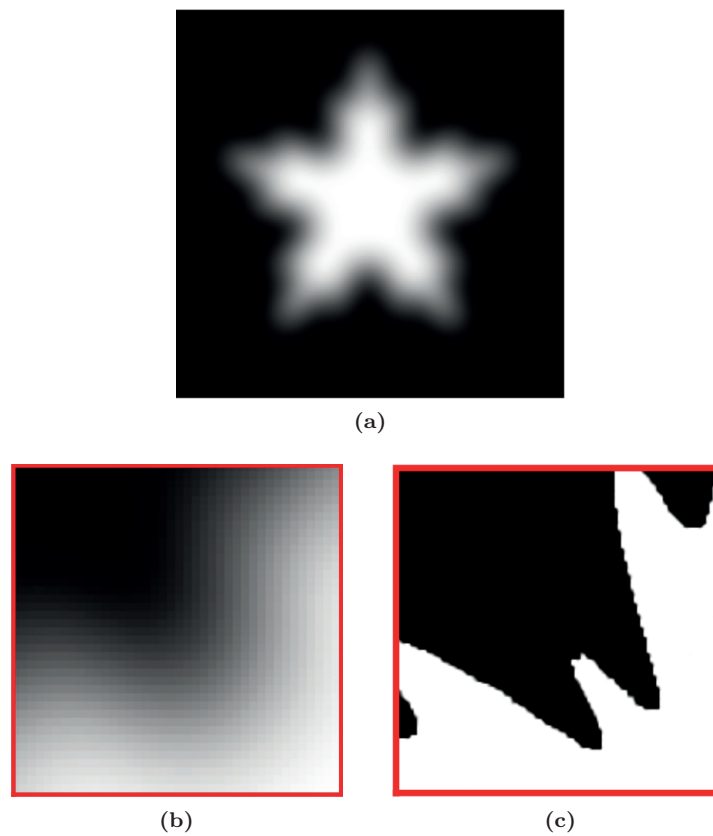


Figure 4.10: Consistent shape reconstruction with the proposed algorithm from highly blurred discrete images: Figure 4.10a shows a 200×200 discrete image corresponding to the shape in Figure 4.9a, when the sampling kernels are shifts of a stretched biquadratic B-spline with an effective support of 40×40 pixels. Figs. 4.10b and 4.10c show the same enlarged sections (as in Figure 4.9b) of the measurement image and reconstructed shape, respectively. The recovered image (without any thresholding) has a PSNR of 33.8096 dB with respect to the original shape and a measurement PSNR of 75.0489 dB.

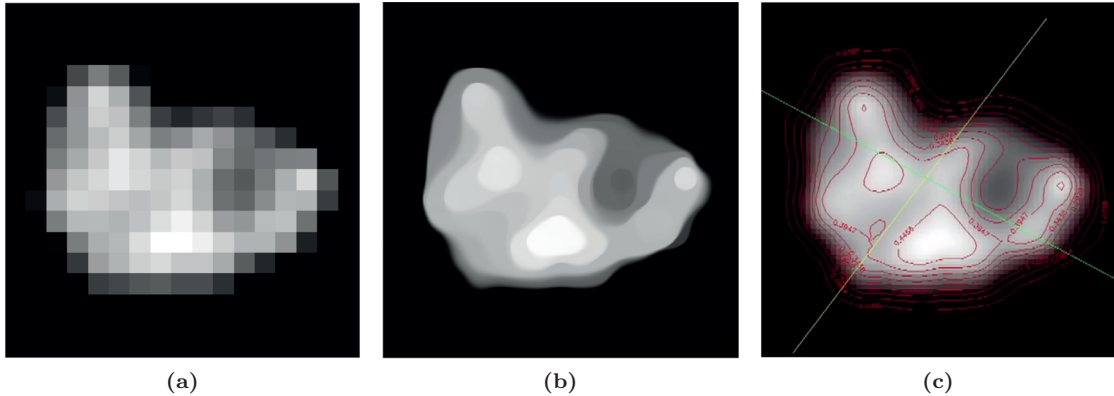


Figure 4.11: Performance of the proposed method in a setting with limited measurements: the measurement image in (a) is taken by the imager of the New Horizons space probe from Hydra. Due to the deficiency of measurements, our reconstruction in (b) is not bilevel; yet it is a good match to the processed image (c) released by NASA.

4.6 Conclusion

In this chapter, we studied the problem of reconstructing a continuous domain shape image from the samples in a gray-scale discrete image. This is essentially equivalent to the interpolation of pixels in a way that generates a binary image. We formulated this problem as a minimization problem where the functional is the continuous domain total variation and the constraints encode the sampling relation between the continuous domain image and the pixels of the discrete image. When the search is over binary images, the minimizers will be shapes with minimum perimeter and smooth boundaries that satisfy the measurements. However, the search over shape images is computationally intractable. We introduced the reducibility condition on the samples of the discrete image and proved that when it is satisfied, extending the search domain to the non-negative-valued images would not omit any of the binary minimizers. The reducibility condition essentially calls for smooth changes in the values of the neighboring pixels. From this perspective, this is an intuitive requirement on the minimum sampling density that is needed for tracking local changes in the shape boundaries.

We conjecture that under the reducibility condition, the convex problem has a unique binary solution. Nevertheless, we introduced a test to verify whether an obtained solution to the convex minimization problem is binary. This test is mainly useful in the numerical calculation of the minimizers where the recovered solutions might not be precisely bilevel due to the numerical precision.

Our approach in this chapter was based on minimization of the total variation, but all the results remain valid if we use a weighted total variation. A carefully designed weighting kernel might locally adjust the recovered shapes and lead to shapes with higher mean curvature.

4.7 Appendix Proof of Lemma 4.1

In the following, we reserve the notation \mathbf{e}_i^n for the canonical basis of \mathbb{R}^n :

$$\mathbf{e}_i^n \triangleq [0, \dots, 0, \underset{i\text{th}}{1}, 0, \dots, 0]^T \in \mathbb{R}^n.$$

We prove the lemma by induction on n . We set the basis of the induction on $n = 1$. It is trivial to check that Condition (1) for $n = 1$ implies the claim in this case. Next, by assuming the validity of Lemma 4.1 for some $n \geq 1$, we demonstrate the validity for $n + 1$.

For the case $K_1^{(n+1)} = \emptyset$, it is not difficult to see that $\boldsymbol{\lambda} = [\frac{1}{n+1}, \dots, \frac{1}{n+1}]^T$ satisfies the requirement. Here, Condition (1) implies that all the inequalities of Condition (3) are in fact equalities. Hence, we focus on $K_1^{(n+1)} \neq \emptyset$. Without loss of generality, we assume that $n + 1 \in K_1^{(n+1)}$. Next, we will try to reduce the $(n + 1)$ -dimensional problem into a similar n -dimensional one with $K_1^{(n)} = K_1^{(n+1)} \setminus \{n + 1\}$ and $K_2^{(n)} = K_2^{(n+1)}$.

According to Condition (2), at $\boldsymbol{\lambda} = \mathbf{e}_{n+1}^{n+1} \in \Delta_{n+1}$ we have that

$$\forall i \in K_1^{(n+1)} \setminus \{n + 1\} : v_i(\mathbf{e}_{n+1}^{n+1}) < d_i.$$

If $K_1^{(n+1)} \setminus \{n + 1\} = \emptyset$, set $\epsilon = \frac{1}{2}$. Otherwise, set $0 < \epsilon \leq \frac{1}{2}$ such that for all $i \in K_1^{(n+1)} \setminus \{n + 1\}$ and all $\boldsymbol{\lambda} \in \Delta_{n+1}$ with $\|\boldsymbol{\lambda} - \mathbf{e}_{n+1}^{n+1}\| < \epsilon$ (i.e., ϵ -neighborhood of \mathbf{e}_{n+1}^{n+1} inside Δ_{n+1}), we have that $v_i(\boldsymbol{\lambda}) < d_i$. The existence of such ϵ follows from the continuity of v (and consequently v_i s). Furthermore, Condition (3) implies $v_i(\boldsymbol{\lambda}) \leq d_i$ for all $i \in K_2^{(n+1)}$ and the same set of $\boldsymbol{\lambda}$ vectors. In summary, we conclude the existence of $0 < \epsilon \leq \frac{1}{2}$ such that

$$\forall 1 \leq i \leq n, \boldsymbol{\lambda} \in \Delta_{n+1}, \|\boldsymbol{\lambda} - \mathbf{e}_{n+1}^{n+1}\| < \epsilon : v_i(\boldsymbol{\lambda}) \leq d_i.$$

By taking Condition (1) into account, we observe that

$$\forall \boldsymbol{\lambda} \in \Delta_{n+1}, \|\boldsymbol{\lambda} - \mathbf{e}_{n+1}^{n+1}\| < \epsilon : v_{n+1}(\boldsymbol{\lambda}) \geq d_{n+1}. \quad (4.9)$$

In words, the value of v_{n+1} in a neighborhood of \mathbf{e}_{n+1}^{n+1} never drops below the desired value d_{n+1} . In contrast, the values of v_{n+1} on the facet of the simplex Δ_{n+1} opposite to \mathbf{e}_{n+1}^{n+1} ($\boldsymbol{\lambda} \in \Delta_{n+1}$, $\lambda_{n+1} = 0$) are strictly below d_{n+1} according to Condition (2). Since v_{n+1} is continuous, by starting from any point on this facet and gradually moving towards \mathbf{e}_{n+1}^{n+1} on the line connecting the two points, v_{n+1} will eventually attain the value d_{n+1} . By considering the points on all such lines that v_{n+1} attains the value d_{n+1} for the first time (when moving away from the facet towards the vertex \mathbf{e}_{n+1}^{n+1}), we shall have a manifold intersecting with all the facets except possibly the studied one. To mathematically represent this manifold we employ the following definition:

$$\forall \mathbf{t} \in \Delta_n : \beta(\mathbf{t}) \triangleq \inf \left\{ \beta \in [0, 1] \mid \forall \gamma, \beta \leq \gamma \leq 1 : \right. \\ \left. v_{n+1}(\gamma t_1, \dots, \gamma t_n, 1 - \gamma) < d_{n+1} \right\}.$$

It is not difficult to apply the continuity of v_{n+1} to conclude the continuity of $\beta(\mathbf{t})$ and the fact that

$$\forall \mathbf{t} \in \Delta_n : v_{n+1}(\beta(\mathbf{t})t_1, \dots, \beta(\mathbf{t})t_n, 1 - \beta(\mathbf{t})) = d_{n+1}. \quad (4.10)$$

Moreover, we invoke (4.9) to demonstrate that $\beta(\mathbf{t}) \geq \frac{\epsilon}{\sqrt{2}}$; *i.e.*, $\beta(\mathbf{t})$ is strictly positive for all $\mathbf{t} \in \Delta_n$.

Now we are ready to reduce the dimension to n . For this purpose, we define the function $u : \Delta_n \mapsto \mathbb{R}^n$ as

$$\begin{aligned} \forall \mathbf{t} = [t_1, \dots, t_n]^T \in \Delta_n : \\ u(\mathbf{t}) \triangleq \begin{bmatrix} v_1(\beta(\mathbf{t})t_1, \dots, \beta(\mathbf{t})t_n, 1 - \beta(\mathbf{t})) \\ \vdots \\ v_n(\beta(\mathbf{t})t_1, \dots, \beta(\mathbf{t})t_n, 1 - \beta(\mathbf{t})) \end{bmatrix} = \begin{bmatrix} u_1(\mathbf{t}) \\ \vdots \\ u_n(\mathbf{t}) \end{bmatrix}. \end{aligned} \quad (4.11)$$

The continuity of $u(\mathbf{t})$ directly follows from the continuity of v and β . To verify Condition (1) for u note that

$$\begin{aligned} & \sum_{i=1}^n \beta(\mathbf{t})t_i v_i(\beta(\mathbf{t})t_1, \dots, \beta(\mathbf{t})t_n, 1 - \beta(\mathbf{t})) \\ & + (1 - \beta(\mathbf{t})) \underbrace{v_{n+1}(\beta(\mathbf{t})t_1, \dots, \beta(\mathbf{t})t_n, 1 - \beta(\mathbf{t}))}_{d_{n+1}} \\ & = \sum_{i=1}^n \beta(\mathbf{t})t_i d_i + (1 - \beta(\mathbf{t}))d_{n+1} \\ & \stackrel{\beta(\mathbf{t}) \neq 0}{\implies} \sum_{i=1}^n t_i \underbrace{v_i(\beta(\mathbf{t})t_1, \dots, \beta(\mathbf{t})t_n, 1 - \beta(\mathbf{t}))}_{u_i(\mathbf{t})} = \sum_{i=1}^n t_i d_i. \end{aligned}$$

Also, let $\mathbf{t} \in \Delta_n$ be such that $t_i = 0$ for some $1 \leq i \leq n$. Recalling the definition of u , we have that

$$u_i(\mathbf{t}) = v_i(\tilde{\boldsymbol{\lambda}}),$$

where

$$\begin{aligned} \tilde{\boldsymbol{\lambda}} &= [\beta(\mathbf{t})t_1, \dots, \beta(\mathbf{t})t_n, 1 - \beta(\mathbf{t})]^T, \\ \sum_{i=1}^{n+1} \tilde{\lambda}_i &= \beta(\mathbf{t}) \underbrace{\sum_{i=1}^n t_i}_{=1} + 1 - \beta(\mathbf{t}) = 1 \implies \tilde{\boldsymbol{\lambda}} \in \Delta_{n+1}. \end{aligned}$$

As $t_i = 0$ results in $\tilde{\lambda}_i = 0$, the Conditions (1) and (3) directly carry over to the functions u_i with $K_1^{(n)} = K_1^{(n+1)} \setminus \{n+1\}$ and $K_2^{(n)} = K_2^{(n+1)}$.

To sum up, u is a continuous function that satisfies Conditions (1)-(3). Therefore, we conclude by the assumption of the induction that there exists $\mathbf{t}^* \in \Delta_n$ such that

$$u(\mathbf{t}^*) = [d_1, \dots, d_n]^T.$$

Finally, by plugging this result into (4.11) and using (4.10), we obtain that

$$v(\beta(\mathbf{t}^*)t_1^*, \dots, \beta(\mathbf{t}^*)t_n^*, 1 - \beta(\mathbf{t}^*)) = [d_1, \dots, d_{n+1}]^T. \quad \blacksquare$$

Chapter 5

Randomized Recovery for Boolean Compressed Sensing

5.1 Introduction

In the previous chapters, we have considered the problem of recovering a continuous-domain binary signal from its measurements. We studied various solutions to this problem, ranging from the compressed sensing standpoint of Section 2 to the convex relaxation approach of Section 4. In this chapter, we study a similar inverse problem in the Boolean algebraic domain: the group testing problem, also known as Boolean compressed sensing (CS).

The group testing problem is about distinguishing a small number of defective items among a large population by grouping subsets of items into a few different pools and detecting defective items based on the results of the collective tests for each pool. Dorfman first introduced the group testing for the blood screening of large groups [50]. The problem then found applications in many other fields such as computational biology (e.g. DNA library screening), quality control, data streams and machine learning [53, 79].

Group testing schemes can have an adaptive or a non-adaptive procedure. In the adaptive schemes, the tests for the next stage depend on the results of previous stages. On the contrary, in the non-adaptive group testing, the structure of tests does not change based on the previous test outcomes (measurements). This allows the parallel implementation of different tests. In this chapter, we only focus on non-adaptive group testing.

Consider a collection of n items participating in m tests and let the binary vector $\mathbf{x} \in \{0, 1\}^n$ indicate the state of the involved items. More specifically, \mathbf{x} contains 1's exactly in places corresponding to the defective items. In typical scenarios, the number k of defective items is very small compared to the number of participating items. Equivalently, \mathbf{x} is a k -sparse vector with $\|\mathbf{x}\|_{\ell_0} = k \ll n$. The goal of the group testing problem is to identify the defective items from the fewest possible measurements.

Let $\mathbf{y} \in \{0, 1\}^m$ represent the outcome of the m measurements and γ_i denote the group of

0. This chapter includes research conducted jointly with Martin Vetterli [62].

items contributing to the i th test. We can formulate the measurements as

$$\mathbf{y}[i] = \bigvee_{j \in \gamma_i} \mathbf{x}[j], \quad 1 \leq i \leq m, \quad (5.1)$$

where \vee is the Boolean OR operator. This equation explains that a measurement is positive if it involves at least one defective item. We can integrate the equations in (5.1) into a single Boolean matrix-vector product

$$\mathbf{y} = \mathbf{\Gamma} \vee \mathbf{x}, \quad (5.2)$$

in which $\mathbf{\Gamma}_{m \times n}$ is a Boolean matrix with rows and columns representing different pools and items, respectively: $\mathbf{\Gamma}_{i,j} = 1$ shows that the item j is part of the pool i . Note that \vee in this equation reminds that the summation is replaced by the OR operation.

In addition to the noiseless scenario, we may also consider the noisy-variant of the group testing problem, in which the measurements may differ from the true results. We can model the noisy measurements as

$$\mathbf{y} = \mathbf{\Gamma} \vee \mathbf{x} \oplus \mathbf{n}, \quad (5.3)$$

where \oplus denotes XOR operation and \mathbf{n} represents the Bernoulli distributed noise vector. In this case, the estimation of defective items is more challenging and requires more measurements.

The formulations of the group testing problem in equations (5.2) and (5.3) are very similar to the well-known problem of compressed sensing (CS) [28, 29, 49], where the goal is to estimate a sparse vector from a small number of linear measurements. The major differences are that the former is under a Boolean algebra and involves Bernoulli distributed noise while the latter involves operations in the field of real numbers with Gaussian noise. Hence, the group testing problem is sometimes referred to as Boolean compressed sensing [11, 65]. Moreover, a number of solutions to this problem have parallels in CS; for example, the combinatorial basis pursuit (CBP) and combinatorial orthogonal matching pursuit (COMP) algorithms in [37].

It was recently proposed to use relaxed linear programming (LP) to solve the group testing problem [78]. The LP algorithm of [78] bypasses the binary constraints and solves a linear problem. Then, the outcome undergoes rounding to recover a binary vector. Unfortunately, the final result is often less sparse than the original vector. In this chapter, we replace the rounding procedure with a random assignment of 1's to the most likely defective entries; the probabilities of the random assignments are determined by the solution of the linear program. We show that the proposed algorithm considerably improves the success rate with only a slight increase in computational cost. In this chapter, we only consider the noiseless measurement scenario. The more involved case of noisy measurements is left as future work.

This chapter is organized as follows. In Section 5.2, we review the bounds on the number of measurements that guarantee exact signal reconstruction in group testing. In Section 5.3, we review the LP algorithm of [78] for the noiseless and noisy measurements. We present our randomized algorithm in Section 5.4, accompanied with an analysis of the algorithm. The performance comparison of the ordinary and randomized algorithms is presented in Section 5.5. Finally, we conclude in Section 5.6.

5.2 CS and Group Testing: Recovery Bounds

In CS, the goal is to recover a sparse vector $\mathbf{x}^* \in \mathbb{R}^n$ from a small number $m \ll n$ of linear measurements $\mathbf{y} = \mathbf{A}\mathbf{x}^*$. Combinatorial solutions to this problem solve the equation

$$\begin{aligned} \min_{\mathbf{x} \in \mathbb{R}^n} \|\mathbf{x}\|_{\ell_0} \\ \text{s.t. } \mathbf{y} = \mathbf{A}\mathbf{x}, \end{aligned} \quad (5.4)$$

where $\|\mathbf{x}\|_{\ell_0}$ is a pseudo-norm that counts the nonzero entries of \mathbf{x} . Another possible solution for CS can be obtained by substituting the non-convex ℓ_0 norm in (5.4) with the convex ℓ_1 norm. This results in the *basis pursuit* algorithm

$$\begin{aligned} \min_{\mathbf{x} \in \mathbb{R}^n} \|\mathbf{x}\|_{\ell_1} \\ \text{s.t. } \mathbf{y} = \mathbf{A}\mathbf{x}, \end{aligned} \quad (5.5)$$

which can be solved efficiently with linear programming solvers. It is shown that if the sensing matrix \mathbf{A} has random independent and identically distributed (*i.i.d.*) Gaussian entries with $m = O(k \log(n/k))$ measurements, both equations in (5.4) and (5.5) recover the exact solution $\mathbf{x} = \mathbf{x}^*$. The reason is that these matrices satisfy the so-called *Restricted Isometry Property* (RIP), which ensures that different k -sparse vectors are mapped to different measurements.

In group testing, there are two types of matrices that ensure the identifiability of k -sparse binary vectors: *k-separating* and *k-disjunct* matrices [53, 54].

Definition 5.1

A binary matrix $\mathbf{\Gamma}$ is *k-separating* if Boolean sums of sets of k columns are all distinct.

Matrices with *k-separating* property ensure that different k -sparse vectors produce distinct measurements and therefore, they guarantee recovery of a unique k -sparse solution. A stronger notion is the *k-disjunct* property.

Definition 5.2

A binary matrix is called *k-disjunct* if the Boolean sum of any k columns does not contain any other column.

Matrices that satisfy this property are desirable not only because they ensure identifiability but they also lead to efficient decoding algorithms. Combinatorial constructions of *k-disjunct* matrices were extensively developed in [54, 58].

A different approach to the group testing problem is based on probabilistic methods. In [54, 55], the authors establish upper and lower bounds on the number of rows m for a matrix to be *k-disjunct*. They show that in the noiseless scenario, m should scale as $O\left(\frac{k^2 \log n}{\log k}\right)$ for exact recovery with worst-case input. Also, a study of the noisy counterpart of group testing problem in equation (5.3) revealed that the number of measurements must scale as $O\left(\frac{k^2 \log n}{(1-q) \log k}\right)$ for a worst-case error criterion, when the noise distribution is Bernoulli(q) [11].

5.3 Recovery Algorithms

Several algorithms have been proposed for the recovery of defective items from measurements in the group testing problem, most of which have parallels in CS. Examples are *separate testing of inputs* (STI) algorithm [83], *loopy belief propagation* (LBP) decoder [97], CBP and COMP algorithms [37], and the LP relaxation technique [78]. The last scheme has a simple structure, yet it is more effective in recovering the exact solution compared to the other schemes [78]. This algorithm parallels the LP relaxation of basis pursuit in CS.

In this section, we review the LP relaxation solution for the noiseless and noisy measurements. First, we introduce some notations. Let \mathcal{I} and \mathcal{J} denote the index of positive and negative measurements, respectively; *i.e.*,

$$\mathcal{I} = \{i \mid \mathbf{y}[i] = 1\}, \quad \mathcal{J} = \{1, \dots, m\} \setminus \mathcal{I}.$$

Also, let $\mathbf{\Gamma}_{\mathcal{I}}$ and $\mathbf{\Gamma}_{\mathcal{J}}$ denote the restriction of $\mathbf{\Gamma}$ to the rows indexed by \mathcal{I} and \mathcal{J} , respectively. The LP relaxation technique is based on the observation that any boolean vector that satisfies $\mathbf{y} = \mathbf{\Gamma} \vee \mathbf{x}$ also complies with the linear equations $\mathbf{\Gamma}_{\mathcal{I}}\mathbf{x} \geq \mathbf{y}_{\mathcal{I}}$ and $\mathbf{\Gamma}_{\mathcal{J}}\mathbf{x} = \mathbf{0}$. This leads to the following Boolean linear programming formulation of the group testing problem

$$\begin{aligned} & \min \|\mathbf{x}\|_{\ell_1} & (5.6) \\ \text{s.t. } & \mathbf{x} \in \{0, 1\}^n, \quad \mathbf{\Gamma}_{\mathcal{I}}\mathbf{x} \geq \mathbf{y}_{\mathcal{I}}, \quad \mathbf{\Gamma}_{\mathcal{J}}\mathbf{x} = \mathbf{0}, \end{aligned}$$

where we used the equality $\|\mathbf{x}\|_{\ell_0} = \|\mathbf{x}\|_{\ell_1}$ for Boolean vectors \mathbf{x} . By relaxing the binary constraint on \mathbf{x} , we obtain a tractable linear program

$$\begin{aligned} & \min \|\mathbf{x}\|_{\ell_1} & (5.7) \\ \text{s.t. } & 0 \leq \mathbf{x} \leq 1, \quad \mathbf{\Gamma}_{\mathcal{I}}\mathbf{x} \geq \mathbf{y}_{\mathcal{I}}, \quad \mathbf{\Gamma}_{\mathcal{J}}\mathbf{x} = \mathbf{0}. \end{aligned}$$

In case of non-integral entries $\mathbf{x}[j]$ in the solution, we set them to 1.

In the noisy scenario, we might not find a boolean vector that satisfies the measurements $\mathbf{y} = \mathbf{\Gamma} \vee \mathbf{x}$. In this case, we can use a slack vector $\boldsymbol{\xi} \in \mathbb{R}^m$ to obtain a LP relaxation of group testing in the the presence of noise:

$$\begin{aligned} & \min \|\mathbf{x}\|_{\ell_1} + \alpha \|\boldsymbol{\xi}\|_{\ell_1} \\ \text{s.t. } & 0 \leq \mathbf{x} \leq 1, \quad 0 \leq \boldsymbol{\xi}, \quad \boldsymbol{\xi}_{\mathcal{I}} \leq 1, \\ & \mathbf{\Gamma}_{\mathcal{I}}\mathbf{x} + \boldsymbol{\xi}_{\mathcal{I}} \geq \mathbf{y}_{\mathcal{I}}, \quad \mathbf{\Gamma}_{\mathcal{J}}\mathbf{x} = \boldsymbol{\xi}_{\mathcal{J}}. \end{aligned}$$

5.4 Randomized Recovery

The LP algorithm in equation (5.7) provides the optimal solution $\mathbf{x} = \mathbf{x}^*$ if \mathbf{x}^* is k -sparse and the matrix $\mathbf{\Gamma}$ is k -disjunct [78]. Otherwise, it may yield a non-integral solution with minimum ℓ_1 norm and a large number of non-zero entries. Rounding the non-integral entries to 1 gives a solution with a large number of defective items.

In this section, we propose a randomized LP algorithm (RLP) based on the LP relaxation in (5.7). The new algorithm provides arbitrary small measurement error probability and sparser solutions compared to the LP algorithm described above.

Algorithm 5.1 Randomized linear programming for noiseless measurements

Input: \mathbf{y} , Γ , ϵ .**Output:** $\hat{\mathbf{x}} \in \{0, 1\}^n$ such that $\mathbf{y} = \Gamma \vee \hat{\mathbf{x}}$ (with probability $\geq 1 - \epsilon$).

- 1: **Initialization:**
 - 2: $\hat{\mathbf{x}} \leftarrow \mathbf{0}$, $\mathcal{I} = \{i \mid \mathbf{y}[i] = 1\}$, $\mathcal{J} = \{i \mid \mathbf{y}[i] = 0\}$;
 - 3: Set \mathbf{x}_p as the minimizer of (5.7);
 - 4: **for** $\ell := 1$ **to** $\lceil \log \frac{|\mathcal{I}|}{\epsilon} \rceil$ **do**
 - 5: Generate a vector \mathbf{x}_ℓ according to the distribution $\mathbf{x}_\ell[i] \sim \text{Bernoulli}(\mathbf{x}_p[i])$, $i = 1, \dots, n$;
 - 6: $\hat{\mathbf{x}} \leftarrow \hat{\mathbf{x}} \vee \mathbf{x}_\ell$;
 - 7: **if** $(\Gamma \vee \hat{\mathbf{x}} = \mathbf{y})$ **then**
 - 8: Stop;
 - 9: **end if**
 - 10: **end for**=0
-

Let $0 \leq \mathbf{x}_p \leq 1$ denote the fractional minimizer of (5.7). Instead of rounding the entries of \mathbf{x}_p , we consider \mathbf{x}_p as a set of probabilities which we use to generate a Boolean vector \mathbf{x}_ℓ according to the distribution

$$\mathbf{x}_\ell[i] \sim \text{Bernoulli}(\mathbf{x}_p[i]), \quad i = 1, \dots, n.$$

Then, we set $\hat{\mathbf{x}} = \mathbf{x}_\ell$ and check whether the equality $\Gamma \vee \hat{\mathbf{x}} = \mathbf{y}$ holds. If not, we take a new realization of \mathbf{x}_ℓ and we set $\hat{\mathbf{x}} = \hat{\mathbf{x}} \vee \mathbf{x}_\ell$. We repeat this procedure until $\hat{\mathbf{x}}$ satisfies the measurements or we reach a certain number of iterations. Algorithm 5.1 summarizes the proposed recovery method.

In the following, we prove that this algorithm recovers a Boolean vector that satisfies the measurements with arbitrarily small error probability. Let J_{LP} represent the minimum value of (5.7). Also, let $\hat{\mathbf{x}}$ indicate the output of Algorithm 5.1 after 1 iteration. Then,

$$P(\hat{\mathbf{x}}[i] = 1) = \mathbf{x}_p[i], \quad P(\hat{\mathbf{x}}[i] = 0) = 1 - \mathbf{x}_p[i]$$

and

$$\mathbb{E}(\|\hat{\mathbf{x}}\|_{\ell_0}) = \sum_{i=1}^n 1 \cdot \mathbf{x}_p[i] = J_{LP} \leq J, \quad (5.8)$$

where \mathbb{E} is the expected value and J is the optimal value of the Boolean group testing problem in (5.6). Equation (5.8) shows that the expected number of defective items in $\hat{\mathbf{x}}$ is J_{LP} . Therefore, the average number of defective items of the output in Algorithm 5.1 after $c = \lceil \log \frac{|\mathcal{I}|}{\epsilon} \rceil$ iterations is not larger than cJ_{LP} .

Proposition 5.1

The output vector $\hat{\mathbf{x}}$ of Algorithm 5.1 after $c = \lceil \log \frac{|\mathcal{I}|}{\epsilon} \rceil$ iterations coincides with the measurements \mathbf{y} with a probability greater than $1 - \epsilon$, i.e.,

$$P(\mathbf{y} = \Gamma \vee \hat{\mathbf{x}}) > 1 - \epsilon.$$

Proof The constraint $\mathbf{\Gamma}_{\mathcal{I}}\mathbf{x} = \mathbf{0}$ in (5.7) implies that the entries of \mathbf{x}_p corresponding to the items that contribute to the pools with negative (or zero) test outcomes are set to 0. This ensures the same items in $\hat{\mathbf{x}}$ are set to 0, or equivalently, the vector of test outcomes \mathbf{y} contains the measurements associated to $\hat{\mathbf{x}}$, *i.e.*,

$$\mathbf{y} \geq \mathbf{\Gamma} \vee \hat{\mathbf{x}}.$$

Therefore, we only need to calculate the probability of $\mathbf{\Gamma}_{\mathcal{I}} \vee \hat{\mathbf{x}} = \mathbf{y}_{\mathcal{I}}$ or equivalently, $\mathbf{\Gamma}_{\mathcal{I}}\hat{\mathbf{x}} \geq \mathbf{y}_{\mathcal{I}}$.

Let $i \in \mathcal{I}$ and $|\gamma_i|$ denote the number of items contributing to the i th pool with a positive outcome. If $\hat{\mathbf{x}}$ denotes the output of Algorithm 5.1 after 1 iteration, we have

$$P(\mathbf{\Gamma}_i\hat{\mathbf{x}} < \mathbf{y}[i]) = P(\mathbf{\Gamma}_i\hat{\mathbf{x}} = 0) = \prod_{j \in \gamma_i} (1 - \mathbf{x}_p[j]).$$

We can take the logarithm of the right hand side and apply Jensen's inequality to the concave function $\log(1 - x)$ to get

$$\begin{aligned} \sum_{j \in \gamma_i} \frac{1}{|\gamma_i|} \log(1 - \mathbf{x}_p[j]) &\leq \log\left(1 - \frac{\sum_{j \in \gamma_i} \mathbf{x}_p[j]}{|\gamma_i|}\right) \\ \implies \prod_{j \in \gamma_i} (1 - \mathbf{x}_p[j]) &\stackrel{(a)}{\leq} \left(1 - \frac{1}{|\gamma_i|}\right)^{|\gamma_i|} \leq \frac{1}{e}, \end{aligned}$$

where (a) results from the fact that $\sum_{j \in \gamma_i} \mathbf{x}_p[j] = \sum_{j=1}^n \mathbf{\Gamma}_{ij} \mathbf{x}_p[j] \geq 1$. Therefore, after c iterations, we have

$$P(\mathbf{\Gamma}_i\hat{\mathbf{x}} = 0) \leq \left(\frac{1}{e}\right)^c.$$

Finally, from the union bound, we get

$$P(\exists i \in \mathcal{I} : \mathbf{\Gamma}_i\hat{\mathbf{x}} = 0) \leq |\mathcal{I}| \cdot \left(\frac{1}{e}\right)^{\left\lceil \log \frac{|\mathcal{I}|}{\epsilon} \right\rceil} \leq \epsilon,$$

which proves that $P(\mathbf{y} = \mathbf{\Gamma} \vee \hat{\mathbf{x}}) > 1 - \epsilon$. ■

The LP algorithm in [78] can be regarded as a special case of our algorithm with infinite iterations so that every $\hat{\mathbf{x}}[i]$ that has a probability $\mathbf{x}_p[i]$ larger than 0 is set to 1. Therefore, it generates a less sparse binary vector compared to the output of Algorithm 5.1. We recall that when \mathbf{y} corresponds to a k -sparse vector \mathbf{x}^* and $\mathbf{\Gamma}$ is k -disjunct, equation (5.7) has a binary solution and therefore, both algorithms recover the optimal solution $\mathbf{x} = \mathbf{x}^*$.

Link to the set covering problem

A related problem to the Boolean CS is the classical set covering problem. Given a set of elements $U = \{1, \dots, m\}$ (called a universe) and n sets whose union comprises the universe, the set covering problem is to identify the smallest number of sets whose union still contains all elements of the universe. The Boolean CS problem can be modeled as set covering problem by considering $\mathbf{y}_{\mathcal{I}}$ as the universe and columns of $\mathbf{\Gamma}_{\mathcal{I}}$ as different sets. In this regard, the randomized LP method of this section parallels the solutions to the set covering problem [95].

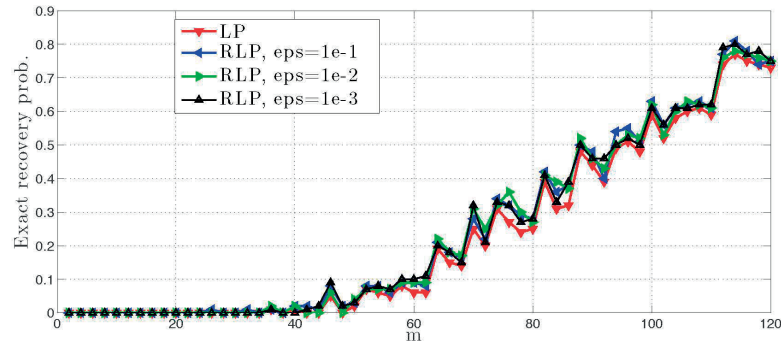


Figure 5.1: Probability of exact signal reconstruction in LP and RLP algorithms for $n = 150$, $k = 4$ and noiseless measurements. Averages over 100 trials.

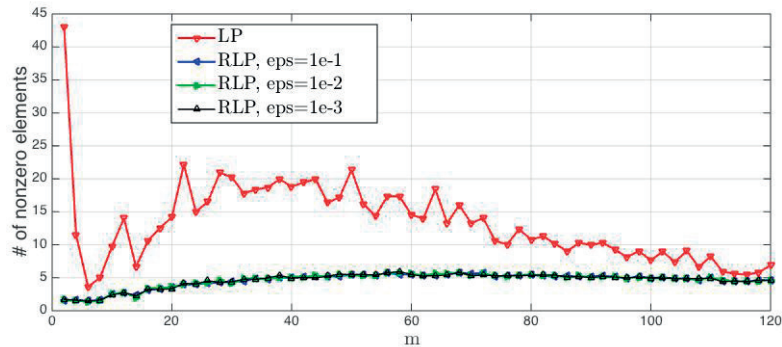


Figure 5.2: Sparsity of the recovered signals in LP and RLP algorithms for $n = 150$, $k = 4$ and noiseless measurements. Averages over 100 trials.

5.5 Simulation Results

In [78], the authors compare the performance of LP algorithm with a number of algorithms such as CBP, COMP, LBP and STI. This comparison reveals that LP outperforms the other algorithms in terms of the probability of exact recovery. We now present experimental results comparing our randomized algorithm with LP. For better comparison, we follow the same experimental setup as in [78].

In the first experiment, we study the probability of exact signal recovery and sparsity of recovered signals in 100 random trials for different number m of measurements. We consider Boolean vectors $\mathbf{x} \in \{0, 1\}^n$ for $n = 150$ and 4 nonzero entries. For each value of $m \in \{1, \dots, 120\}$, we generate a Boolean sensing matrix with 50% of its entries set to 1 and then, we calculate the (noiseless) measurements. We compute the LP solutions as well as the results of RLP for three different error probabilities $\epsilon = 0.1, 0.01$ and 0.001 . The results are shown in Figures 5.1 and 5.2. The plots in these figures show that our RLP algorithm outperforms LP in terms of both the sparsity and the exact reconstruction probability.

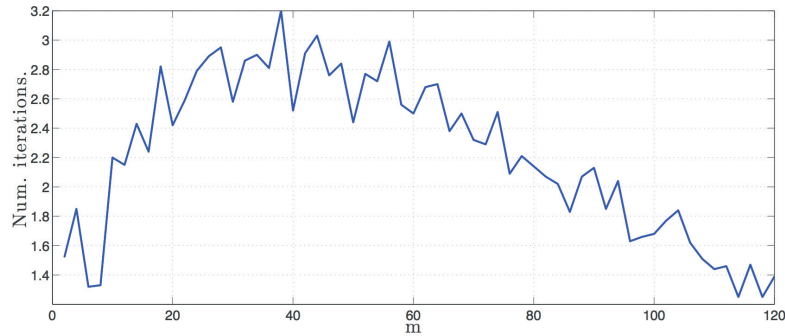


Figure 5.3: Computational complexity of RLP: the average number of iterations required for generating a vector $\hat{\mathbf{x}}$ that coincides with measurements \mathbf{y} . Averages over 100 trials for $n = 150$ and $k = 4$.

In the next experiment, we examine the computational complexity of RLP. For this purpose, we run RLP until the recovered signal $\hat{\mathbf{x}}$ produces the same measurement vector \mathbf{y} . The average number of iterations is depicted in Figure 5.3 as a function of m , for the same setup as in the previous experiment. This plot shows that the randomized LP algorithm requires only a small number of iterations. Note that each iteration consists of generating a random Bernoulli vector \mathbf{x}_ℓ and the Boolean operations involved in $\mathbf{\Gamma} \vee \hat{\mathbf{x}}$ and $\hat{\mathbf{x}} \vee \mathbf{x}_\ell$. These results show that RLP achieves a considerable performance improvement over LP with a slight increase in computational complexity.

5.6 Conclusion

We considered the problem of Boolean CS, where the unknown variables $\mathbf{x}[i]$ are constrained to be in $\{0, 1\}$. Although the measurement process is linear with respect to $\mathbf{x}[i]$, due to the binary constraints, the linear program is NP hard [78]. We applied the relaxation $\mathbf{x}[i] \in [0, 1]$ in the linear program and obtained fractional solutions. To map the fractional values onto binary values, instead of the common rounding techniques, we considered a randomized approach; i.e., each value is randomly mapped to 0 or 1, with a probability determined by the fractional value. The simulation results indicate that the randomized algorithm considerably outperforms the previous methods with only a slight increase in computational cost.

Chapter 6

Conclusion and Future Work

یک چند به کودکی باستاد شدیم یک چند ز استادی خود شاد شدیم
پایان سخن شنو که مارا چه رسید از خاک در آمدیم و بر خاک شدیم

In childhood we strove to go to school
Our turn to teach, joyous as a rule
The end of story is sad and cruel
From dust we came, and gone with winds cool

Omar Khayyam

A large part of this thesis was developed related to the problem of recovering continuous-domain shape images from their samples. We considered a sampling model reflecting the physics of imaging devices such as digital cameras with some degree of simplification. In this linear model, the image pixels and the involved point spread function are represented by the samples and the sampling kernels, respectively. Here, we briefly review the results and highlight some of remaining challenges as potential future works.

1. **Signal Approximation:** Samples of a signal can be regarded as its coefficients in a domain spanned by the sampling kernels. When the sampling domain yields a poor signal approximation, it might be helpful to switch the representation domain to the ones that approximate the target class of signals more effectively. We studied this problem in the recent frameworks of generalized sampling and infinite-dimensional compressed sensing. We observed that the gain of generalized sampling, due to its linearity, is limited to the linear approximation rates of the representation domain; hence, it is incapable of generating good shape approximations from a limited number of samples. The infinite-dimensional compressed sensing is a more promising approach for recovering efficient signal approximations in a domain. But, we saw that a main ingredient in this approach is (uniform or structured) random sampling that is not in harmony with our sampling model.
2. **A Robust Sampling Scheme for Shapes with Algebraic Boundaries:** We proposed a sampling and reconstruction scheme for shape images with boundaries that form a subset of an algebraic curve with an implicit bivariate polynomial. We showed that the image parameters satisfy a set of linear annihilation equations with the coefficients being the image

moments. To form these equations, we need to extract the moments from pixel values, which in turn requires the sampling kernel to exactly reproduce polynomials. Further, the process of converting pixels into moments is very sensitive to noise. To combat these two limitations, we introduced positive and decaying weight functions within the definition of moments (generalized moments). Indeed, the decay of the weight function improves the stability of the method against noise. We also removed the constraint on the sampling kernel by optimizing over the choice of the weight function. Besides, we reinforced the resulting reconstruction technique by applying sign and measurement consistency.

In future work, we should consider the following problem:

- In this work, we introduced a fast decaying weight function g to prevent the blowup of the elements of the moment matrix \mathbf{M} and improve the stability of the algorithm. Our approach was heuristic in the sense that we did not analyze how preventing the blowup simply causes stability. A theorem stating how the error in the measurements would impact the conditioning number of the matrix \mathbf{M} and the reconstruction would be enlightening.
- Among the interesting problems that are not addressed in this thesis and deserves future investigation is the detection of occluded shapes. This problem arises in many applications such as quality control and medical imaging. Oftentimes, the desired objects have simple structures such as circles or ellipses and can be simply modeled with low-degree polynomials. In a noiseless setting, our proposed algorithm succeeds in detecting all the objects even the occluded ones. In a noisy setting, however, the algorithm tries to merge the overlapping objects into a single shape with a higher polynomial degree. By restricting the output of the algorithm to be decomposable into low-order polynomials or follow a structure, one might be able to extend this technique to noisy cases.

3. Measurement-Consistent Shape Reconstruction: Parametric image models with a few parameters admit limited shape geometries. Also, increasing the number of parameters usually complicates the sampling and reconstruction schemes. To address sampling of shapes with arbitrary geometries, we formulated the reconstruction technique by minimizing the shape perimeter over the set of consistent binary images. We introduced a sufficient requirement, called reducibility, on the pixel values that allowed us to transform the problem into minimizing the total variation over consistent non-negative-valued image. We also illustrated that the reducibility condition is an intuitive requirement on the minimum sampling density.

In future work, we should consider the following problems:

- We established the equivalence between the non-convex problem and its convex relaxation by showing that under the reducibility condition, we can merge the multiple constraints into a single one. This way, we reduced the problem to the well-known Cheeger problem and we exploited the existing results there. We might get a more relaxed condition on the pixel values if we bypass the link to the single-constraint problem and directly prove the results for the multiple-constraints setting.
- The reducibility requirement on the pixel values guarantees that the relaxed minimization problem has a binary solution: the consistent shape image with minimum

perimeter. However, this might not be the exact solution. Investigating requirements on the pixels that guarantee an exact solution would lead to an actual sampling theory for shape images.

4. **Randomized Recovery for Boolean Compressed Sensing:** We further studied a relevant problem in the Boolean algebra: the group testing problem, also known as Boolean Compressed sensing. We revisited a linear programming formulation of the problem that is based on relaxing the Boolean constraint on the variables accompanied by a rounding of the basis pursuit solution. We replaced the rounding step by a random assignment of 0's and 1's to the variables, with a probability determined by the fractional solution of the basis pursuit problem. We showed that the randomized algorithm outperforms the previous methods with only a slight increase in the computational cost. In this thesis, we only studied this problem in a noiseless setting. Extension of the randomized algorithm to the noisy Boolean compressed sensing might be considered as future work.

Our final comment is regarding our model of shape images. In this thesis, we only considered shape images with exactly two intensity values. However, many images in the real world are just approximately binary and it would be very useful to extend the algorithms of this thesis to this broader class of images. A potential result of this extension would be the segmentation of non-binary continuous-domain images from their samples.

Bibliography

- [1] B. Adcock and A. C. Hansen, “Sharp bounds, optimality and a geometric interpretation for generalized sampling in Hilbert spaces,” *Preprint*, 2011.
- [2] —, “A generalized sampling theorem for stable reconstruction in arbitrary bases,” *J. Fourier Anal. Appl.*, vol. 18, no. 4, pp. 685–716, Aug. 2012.
- [3] —, “Stable reconstruction in Hilbert spaces and the resolution of the Gibbs phenomenon,” *Appl. Comput. Harmon. Anal.*, vol. 32, no. 3, pp. 357–388, 2012.
- [4] —, “Generalized sampling and infinite-dimensional compressed sensing,” *Found. Comput. Math.*, pp. 1–61, Aug. 2015, doi 10.1007/s10208-015-9276-6.
- [5] B. Adcock, A. C. Hansen, E. Herrholz, and G. Teschke, “Generalized sampling: extension to frames and inverse and ill-posed problems,” *Inverse Probl.*, vol. 29, no. 1, p. 015008, Jan. 2013.
- [6] B. Adcock, A. C. Hansen, G. Kutyniok, and J. Ma, “Linear stable sampling rate: optimality of 2D wavelet reconstructions from Fourier measurements,” *SIAM J. Math. Anal.*, vol. 47, no. 2, pp. 1196–1233, 2015.
- [7] B. Adcock, A. C. Hansen, and C. Poon, “On optimal wavelet reconstructions from Fourier samples: linearity and universality of the stable sampling rate,” *Appl. Comput. Harmon. Anal.*, vol. 36, no. 3, pp. 387–415, 2014.
- [8] B. Adcock, A. C. Hansen, C. Poon, and B. Roman, “Breaking the coherence barrier: asymptotic incoherence and asymptotic sparsity in compressed sensing,” *Preprint*, 2013.
- [9] —, “Breaking the coherence barrier: a new theory for compressed sensing,” *arXiv preprint arXiv:1302.0561v4*, Jun. 2014.
- [10] E. Arbarello, M. Cornalba, and P. Griffiths, *Geometry of Algebraic Curves: Volume II with a Contribution by Joseph Daniel Harris*. Springer Science & Business Media, 2011, vol. 268.
- [11] G. K. Atia and V. Saligrama, “Boolean compressed sensing and noisy group testing,” *IEEE Trans. Inf. Theory*, vol. 58, no. 3, pp. 1880–1901, Mar. 2012.
- [12] L. Baboulaz and P. Dragotti, “Exact feature extraction using finite rate of innovation principles with an application to image super-resolution,” *IEEE Trans. Image Process.*, vol. 18, no. 2, pp. 281–298, Jan. 2009.

-
- [13] R. H. Bamberger and M. J. Smith, "A filter bank for the directional decomposition of images: theory and design," *IEEE Trans. Signal Process.*, vol. 40, no. 4, pp. 882–893, Apr. 1992.
- [14] J. Berent, P. L. Dragotti, and T. Blu, "Sampling piecewise sinusoidal signals with finite rate of innovation methods," *IEEE Trans. Signal Process.*, vol. 58, no. 2, pp. 613–625, Feb. 2010.
- [15] T. Blu, P. L. Dragotti, M. Vetterli, P. Marziliano, and L. Coulot, "Sparse sampling of signal innovations," *IEEE Signal Process. Mag.*, vol. 25, no. 2, pp. 31–40, Mar. 2008.
- [16] L. M. Bregman, "The relaxation method of finding the common point of convex sets and its application to the solution of problems in convex programming," *USSR comp. math. math. phys.*, vol. 7, no. 3, pp. 200–217, 1967.
- [17] X. Bresson, S. Esdoglu, P. Vandergheynst, J. P. Thiran, and S. Osher, "Fast global minimization of the active contour/snake model," *J. Math. Imaging Vis.*, vol. 28, no. 2, pp. 151–167, 2007.
- [18] X. Bresson, P. Vandergheynst, and J. P. Thiran, "A variational model for object segmentation using boundary information and shape prior derived by Mumford-Shah functional," *Int. J. Comput. Vis.*, vol. 68, no. 2, pp. 145–162, 2006.
- [19] P. Brigger, J. Hoeg, and M. Unser, "B-spline snakes: A flexible tool for parametric contour detection," *IEEE Trans. Signal Process.*, vol. 9, no. 9, pp. 1484–1496, Sep. 2000.
- [20] P. J. Burt and E. H. Adelson, "The Laplacian pyramid as a compact image code," *IEEE Trans. Commun.*, vol. COM-31, no. 4, pp. 532–540, Apr. 1983.
- [21] G. Buttazzo, G. Carlier, and M. Comte, "On the selection of maximal Cheeger sets," *Differ. Integral Equ.*, vol. 20, no. 9, pp. 991–1004, Jun. 2007.
- [22] J. A. Cadzow, "Signal enhancement – a composite property mapping algorithm," *IEEE Trans. Acoust. Speech, Signal Process.*, vol. 36, no. 1, pp. 49–62, Jan. 1988.
- [23] E. Candès, "Ridgelets: Theory and Applications," Ph.D. dissertation, Department of Statistics, Stanford University, 1998.
- [24] E. Candès and D. Donoho, "Ridgelets: the key to higher-dimensional intermittency?" *Phil. Trans. R. Soc. Lond. A*, vol. 357, no. 1760, pp. 2495–2509, Sep. 1999.
- [25] —, "Curvelets, multiresolution representation, and scaling laws," in Proc. *Int. Symposium on Opt. Sci. Technol. SPIE*, pp. 1–12. International Society for Optics and Photonics, 2000.
- [26] —, "New tight frames of curvelets and optimal representations of objects with piecewise c^2 singularities," *Comm. Pure Appl. Math.*, vol. 57, no. 2, pp. 219–266, Feb. 2004.
- [27] E. Candès and J. Romberg, "Sparsity and incoherence in compressive sampling," *Inverse Probl.*, vol. 23, no. 3, pp. 969–985, 2007.

-
- [28] E. Candès, J. Romberg, and T. Tao, “Robust uncertainty principles: exact signal reconstruction from highly incomplete frequency information,” *IEEE Trans. Info. Theory*, vol. 52, no. 2, pp. 489–509, Feb. 2006.
- [29] E. Candès and T. Tao, “Near optimal signal recovery from random projections: universal encoding strategies,” *IEEE Trans. Info Theory*, vol. 52, no. 12, pp. 5406–5425, Dec. 2006.
- [30] G. Carlier and M. Comte, “On a weighted total variation minimization problem,” *J. Func. Anal.*, vol. 250, no. 1, pp. 214–226, Sep. 2007.
- [31] G. Carlier, M. Comte, and G. Peyré, “Approximation of maximal Cheeger sets by projection,” *M2AN Math. Model. Numer. Anal.*, vol. 43, no. 1, pp. 139–150, Jan. 2009.
- [32] J. L. Carter, “Dual methods for Total Variation-Based Image Restoration,” Ph.D. dissertation, University of California Los Angeles, 2001.
- [33] V. Caselles, R. Kimmel, and G. Sapiro, “Geodesic active contours,” *Int. J. Comput. Vis.*, vol. 22, no. 1, pp. 61–79, Feb. 1997.
- [34] A. Chambolle, “An algorithm for total variation minimization and applications,” *J. Math. Imaging Vis.*, vol. 20, no. 1-2, pp. 89–97, 2004.
- [35] —, “Total variation minimization and a class of binary MRF models,” in Proc. *Energy Minim. Methods Comput. Vis. Pattern Recog. (EMMCVPR)*, pp. 136–152. Springer, 2005.
- [36] A. Chambolle and P. L. Lions, “Image recovery via total variation minimization and related problems,” *Numer. Math.*, vol. 76, no. 2, pp. 167–188, Apr. 1997.
- [37] C. L. Chan, P. H. Che, S. Jaggi, and V. Saligrama, “Non-adaptive probabilistic group testing with noisy measurements: Near-optimal bounds with efficient algorithms,” in Proc. *IEEE Allerton Conf.*, pp. 1832–1839, Sep. 2011.
- [38] T. F. Chan and E. Selim, “Aspects of total variation regularized l^1 function approximation,” *SIAM J. Appl. Math.*, vol. 65, no. 5, pp. 1817–1837, Jul. 2005.
- [39] T. F. Chan, E. Selim, and N. Mila, “Algorithms for finding global minimizers of image segmentation and denoising models,” *SIAM J. Appl. Math.*, vol. 66, no. 5, pp. 1632–1648, Jun. 2006.
- [40] T. F. Chan, G. H. Golub, and P. Mulet, “A nonlinear primal-dual method for total variation-based image restoration,” *SIAM J. on Sci. Comput.*, vol. 20, no. 6, pp. 1964–1977, 1999.
- [41] C. Chen, P. Marziliano, and A. C. Kot, “2D finite rate of innovation reconstruction method for step edge and polygon signals in the presence of noise,” *IEEE Trans. Signal Process.*, vol. 60, no. 6, pp. 2851–2859, Jun. 2012.
- [42] D. Cremers, F. Tischhauser, J. Weickert, and C. Schnorr, “Diffusion snakes: introducing statistical shape knowledge into the Mumfords-Shah functional,” *Int. J. Comput. Vis.*, vol. 50, no. 3, pp. 295–313, 2002.

-
- [43] R. Delgado-Gonzalo, V. Uhlmann, D. Schmitter, and M. Unser, "Snakes on a plane: A perfect snap for bioimage analysis," *IEEE Signal Process. Mag.*, vol. 32, no. 1, pp. 41–48, Jan. 2015.
- [44] R. Desai, R. Cheng, and H. D. Cheng, "Pattern recognition by local radial moments," in *Proc. 12th IAPR Int. Conf. Pattern Recog. (ICPR)*, 1994.
- [45] M. N. Do and M. Vetterli, "The contourlet transform: an efficient directional multiresolution image representation," *IEEE Trans. Image Process.*, vol. 14, no. 12, pp. 2091–2106, Dec. 2005.
- [46] M. N. Do and M. Vetterli, "The finite ridgelet transform for image representation," *IEEE Trans. Image Process.*, vol. 12, no. 1, pp. 16–28, Jan. 2003.
- [47] —, "Framing pyramids," *IEEE Trans. Signal Process.*, vol. 51, no. 9, pp. 2329–2342, Sep. 2003.
- [48] D. C. Dobson and F. Santosa, "Recovery of blocky images from noisy and blurred data," *SIAM J. Appl. Math.*, vol. 56, no. 4, pp. 1181–1198, Aug. 1996.
- [49] D. L. Donoho, "Compressed sensing," *IEEE Trans. Inf. Theory*, vol. 52, no. 4, pp. 1289–1306, Apr. 2006.
- [50] R. Dorfman, "The detection of defective members of large populations," *Ann. Math. Stat.*, vol. 14, no. 4, pp. 436–440, Dec. 1943.
- [51] P. L. Dragotti, M. Vetterli, and T. Blu, "Exact sampling results for signals with finite rate of innovation using Strang-Fix conditions and local kernels," in *Proc. IEEE Int. Conf. Acoust. Speech, Signal Process. (ICASSP)*, vol. 4, pp. 233–236, Mar. 2005.
- [52] —, "Sampling moments and reconstructing signals of finite rate of innovation: Shannon meets Strang-Fix," *IEEE Trans. Signal Process.*, vol. 55, no. 5, pp. 1741–1755, May 2007.
- [53] D. Z. Du and F. K. Hwang, *Pooling Designs and Nonadaptive Group Testing: Important Tools for DNA Sequencing*. World Scientific, 2006.
- [54] A. G. Dyachkov and V. V. Rykov, "A survey of superimposed code theory," *Probl. Control Inf. Theory*, vol. 12, no. 4, pp. 1–13, 1983.
- [55] A. G. Dyachkov, V. V. Rykov, and M. Rashad, "Bounds of the length of disjunct codes," *Probl. Control Inf. Theory*, vol. 11, pp. 7–13, 1982.
- [56] Y. C. Eldar, "Sampling with arbitrary sampling and reconstruction spaces and oblique dual frame vectors," *J. Fourier Anal. Appl.*, vol. 9, no. 1, pp. 77–96, Jan. 2003.
- [57] Y. C. Eldar and T. Werther, "General framework for consistent sampling in Hilbert spaces," *Int. J. Wavelets Multiresolut. Inf. Process.*, vol. 3, no. 3, pp. 347–359, 2005.
- [58] P. Erdos, P. Frankl, and Z. Furedi, "Family of finite sets in which no set is covered by the union of n others," *Israel J. Math.*, vol. 51, no. 1-2, pp. 79–89, Dec. 1985.
- [59] M. Fatemi, A. Amini, L. Baboulaz, and M. Vetterli, "Shapes from pixels," *IEEE Trans. Image Process.*, vol. 25, no. 3, pp. 1193–1206, Mar. 2016.

-
- [60] M. Fatemi, A. Amini, and M. Vetterli, "Sampling and reconstruction of shapes with algebraic boundaries," *IEEE Trans. Sig. Process.*, 2015, submitted.
- [61] M. Fatemi, L. Baboulaz, and M. Vetterli, "Optimal sampling rates in infinite-dimensional compressed sensing," in Proc. *10th Int. Conf. Sampling Theory Appl. (SampTA)*, pp. 260–263, Jul. 2013.
- [62] M. Fatemi and M. Vetterli, "Randomized recovery for Boolean compressed sensing," in Proc. *IEEE Int. Symp. Inf. Theory (ISIT)*, pp. 469–473, Jul. 2013.
- [63] M. A. T. Figueiredo, J. M. N. Leitão, and A. K. Jain, "Unsupervised contour representation and estimation using B-splines and a minimum description length criterion," *IEEE Trans. Image Process.*, vol. 9, no. 6, pp. 1075–1087, Jun. 2000.
- [64] W. Fulton, *Algebraic Curves: An Introduction to Algebraic Geometry*. Addison-Wesley, 1989.
- [65] A. C. Gilbert, M. A. Iwen, and M. J. Strauss, "Group testing and sparse signal recovery," in Proc. *Asilomar Conf. Signals Syst. Comp. Conf. Record*, pp. 1059–1063, Oct. 2008.
- [66] B. Gustafsson, "Quadrature identities and the Schottky double," *Acta. Appl. Math.*, vol. 1, no. 209–240, 1983.
- [67] B. Gustafsson, C. He, P. Milanfar, and M. Putinar, "Reconstructing planar domains from their moments," *Inverse Probl.*, vol. 16, no. 4, pp. 1053–1070, 2000.
- [68] I. R. Ionescu and T. Lachand-Robert, "Generalized Cheeger sets related to landslides," *Calc. Var. Partial Differ. Equ.*, vol. 23, no. 2, pp. 227–249, Jun. 2005.
- [69] M. Jacob, T. Blu, and M. Unser, "An exact method for computing the area moments of wavelet and spline curves," *IEEE Trans. Pattern Anal. Mach. Intell.*, vol. 23, no. 6, pp. 633–642, Jun. 2001.
- [70] S. Karlin and W. J. Studden, *Tchebycheff Systems, with Applications in Analysis and Statistics*. New York: Interscience, 1966.
- [71] M. Kass, A. Witkin, and D. Terzopoulos, "Snakes: Active contour models," *Int. J. Comput. Vis.*, vol. 1, no. 4, pp. 321–331, Jan. 1988.
- [72] D. Keren, D. Cooper, and J. Subrahmonia, "Describing complicated objects by implicit polynomials," *IEEE Trans. Pattern Anal. Mach. Intell.*, vol. 16, no. 1, pp. 38–53, Jan. 1994.
- [73] V. V. Kindratenko, "On using functions to describe the shape," *J. Math. Imaging Vis.*, vol. 18, no. 3, pp. 225–245, May 2003.
- [74] J. Kopf and D. Lischinski, "Depixelizing pixel art," *ACM Trans. Graphics*, vol. 30, no. 4, pp. 99:1–99:8, Jul. 2011.
- [75] M. G. Krein, "Über eine neue Klasse von hermiteschen Formen und über eine Verallgemeinerung des trigonometrischen Momentproblems," *Izv. Akad. Nauk.*, vol. 9, pp. 1259–1275, 1993.

-
- [76] J. B. Lasserre and M. Putinar, “Algebraic-exponent data recovery from moments,” *Discrete Comput. Geom.*, vol. 54, no. 4, pp. 993–1012, Dec. 2015.
- [77] J. MacCormick and A. Fitzgibbon, “Curvature regularization for resolution-independent images,” in Proc. *Energy Minimization Methods in Comput. Vis. and Pattern Recog.-EMMCVPR 2013*, pp. 165–179, Jan. 2013.
- [78] D. M. Malioutov and M. B. Malyutov, “Boolean compressed sensing: LP relaxation for group testing,” in Proc. *IEEE Int. Conf. Acoust. Speech, Signal Process. (ICASSP)*, pp. 3305–3308, Mar. 2012.
- [79] D. M. Malioutov and K. R. Varshney, “Exact rule learning via Boolean compressed sensing,” in Proc. *30th Int. Conf. Machine Learning*, pp. 765–773, 2013.
- [80] R. Malladi, J. A. Sethian, and B. C. Vemuri, “Shape modeling with front propagation: A level set approach,” *IEEE Trans. Pattern Anal. and Mach. Intell.*, vol. 17, no. 2, pp. 158–175, Feb. 1995.
- [81] S. Mallat, *A Wavelet Tour of Signal Processing*, 3rd ed. Academic Press, 2009.
- [82] S. Mallat and G. Peyré, “A review of Bandlet methods for geometrical image representation,” *Numer. Algor.*, vol. 44, no. 3, pp. 205–234, Jun. 2007.
- [83] M. B. Malyutov, “Recovery of sparse active inputs in general systems: A review,” in Proc. *IEE Int. Conf. Comput. Tech. Electr. Electron. Eng. (SIBIRCON)*, pp. 15–22, Jul. 2010.
- [84] I. Maravić and M. Vetterli, “Exact sampling results for some classes of parametric non-bandlimited 2-d signals,” *IEEE Trans. Signal Process.*, vol. 52, no. 1, pp. 175–189, Jan. 2004.
- [85] —, “Sampling and reconstruction of signals with finite rate of innovation in the presence of noise,” *IEEE Trans. Signal Process.*, vol. 53, no. 8, pp. 2788–2805, Aug. 2005.
- [86] P. Milanfar, M. Putinar, J. Varah, B. Gustafsson, and G. Golub, “Shape reconstruction from moments: theory, algorithms, and applications,” in Proc. *Int. Symp. Opt. Sci. Tech.*, pp. 406–416. International Society for Optics and Photonics, 2000.
- [87] D. Mumford and J. Shah, “Optimal approximations by piecewise smooth functions and associated variational problems,” *Comm. Pure Appl. Math.*, vol. 42, no. 5, pp. 577–685, 1989.
- [88] H. Pan, T. Blu, and P. L. Dragotti, “Sampling curves with finite rate of innovation,” *IEEE Trans. Signal Process.*, vol. 62, no. 2, pp. 458–471, Jan. 2014.
- [89] J. W. Patterson, C. D. Taylor, and P. J. Willis, “Constructing and rendering vectorised photographic images,” *J. Virtual Reality and Broadcat. (JVRB)*, vol. 9, no. 3, 2012.
- [90] E. L. Pennec and S. Mallat, “Sparse geometric image representation with bandelets,” *IEEE Trans. Image Process.*, vol. 14, no. 4, pp. 423–438, Apr. 2005.
- [91] T. Pock, A. Chambolle, D. Cremers, and H. Bischof, “A convex relaxation approach for computing minimal partitions,” in Proc. *Comput. Vis. Pattern Recog. (CVPR) 2009, IEEE Conf.*, pp. 810–817, Jun. 2009.

-
- [92] T. Pock, D. Cremers, H. Bischof, and A. Chambolle, “An algorithm for minimizing the Mumford-Shah functional,” in Proc. *Computer Vision-ICCV 2009*, pp. 1133–1140, Sep. 2009.
- [93] C. Poon, “A consistent and stable approach to generalized sampling,” *J. Fourier Anal. Appl.*, vol. 20, no. 5, pp. 985–1019, Oct. 2014.
- [94] S. Rad, K. C. Smith, and B. Benhabib, “Application of moments and Fourier descriptors to the accurate estimation of elliptical shape parameters,” in Proc. *IEEE Int. Conf. Acoust. Speech, Signal Process. (ICASSP)*, vol. 4, pp. 2465–2468, 1991.
- [95] R. Raz and S. Safra, “A sub-constant error-probability low-degree test, and a sub-constant error-probability PCP characterization of NP,” in Proc. *ACM Symp. on Theory of Comput. 1997*, pp. 475–484, May 1997.
- [96] L. I. Rudin, S. Osher, and E. Fatemi, “Nonlinear total variation based noise removal algorithms,” *Physica D: Nonlinear Phenomena*, vol. 60, no. 1, pp. 259–268, Nov. 1992.
- [97] D. Sejdinovic and O. Johnson, “Note on the noisy group testing: Asymptotic bounds and belief propagation reconstruction,” in Proc. *IEEE Allerton Conf.*, pp. 998–1003, Sep. 2010.
- [98] P. Selinger, “Potrace: a polygon-based tracing algorithm,” *Potrace (online)*, <http://potrace.sourceforge.net/potrace.pdf> (2009-07-01), 2003.
- [99] C. E. Shannon, “A mathematical theory of communication,” *Bell. Syst. Tech. J.*, vol. 27, pp. 379–423, 1948.
- [100] P. Shukla and P. L. Dragotti, “Sampling schemes for multidimensional signals with finite rate of innovation,” *IEEE Trans. Signal Process.*, vol. 55, no. 7, pp. 3670–3686, Jul. 2007.
- [101] M. Singer, “A general approach to moment calculation for polygons and line segments,” *Pattern Recog.*, vol. 26, no. 7, pp. 1019–1028, Jul. 1993.
- [102] G. Strang, “Maximal flow through a domain,” *Math. Prog.*, vol. 26, no. 2, pp. 123–143, 1983.
- [103] —, “Maximum flows and minimum cuts in the plane,” *J. Global Optim.*, vol. 47, no. 3, pp. 527–535, Jul. 2010.
- [104] E. Strekalovskiy and D. Cremers, “Real-time minimization of the piecewise smooth Mumford-Shah functional,” in Proc. *Comput. Vis.-ECCV 2014*, pp. 127–141, Sep. 2014.
- [105] D. Strong and T. F. Chan, “Edge-preserving and scale-dependent properties of total variation regularization,” *Inverse Probl.*, vol. 19, no. 6, pp. S165–S187, Nov. 2003.
- [106] J. Subrahmonia, D. B. Cooper, and D. Keren, “Practical reliable bayesian recognition of 2D and 3D objects using implicit polynomials and algebraic invariants,” *IEEE Trans. Pattern Anal. Mach. Intell.*, vol. 18, no. 5, pp. 505–519, May 1996.
- [107] V. Y. Tan and V. K. Goyal, “Estimating signals with finite rate of innovation from noisy samples: A stochastic algorithm,” *IEEE Trans. Signal Process.*, vol. 56, no. 10, pp. 5135–5146, Oct. 2008.

-
- [108] G. Taubin, F. Cukierman, S. Sullivan, J. Ponce, and D. J. Krigman, "Parameterized families of polynomials for bounded algebraic curve and surface fitting," *IEEE Trans. Pattern Anal. Mach. Intell.*, vol. 16, no. 3, pp. 287–303, Mar. 1994.
- [109] N. T. Thao and M. Vetterli, "Deterministic analysis of oversampled A/D conversion and decoding improvement based on consistent estimates," *IEEE Trans. Signal Process.*, vol. 42, no. 3, pp. 519–531, Mar. 1994.
- [110] E. Töppe, M. R. Oswald, D. Cremers, and C. Rother, "Image-based 3D modeling via Cheeger sets," in *Proc. Comput. Vis. (ACCV)*, pp. 53–64. Springer, Jan. 2011.
- [111] A. Tsai, A. J. Yezzi, and A. S. Willsky, "Curve evolution implementation of the Mumford-Shah functional for image segmentation, denoising, interpolation, and magnification," *IEEE Trans. Image Process.*, vol. 10, no. 8, pp. 1169–1186, Aug. 2001.
- [112] K. Tsirikolias and B. G. Mertzios, "Statistical pattern recognition using efficient two-dimensional moments with applications to character recognition," *Pattern Recog.*, vol. 26, no. 6, pp. 877–882, Jun. 1993.
- [113] M. Unser, "Splines: A perfect fit for signal and image processing," *IEEE Signal Process. Mag.*, vol. 16, no. 6, pp. 22–38, Nov. 1999.
- [114] —, "Sampling - 50 years after Shannon," *Proc. IEEE*, vol. 88, no. 4, pp. 569–587, Apr. 2000.
- [115] M. Unser and A. Aldroubi, "A general sampling theory for nonideal acquisition devices," *IEEE Trans. Signal Process.*, vol. 42, no. 11, pp. 2915–2925, Nov. 1994.
- [116] M. Unser and J. Zerubia, "A generalized sampling theory without band-limiting constraints," *IEEE Trans. Circuits Syst. II, Analog Digit. Signal Process.*, vol. 45, no. 8, pp. 959–969, Aug. 1998.
- [117] L. Vese and T. Chan, "A multiphase level set framework for image processing using the Mumford-Shah functional," *Int. J. Comput. Vis.*, vol. 50, no. 3, pp. 271–293, 2002.
- [118] M. Vetterli, J. Kovačević, and V. K. Goyal, *Foundations of Signal Processing*. Cambridge University Press, 2014.
- [119] M. Vetterli, P. Marziliano, and T. Blu, "Sampling signals with finite rate of innovation," *IEEE Trans. Signal Process.*, vol. 50, no. 6, pp. 1417–1428, Jun. 2002.
- [120] F. Viola, R. Cipolla, and A. Fitzgibbon, "A unifying resolution-independent formulation for early vision," in *Proc. Comput. Vis. and Pattern Recog. (CVPR), 2012 IEEE Conf.*, pp. 494–501, Jun. 2012.
- [121] R. J. Walker, *Algebraic Curves*. Princeton, New Jersey, 1950.

Curriculum Vitæ

Mitra Fatemi

Audiovisual Communications Laboratory (LCAV)
École Polytechnique Fédérale de Lausanne (EPFL)
CH-1015 Lausanne, Switzerland

Email: mitra.fatemi@epfl.ch

Web-page: <http://lcav.epfl.ch/fatemi>

Personal

Date of birth: January 31, 1985
Nationality: Iranian
Civil status: Married with one child

Education

Sep. 2011–present Ph.D. candidate in School of Electrical Engineering, École Polytechnique Fédérale de Lausanne (EPFL), Lausanne, Switzerland
Sep. 2007–Sep. 2009 M.Sc. in Communication Systems, Cryptography, Sharif University of Technology, Tehran, Iran
Sep. 2003–Sep. 2007 B.Sc. in Electrical Engineering, Communication Systems, Sharif University of Technology, Tehran, Iran

Research Interests

Mathematical Signal and Image Processing, Inverse Problems, Cryptography Protocols

Professional experience

- Sep. 2011–Jul. 2015 **Teaching assistant**, Various bachelor and master level courses, École Polytechnique Fédérale de Lausanne (EPFL), Lausanne, Switzerland
- Nov. 2010–Mar. 2011 **Engineering Intern**, Rezvan. Co., Tehran, Iran
- Sep. 2009–Sep. 2010 **Research Intern**, Advanced Communications Research Institute (ACRI), Sharif University of Technology, Tehran, Iran
- Nov. 2008–Jun. 2009 **Research Intern**, Iran Telecommunication Research Center (ITRC), Tehran, Iran
- 2004–2009 **Instructor**, Teaching different branches of math for high school Olympiad competitors

Publications

Journal papers

1. M. Fatemi, A. Amini and M. Vetterli. Sampling and Reconstruction of Shapes with Algebraic Boundaries, Submitted to *IEEE Transactions on Signal Processing*, Dec. 2015.
2. M. Fatemi, A. Amini, L. Baboulaz and M. Vetterli. Shapes from Pixels, *IEEE Transactions on Image Processing*, Vol. 25, No. 3, pp. 1193-1206, Mar. 2016.
3. M. Fatemi, R. Ghasemi, T. Eghlidos and M. R. Aref. Efficient Multistage Secret Sharing Scheme Using Bilinear Map, *IET Information Security*, Vol. 8, No. 4, pp. 224-229, 2014.
4. M. Fatemi, A. Salahi and S. Salimi. Anonymous Roaming in Universal Mobile Telecommunication System Mobile Networks, *IET Information security*, Vol. 4, No. 2, pp. 93-103, 2010.

Conference papers

1. M. Fatemi, L. Baboulaz and M. Vetterli. Optimal Sampling Rates in Infinite-Dimensional Compressed Sensing. *Sampling Theory and Applications (SampTA)*, Bremen, Germany, Jul. 2013.
2. M. Fatemi and M. Vetterli. Randomized Recovery for Boolean Compressed Sensing. *IEEE International Symposium on Information Theory (ISIT)*, Istanbul, Turkey, Jul. 2013.
3. M. Fatemi, S. Dashmiz, M. H. Shafinia and V. Cevher. Equivalence of Synthesis and Atomic Formulations of Sparse Recovery. *IEEE Statistical Signal Processing Workshop (SSP)*, Ann Arbor, Michigan, USA, 2012.
4. M. Fatemi, S. Salimi and A. Salahi. Improved EndSec: A Practical Protocol for Securing Core Network Signaling in UMTS. *Information Security and Cryptology Conference (ISC)*, Isfahan, Iran, 2009.
5. M. Fatemi, T. Eghlidos and M. Aref. A Multi-stage Secret Sharing Scheme Using All-or-Nothing Transform Approach. *Information and Communications Security*, Beijing, China, Dec. 2009.

Awards and honors

- 2007 Ranked 61st among over 19,000 applicants in Telecommunications major in Iran's Nationwide University Entrance Exam (Konkour) for M.Sc. level.
- 2003 Ranked 51st among over 400, 000 applicants in Iran's Nationwide University Entrance Exam for Engineering and Applied Mathematics, Iran.
- 2003 Ranked 23rd among over 400, 000 applicants in Iran's Azad University Entrance Exam for Engineering and Applied Mathematics, Iran.
- 2002 Recipient of Silver Medal of National Mathematics Olympiad

Computer Skills

C⁺⁺, MATLAB, L^AT_EX, Microsoft Office

Languages

Farsi (Native), English (Advanced), French (Intermediate), Arabic (Basic)

